1. REPORT DATE *(DD-MM-YYYY)*	2. REPORT TYPE	3. DATES COVERED *(From - To)*
01-08-2006	Final Report	04/01/03 – 03/31/06

4. TITLE AND SUBTITLE	5a. CONTRACT NUMBER
Robust Controller For Turbulent And Convective Boundary Layers	
	5b. GRANT NUMBER F49620-03-1-0244
	5c. PROGRAM ELEMENT NUMBER

6. AUTHOR(S)	5d. PROJECT NUMBER
Jason L. Speyer	
	5e. TASK NUMBER
J. John Kim	
	5f. WORK UNIT NUMBER

7. PERFORMING ORGANIZATION NAME(S) AND ADDRESS(ES)	8. PERFORMING ORGANIZATION REPORT NUMBER
Regents of the University of California 10920 Wilshire Boulevard, Suite 1200 Los Angeles, CA 90024-6502	

9. SPONSORING / MONITORING AGENCY NAME(S) AND ADDRESS(ES)	10. SPONSOR/MONITOR'S ACRONYM(S)
OFC of Naval Research San Diego San Diego Regional Office 4520 Executive Dr., Ste 300 San Diego, CA 92121-3019	
	11. SPONSOR/MONITOR'S REPORT NUMBER(S)

12. DISTRIBUTION / AVAILABILITY STATEMENT
Approved for public release; distribution is unlimited.

13. SUPPLEMENTARY NOTES

14. ABSTRACT
Linear feedback controllers and estimators have been designed from the governing equations of a channel flow, linearized about the laminar mean flow, and a layer of heated fluid, linearized about the no-motion state. Spectral decomposition involving a two-dimensional Fourier expansion and a Chebyshev-Galerkin projection cast these linearized equations into state-space form that decoupled to independent Fourier wavenumber sub-systems. The control law are designed by applying Linear Quadratic Gaussian (LQG) synthesis to these sub-systems. The size of the controller is reduced by both limiting the number of sub-systems, on which LQG synthesis is applied, as well as applying system theoretic model reduction techniques to each sub-system. This methodology has produced highly effective controllers to suppress convection in a heated fluid layer, but has found only moderate success with the channel flow. While the Oberbeck-Boussinesq equations (heated fluid layer) provide a direct measure of Rayleigh-Bénard convection, the Poiseuille flow equations do not. The feedback control laws for channel flow could only indirectly affect viscous drag. An open-loop optimization has been applied to the channel flow control problem in an effort to capture more of the nonlinear dynamics and, thereby, affect the viscous drag directly. During these experiments, it has been discovered that upstream traveling waves of blowing and suction not only reduces the skin-friction drag in a channel but also sustains it below laminar levels.

15. SUBJECT TERMS
drag reduction, convection suppression, LQR, LQG, model reduction, channel flow, turbulence

16. SECURITY CLASSIFICATION OF:			17. LIMITATION OF ABSTRACT	18. NUMBER OF PAGES	19a. NAME OF RESPONSIBLE PERSON
a. REPORT	**b. ABSTRACT**	**c. THIS PAGE**			
				68	**19b. TELEPHONE NUMBER** *(include area code)* 310-206-4451

ROBUST CONTROLLER FOR TURBULENT AND CONVECTIVE BOUNDARY LAYERS

Jason L. Speyer and John Kim

Mechanical and Aerospace Engineering Department

University of California, Los Angeles

Los Angeles, CA 90095-1597

Final Report

August 1, 2006

Linear feedback controllers and estimators have been designed from the governing equations of a channel flow, linearized about the laminar mean flow, and a layer of heated fluid, linearized about the no-motion state. Spectral decomposition involving a two-dimensional Fourier expansion and a Chebyshev-Galerkin projection cast these linearized equations into state-space form that decoupled to independent Fourier wavenumber sub-systems. The control law are designed by applying Linear Quadratic Gaussian (LQG) synthesis to these sub-systems. The size of the controller is reduced by both limiting the number of sub-systems, on which LQG synthesis is applied, as well as applying system theoretic model reduction techniques to each sub-system. This methodology has produced highly effective controllers to suppress convection in a heated fluid layer, but has found only moderate success with the channel flow. While the Oberbeck-Boussinesq equations (heated fluid layer) provides a direct measure of Rayleigh-Bénard convection, the Poiseuille flow equations do not. The feedback control laws for channel flow could only indirectly affect viscous drag. An open-loop optimization has been applied to the channel flow control problem in an effort to capture more of the nonlinear dynamics and, thereby, affect the viscous drag directly. During these experiments, it has been discovered that upstream traveling waves of blowing and suction not only reduces the skin-friction drag in a channel but also sustains it below laminar levels.

Table of Contents

1   Introduction

The potential benefits of controlling flows to reduce drag are significant. Commercial airlines consume about 1.5 billion barrels a year. A flow control scheme that reduces drag by 20% could save $15 billion per year (at $50 per barrel). Reduced drag can also provide faster speed instead of savings in fuel consumption. In the past decade, flow control has shifted from depending on the investigator's intuition built on empirical observations to more systematic approaches focusing on the dynamics of the flow field [1, 2]. In our studies, we have applied modern control theories to linearized Navier-Stokes equations with suction/blowing actuation along the channel walls with no net mass transfer. The resulting controllers were implemented and evaluated in a direct numerical simulation (DNS) of a turbulent channel flow.

Spectrally decomposing the Navier-Stokes equations linearized around the laminar profile in a channel results in a dynamical model in state-space form that decouples to independent sub-systems by wavenumber. A parallel architecture of compensators in wave space is thus possible [3]. Control laws are synthesized for only certain wavenumbers, reducing the size of the overall controller. Furthermore, the individual sub-systems can be reduced using modern control theories (based on observability and controllability). Although the linearized equations are missing the nonlinear terms in the Navier-Stokes equations, Linear Quadratic Gaussian (LQG) controllers of just a few wavenumbers have been moderately successful in reducing the viscous drag. We have reported approximately 15%-18% reductions in previous reports [4]. However, further reductions have been difficult to achieve.

The primary obstacle to improved performance appeared to be the lack of a cost function in the linearized equations that directly relates to mean skin-friction drag. The same control methodology applied to the suppression of Rayleigh-Bénard convection in a heated layer of fluid produced remarkable results [5, 6, 7, 8] (Appendix A, B, and C). The Oberbeck-Boussinesq equations provided a direct quadratic cost of convection; however, the flow control problem only had indirect cost functions. This motivated an investigation into periodic optimization algorithms. By inducing small perturbations of the open-loop controls and periodic flow field conditions in the nonlinear DNS, direct numerical gradients associated with the drag were computed. These gradients were used to make improvements to the control history and initial flow conditions to directly improve drag reduction.

In the process of simplifying this procedure, we discovered that wall-normal blowing and suction on the upper and lower walls in the form of two-dimensional waves traveling *upstream* could reduce the skin-friction drag to *below* laminar levels. Defined as simple streamwise sine waves, these control waves do not change the net mass flux of the channel. Even more remarkably, this behavior appeared to be a *sustainable*, *steady-state* solution. Although the properties of the nonlinear dynamics that results in the sub-laminar drag are not completely understood, we show that the Orr-Sommerfeld equation is a good predictor of the nonlinear channel flow's response to traveling waves.

2   Achievements

The linearized three-dimensional Navier-Stokes equations as the basis for designing fully three-dimensional reduced-order controllers. Improvements to the estimation in the LQG synthesis recovered the Linear Quadratic Regulator (LQR) performance; however, both seemed to have a performance limit. During the effort to find a more direct measure of drag reduction with periodic optimization, we found that upstream traveling waves could drive skin-friction drag below laminar. LQG controllers for Rayleigh-Bénard convection suppression were more successful; reduced-order controllers successfully stabilized convection in linear and non-linear simulations of a heated layer of fluid.

2.1   LQG/Loop Transfer Recovery Matches LQR in Flow Control
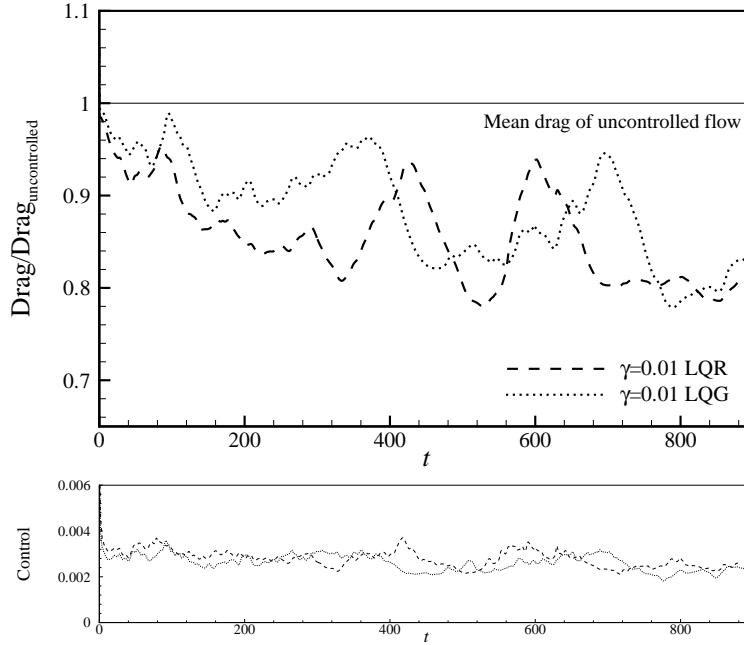
Figure 1: Drag evolution of LQG and LQR controlled turbulent flow. γ is the regulator cost function tuning parameter, which weights the control input against the cost function of the perturbed streamwise wall-shear stress.

The Navier-Stokes equations, linearized about a laminar Poiseuille flow profile, are used as a basis for the design of reduced-order controllers. The decomposition, a two-dimensional Fourier expansion in the streamwise and spanwise directions and a Galerkin projection in the wall-normal direction, decoupled the dynamical equations by each Fourier wavenumber. LQG synthesis is applied to a few of these independent sub-systems, in effect applying control to suppress perturbations only at certain Fourier wavenumbers. Furthermore, each sub-system is further reduced

by selecting only the most controllable and observable modes. Thus, the controller equations are reduced 98% in size. Application on fully nonlinear turbulent DNS of a channel flow have been moderately successful with approximately 15%-18% reduction in drag [4]. Linear mechanisms are demonstrated to be an important part of sustaining turbulence [9].

Comparison of the un-rotated, full-state linearized equations evolution and nonlinear DNS with sufficiently small amplitudes revealed slight differences in the truncation errors present in both simulations. The differences were significant enough to prevent the estimation filter from accurately reconstructing the plant state. The estimation was significantly improved by accounting for the differences in truncation errors, and the LQG controllers were able to perform about as well as the full state feedback, LQR controllers (see Figure 1). However, in experiments with different cost functions, such as minimal perturbation energy and reducing the coupling term to the Squire equations, the resulting controllers were unable to gain any further reductions in drag.

2.2 Upstream Travelling Wave: sub-laminar drag

Our linear control design was based on the notion that if the perturbations can be removed at all significant wavenumbers, the the indirect effect would be a reduction in mean viscous drag. Since it became clear that this indirect approach to drag reduction would be of limited effectiveness, a more direct approach that links perturbations in each wavenumber pair to drag through the nonlinearities in the the governing equations was investigated. Noting that our LQR controllers transiently induced below laminar drag [10] with certain initial flow fields, we attempted to determine if there were a periodic process in which average drag could be sustained below that of laminar flow. Initial attempts using a sequence of two controllers, one that induced below laminar drag and the other to recover the initial flow conditions, did not result in reduced averaged sustained drag below laminar flow. Therefore, we took a direct approach by developing a numerical code to determine the optimal periodic open-loop control. Using our DNS code as the plant, perturbations were made in the parameterized controls as well as the initial flow conditions for a small set of wave number pairs. Numerical gradients were constructed and became inputs to an accelerated gradient optimization technique.

It might appear that this effort would not produce sustained drag below laminar flow based on a conjecture proposed by Bewley and Aamo [11]:

> Conjecture: *The lowest sustainable drag of an incompressible constant mass-flux channel flow, when controlled via a distribution of zero-net mass-flux blowing/suction over the no-slip channel walls, is exactly that of the laminar flow.*

However, in the process of simplifying this complex numerical scheme, we discovered that two-dimensional waves of wall-bounded, wall-normal blowing and suction made to travel *upstream* can reduce skin-friction drag on a sustained basis. This traveling wave control is defined in physical

space as

$$v_{\mathrm{w}}(x,t) = a \, \cos\big(k_x(x - c\,t)\big) \quad ,$$

where a is a scalar, c is the convective speed normalized to the mean centerline velocity, k_x is the streamwise wavenumber, v_w denotes the wall-normal velocity at the wall, i.e. wall-normal suction or blowing, and is applied to both the upper and lower walls of the channel in varicose mode, where suction (and blowing) occurs at the same streamwise location at both walls. By convention, the control on the upper wall will have a minus sign to denote blowing (positive sign for suction) and the opposite for the lower wall.
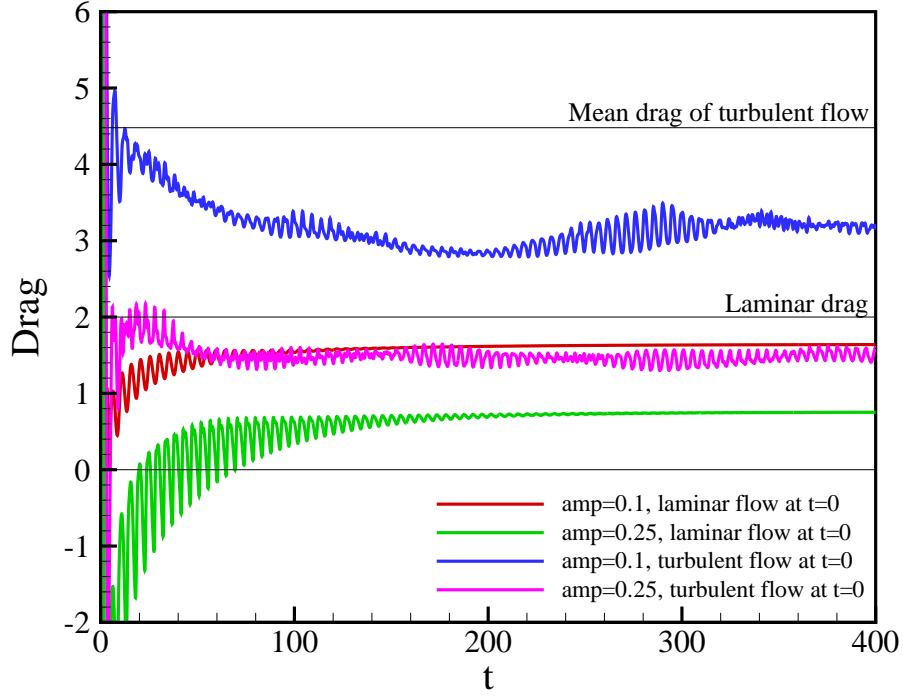
Figure 2: Time history of drag in DNS at Re=2000. Upstream traveling wave control applied at $k_x = 0.5$, speed -2 (upstream). Initially turbulent simulations are full three-dimensional, while initially laminar simulations are two-dimensional to reduce compuational requirements.

Although the exact mechanism is not fully understood, upstream traveling waves have been found to be able to force sustained *below* laminar drag in simulations initialized by both laminar and turbulent flows (Figure 2). The efficiency of these controllers as the ratio of the power saved minus the input power to input power, η, is

$$\eta = \frac{\mathrm{Power_{saved}} - \mathrm{Power_{input}}}{\mathrm{Power_{input}}} \quad , \tag{1}$$

Here $\mathrm{Power_{saved}}$ is the drag reduction from the laminar solution, and $\mathrm{Power_{input}}$ is calculated from an energy balance on the channel volume and represents the amount of power needed to push or draw fluid out of the channel.

Preliminarily calculations of efficiency for below laminar drag initialized from laminar flow is $\eta = -0.50$ for the 0.1 amplitude case in Figure 2 and $\eta = -0.54$ for the other. Initialized from the turbulent channel flow, the efficiencies improves to more favorable values, $\eta = 4.67$ (amplitude = 0.1) and $\eta = 7.46$ (amplitude = 0.25). Further research is required to improve the efficiency.

The recent derivation by Fukagata *et al.* [12, 13] provides some explanation about the mechanism which sustains drag reduction to below laminar levels. For a channel flow, they derived an explicit relationship between skin-friction drag value and the Reynolds shear stress. The following form follows from their derivation:

$$\langle D \rangle_\infty = \langle D \rangle_l + \frac{3\mathrm{Re}}{2} \int_{-1}^{1} \overline{u\,v}\, y\, dy \;, \tag{2}$$

where $\langle D \rangle_\infty$ represents the total skin-friction drag, $\langle D \rangle_l$ denotes the laminar drag value, and Re is the Reynolds number of flow centerline velocity, u is the streamwise perturbation velocity, v is the wall-normal perturbation velocity, $\overline{u\,v}$ denotes the Reynolds shear stress, and y denotes the wall-normal direction. While Fukagata *et al.* have reported a conceptual feedback controller using Lorentz body forces to achieve sub-laminar skin-friction drag [13], our open-loop control drives the integral of the Reynolds shear stress to become negative with more realizable control inputs, i.e. surface blowing and suction.

In order to understand how the control is able to drive the Reynolds shear stress negative, the linear mechanism associated with this phenomena is exploited. Solutions to the Orr-Sommerfeld equation of the channel flow reveal negative distributions of the Reynolds shear stress when subjected to upstream traveling waves. Using the linearized equations, we can easily find the expected drag reductions, i.e. $\int_{-1}^{1} \overline{u\,v}\, y\, dy$, for any wave speed (Figure 3) at steady-state. We can see that while the channel responds very adversely to downstream traveling waves, at certain upstream speeds, i.e. $c < 0$, the drag will be reduced. Furthermore, it suggests that there is some optimal speed at which the most amount of drag reduction can be achieved. The peak that appears at downstream wave speeds (approximately $c = 0.515$ for wave at $k_x = 0.5$) corresponds to the most observable and controllable mode. While adverse for drag, the downstream traveling waves are also worth studying for desirable effects in certain applications. For example, it appears that an optimized downstream traveling wave can be used to prevent or delay separation in turbulent boundary layers subject to a strong adverse pressure gradient (e.g. diffusers or flow over airfoil).

As shown in Figure 4, for small amplitudes the linear equations predict very well the amount of drag reduction that will be achieved in the nonlinear DNS. Thus we believe that the linearized equations provide a good approximation in which to analyze the channel flow response to traveling waves. This provides a computationally inexpensive avenue for further analysis and control development for improved drag reduction. Details of our preliminary analysis are given in [14]

5
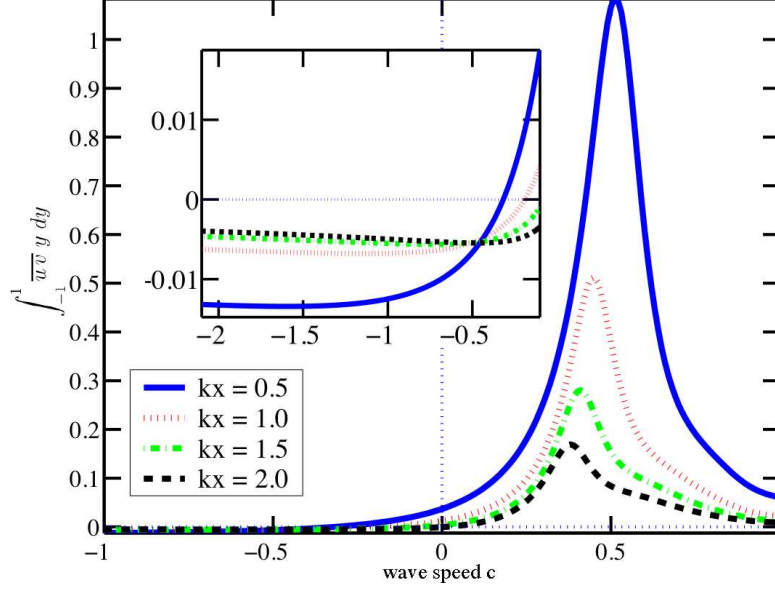
Figure 3: The weighted Reynolds shear stress integral as a function of the control wave speed (normalized by the centerline velocity) for a Poiseuille channel flow at Re = 1500.
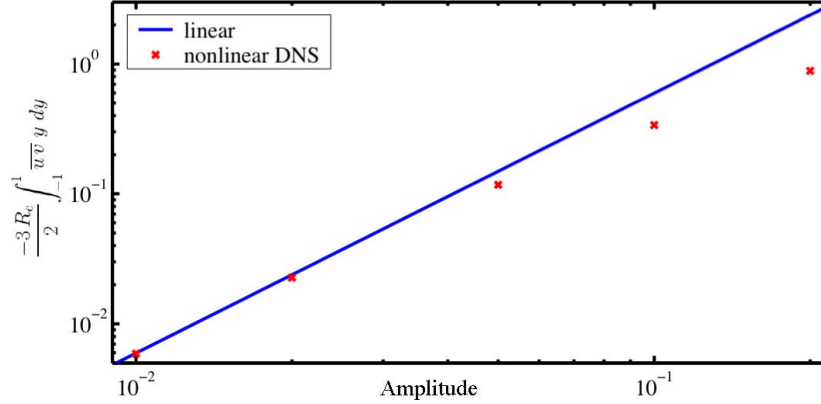
Figure 4: Comparison of drag reduction predicted by linearized equations and found in nonlinear DNS.

(Appendix D).

2.3 Robust Feedback Control of Rayleigh-Bénard Convection

Over the last three years we have developed feedback control methods for the suppression of thermal convection, that have potential applications to material processing, molding and crystal growth. These controllers have been shown to be quite robust within very realistic simulations. These controllers have matured sufficiently to warrant experimental verification.

6

Although a proportional feedback controller has shown certain effectiveness in increasing the Rayleigh number at which convection starts, much better performance is obtainable by using a LQG controller. The LQG provides a systematic and optimal way to synthesize a high-order compensator, that guarantees a high stability margin. Comparable performance by a PID method will require strategic placements of compensator poles and zeroes for a multiple-input and multiple-output system, which is a difficult task if the system has large order.

A closed-loop linear stability analysis was published in [5]. Detailed stability boundary curves are computed. Since the study was to show the controller performance, only the Prandtl number, $Pr = 7.0$, was considered. This value corresponds to water at room temperature as the working fluid. The sensor-actuator model consists of three embedded sensor planes and one actuator plane coincided with the lower wall. Both sensing and actuating are assumed to be spatially and temporally continuous. In this configuration the closed-loop stability curves indicate that convection suppression up to Rayleigh number (Ra) equal to 14.5 times the critical value ($Ra_{c0} = 1707.76$) is achievable. However, these are linear stability results and require infinitesimally small amplitudes of convection in the fluid layer. In applications, this requirement is probably not achievable.

To relax the restriction, we replace the linear plant model with a three-dimensional nonlinear model [6] (Appendix A). Developed using the pseudo-spectral method, this model provides a realistic simulation of a heated fluid layer. The nonlinear time-domain simulations show that a finite-amplitude, steady-state convection in a layer of fluid at $Ra = 10^4$ can be removed by applying the same linear optimal controller designed in the previous study [5].

In [7] (Appendix B), two important advances are made: (i) a reduced-order compensator is developed and (ii) a gain-schedule approach is proven in concept by simulation. For order reduction, results show that at least 8 Chebyshev modes are required in the compensator for effective performance. By using the gain scheduling approach which involves a two-step Ra profile, we are able to raise the suppressed no-motion state to about 12 times Ra_{c0}. The closed-loop linear stability limit occurs at about 14.5 times Ra_{c0}, which puts an upper bound to the nonlinear simulation. In [8] (Appendix C), the models have been improved by eliminating the idealized thermal boundary conditions and replacing them by walls of finite thickness. As for deviational errors, the compensator model is run at the nominal values, while the corresponding parameters in the plant model are allowed to change from their nominal values from which stability margins are computed. Stability margins are also determined for the Rayleigh number, the wavenumber, the actuator delay, and the sensor-plane depth uncertainty. The conservatism of these robust stability margins are investigated via a fully nonlinear, 3D simulation. As the conclusion of the study, we believe the concept can now be implemented as laboratory experiments.

3   Conclusions and Future Work

It is clear from the results of this study that Linear Quadratic control laws can be effective in controling nonlinear phenomenon. However, there is a limit to its performanace. While the control can be highly effective if a direct measure of the desired quantities is available such as with the Rayleigh-Bénard convection suppression problem, the linear controllers are severely limited when the desired objective is only available indirectly, such as drag reduction in channel flows.

The effect of traveling waves of wall-bounded, wall-normal suction and blowing definitely warrants further study. While using the same actuation that appeared limited with the LQR/LQG controllers, a simple open-loop scheme is able to demonstrate dramatic drag reduction, even driving the drag below sub-laminar levels. The results found in this study are very preliminary. A better understanding of the phenomonen as well as the flow field induced by these traveling waves will be required before improvements can be made to the control schemes, both in terms of further reduction, flow stability, and efficiency of control.

4 References

References

[1] J. Kim, "Control of turbulent boundary layers," *Physics of Fluids*, vol. 15, pp. 1093–1105, May 2003.

[2] T. R. Bewley, "Flow control: New challenges for a new renaissance," *Progress in Aerospace Sciences*, vol. 37, pp. 21–58, 2001.

[3] L. Cortelezzi and J. L. Speyer, "Robust reduced-order controller of laminar boundary layer transitions," *Physical Review E*, vol. 58, pp. 1906–1910, August 1998.

[4] K. H. Lee, L. Cortelezzi, J. Kim, and J. L. Speyer, "Application of robust reduced-order controller to turbulent flows for drag reduction," *Physics of Fluids*, vol. 13, no. 5, pp. 1321–1330, 2001.

[5] A. C. Or, L. Cortelezzi, and J. L. Speyer, "Robust feedback control of Rayleigh-Bénard convection," *Journal of Fluid Mechanics*, vol. 437, pp. 175–202, 2001.

[6] A. C. Or and J. L. Speyer, "Active suppression of finite amplitude Rayleigh-Bénard convection," *Journal of Fluid Mechanics*, vol. 483, pp. 111–128, 2003.

[7] A. C. Or and J. L. Speyer, "Gain-scheduled controller for the suppression of convection at high Rayleigh number," *Physical Review E*, vol. 71, no. 4, 2005.

[8] A. C. Or and J. L. Speyer, "Robust control for convection suppression in a fluid layer: The effects of boundary properties, actuator delay and major parameter uncertainties," *Physical Review E*, vol. 73, April 2006.

[9] J. Kim and J. Lim, "A linear process in wall-bounded turbulent shear flows," *Physics of Fluids A*, vol. 12, no. 8, pp. 1885–1888, 2000.

[10] L. Cortelezzi, K. H. Lee, J. Kim, and J. L. Speyer, "Skin-friction drag reduction via robust reduced-order linear feedback control," *International Journal of Computational Fluid Dynamics*, vol. 11, no. 1-2, pp. 79–92, 1998.

[11] T. R. Bewley and O. M. Aamo, "A 'win-win' mechanism for low-drag transients in controlled two-dimensional channel flow and its implications for sustained drag reduction," *Journal of Fluid Mechanics*, vol. 449, pp. 183–196, 2004.

[12] K. Fukagata, K. Iwamoto, and N. Kasagi, "Contribution of Reynolds stress distribution to the skin friction in wall-bounded flows," *Physics of Fluids*, vol. 14, no. 11, pp. L73–L76, 2002.

[13] K. Fukagata, N. Kasagi, and K. Sugiyama, "Feedback control achieving sublaminar friction drag," in *Proceedings of the 6th Symposium on Smart Control of Turbulence*, (Tokyo, Japan), pp. 143–148, March 6-9 2005.

[14] T. Min, S. M. Kang, J. L. Speyer, and J. Kim, "Sustained sub-laminar drag in a fully developed channel flow," *Journal of Fluid Mechanics*, vol. 558, pp. 309–318, 2006.

APPENDIX A:

Active Suppression of Finite Amplitude Rayleigh-Bénard Convection

Active suppression of finite-amplitude Rayleigh–Bénard convection

By A. C. OR AND J. L. SPEYER

Department of Mechanical and Aerospace Engineering, University of California, Los Angeles,
CA 90095-1597, USA

We study by a fully nonlinear three-dimensional pseudospectral time-splitting simulation, the feedback control of a layer of fluid heated from below. The initial condition corresponds to a steady large-amplitude preferred convection state obtained at Prandtl number of 7.0 and Rayleigh number of 10^4, which is about six times the Rayleigh critical value. A robust controller based on the LQG (linear–quadratic–Gaussian) synthesis method is used. Both sensors and actuator are thermal-based, planar, and assumed to be continuously distributed. The simulated results show that large-amplitude steady-state convection rolls can be suppressed by the linear LQG controller action. The Green's function of the controller gives the shape of the control action corresponding to a point measurement. In addition, for Rayleigh numbers below the proportional feedback control stability limit, this controller appeared to be effective in damping out steady-state convection rolls as well. However, in a region very near the proportional control stability limit, proportional control action induces subcritical g-type hexagonal convection, which is obtained here through direct simulations. Note that well above this proportional control limit, the LQG still damps out all convection. The nonlinear plant model is validated by comparing check cases with published results.

1. Introduction

Active suppression of onset of convection in a layer of fluid has potentially important applications in improving the material that goes through solidification in a mould. For instance, during the growth phase of large silicon wafers or composite materials, a large thermal gradient typically causes undesirable convective motions in the melt. To understand the active control of the realistic manufacturing process, an idealized system is an important starting point. To this end Rayleigh–Bénard convection (RBC) is ideal for vigorous theoretical analysis.

Many theoretical studies have employed the linear feedback control to increase the stability threshold of the purely heat conductive state so that no convection occurs despite the presence of a large thermal gradient (Tang & Bau 1993, 1994, 1998*a*, *b*; Howle 1997*a*, *b*, *c*, 2000; Or, Cortelezzi & Speyer 2001). These studies used the linear plant model and employed a simple controller using the proportional feedback. The implantable sensor and actuator are assumed to be of the thermal type and continuously distributed spatially on the horizontal plane. Analysis as well as experimental results in general indicate that the proportional controller will stabilize the basic state up to Rayleigh number (Ra) of 3 to 4 times its critical value of the basic state (see Tang & Bau 1994; Howle 1997*a*). Furthermore, as shown in

Tang & Bau (1994), a controller-induced oscillatory instability occurs at a large gain. A linear–quadratic–Gaussian (LQG) controller has also been studied (Or *et al.* 2001) to increase the region of stabilization and with a higher margin of robustness. First, the stability limit can be raised to about 14 times the critical value of Ra. Secondly, the gain and phase margins about the design point of the controller appear adequate for practical implementation.

To develop a control design to be implementable for applicational processes (such as for crystal growth or a melt), it is crucial to understand the control process for simpler geometry and material properties. We have been focused on an Oberbeck–Boussinesq model for a horizontal layer of fluid. The plant dynamics is known as Rayleigh–Bénard convection (RBC) (Cross & Hohenberg 1993). As a first step, the performance of the linear controller design for the linear plant dynamics is reported in Or *et al.* (2001). In this paper, as a step further, the focus is turned to the performance of the linear controller design for the fully nonlinear plant dynamics.

It is well known that in a large layer of heated fluid, convection occurs as a steady pattern of two-dimensional rolls. The two-dimensional convection rolls and the stability properties were investigated in detail by Clever & Busse (1974) and Busse & Clever (1979). For the heated layer corresponding to $Ra > Ra_{c0}$ (Ra_{c0} is computed theoretically to have the value of 1707.762 up to 3 decimal places), the stable roll pattern occurs only within a band of wavenumber centred approximately about the critical wavenumber $\alpha_c = 3.117$. Within the stable band the rolls realized do not necessarily have a preferred length scale. Indeed, their wavelength appears to be dictated by the initial conditions used to select the rolls and by the manner that the basic state temperature is prescribed spatially and temporally. The band is bounded on both sides by instabilities that pertain to changing the wavelength of the rolls but not changing the planform. As the induced rolls acquire a wavelength too large or too small, an instability will occur to shift their length scale back to a value close to the critical value. As the value of Ra increases, the rolls will at some point becomes unstable and the convection structure will converge to a pattern with more complex spatial or temporal structure. The exact value of Ra at which the transition occurs is wavenumber dependent. For a Prandtl number (Pr) of 7.0, for instance, the two-dimensional rolls become unstable to a three-dimensional bimodal convection at roughly $Ra \approx 25Ra_{c0}$ at the wavenumber of about 2.0 (see the experimental observations presented in figure 11, Busse & Clever 1979). The transition highlights a sufficiently strong thermal boundary-layer effect, made possible at Ra values. The transition to three-dimensional convection occurs at a significantly higher Ra threshold than the closed-loop stability limit of $14.5Ra_{c0}$ based on the linear LQG controller (Or *et al.* 2001). For our control analysis here, therefore, we need only to consider the two-dimensional rolls as the initial state of convection to be controlled.

Our present control problem can be investigated most effectively by the use of time-domain analysis. A three-dimensional fully nonlinear pseudospectral model using a time-splitting integration method is developed, based on the Oberbeck–Boussinesq equations. The proportional feedback controller is easily implementable. This case provides the check cases for code validation purposes. Certain flow patterns that are known to be induced by the controller effects, such as the oscillation mode (Tang & Bau 1994) and the g-type hexagons (Or & Kelly 2001), can be obtained here from the direct numerical simulations and compared with those reported from previous analyses. In §2, the nonlinear plant model and the LQG controller will be briefly described. The results will be presented in §3, followed by the conclusion in §4.

2. Mathematical formulation

2.1. *Nonlinear plant model and numerical solution*

The nonlinear plant model is governed by the Oberbeck–Boussinesq equations for a horizontal layer of fluid. In the non-dimensional form d, d^2/κ, κ/d, κ/d^2, $\rho(\kappa/d)^2$ and ΔT are used as the scales of length, time, velocity, vorticity, pressure and temperature, where d is the layer thickness, κ and ρ are the mean thermal diffusivity and density of the fluid, and ΔT is the temperature difference between the upper and lower wall in the purely conductive basic state. The governing non-dimensional equations are,

$$Pr^{-1}\partial_t \boldsymbol{v} = Pr^{-1}\boldsymbol{v} \times \boldsymbol{\omega} + \boldsymbol{k}Ra\theta - \nabla\pi + \nabla^2\boldsymbol{v}, \tag{2.1}$$

$$\partial_t\theta = -\boldsymbol{v}\cdot\nabla\theta + w + \nabla^2\theta, \tag{2.2}$$

$$\nabla\cdot\boldsymbol{v} = 0, \tag{2.3}$$

where $\boldsymbol{v} = (u, v, w)$ is the velocity vector field, $\boldsymbol{\omega} = \nabla\times\boldsymbol{v}$ is the vorticity, $\pi = p+\boldsymbol{v}\cdot\boldsymbol{v}/2$ is the pressure head, θ is the perturbation temperature and $\boldsymbol{k}$ is the unit vector in the z-direction. The two external parameters are Rayleigh and Prandtl numbers, given by $Ra = g\Delta T d^3/\nu\kappa$ and $Pr = \nu/\kappa$ where ν is the mean kinematic viscosity. The continuity equation (2.3) applies only when the flow is incompressible.

The velocity field is assumed to be non-permeable and non-slip at the upper and lower walls, thus subject to

$$\boldsymbol{v}(x, y, 0, t) = \boldsymbol{0}, \quad \boldsymbol{v}(x, y, 1, t) = \boldsymbol{0}. \tag{2.4}$$

The temperature field, on the other hand, is assumed to satisfy the isothermal condition at the upper wall. The lower wall is non-isothermal owing to the action of the thermal actuation. It is assumed that a control temperature $\theta_c(x, y, t)$ can be imposed. The upper and lower thermal boundary conditions for the perturbation field are therefore

$$\theta(x, y, 1, t) = 0, \quad \theta(x, y, 0, t) = \theta_c(x, y, t). \tag{2.5}$$

In order to perform the feedback control, the perturbation temperature field has to be measured in the fluid. In our model, three sensor planes are embedded in the layer at carefully chosen levels at $z = z_s$ (with $s = 1, 2$ and 3). For analysis purposes, these sensor planes are assumed to exert no blockage effects on the flow field. They measure the planar temperature distribution in the layer,

$$\theta(x, y, z_s, t) = \theta_s(x, y, t), \quad s = 1, 2, 3. \tag{2.6}$$

Assuming a continuous-distributed sensor, $\theta_s(x, y, t)$ are known at sampled points and time.

In the numerical scheme, the dependent variables u, v, w, p and θ are expressed by the following truncated, triple sums,

$$\begin{bmatrix} u \\ v \\ w \\ p \\ \theta \end{bmatrix}(x, y, z, t) = \mathrm{Re}\left\{ \sum_{n=0}^{N}\sum_{k=0}^{K}\sum_{m=-M+1}^{M} \begin{bmatrix} u_{kmn} \\ v_{kmn} \\ w_{kmn} \\ p_{kmn} \\ \theta_{kmn} \end{bmatrix}(t)T_n(z)\ \exp(\mathrm{i}(k\alpha_x x + m\alpha_y y)) \right\} \tag{2.7}$$

where Re denotes the real part of the sum, α_x and α_y are the fundamental wavenumbers in the x- and y-directions, respectively. The asymmetric treatment of the indices k and m reduces the number of coefficients by half because the velocity, pressure and temperature are real dependent variables (see Marcus 1984). These two parameters are prescribed in the model. The functions $T_n(z)$ ($n = 0, 1, \ldots$) denote the

Chebyshev polynomials. Note that a linear coordinate transformation is implicitly assumed to convert the Chebyshev function domain between $+1$ and -1 to our physical range $0 \leqslant z < 1$. The actuator and sensor temperatures, θ_c and θ_s ($s = 1, 2$ and 3), are planar (two-dimensional). They are expanded in double series in a similar fashion,

$$\begin{bmatrix} \theta_s(z_1, t) \\ \theta_s(z_2, t) \\ \theta_s(z_3, t) \\ \theta_c(0, t) \end{bmatrix} (x, y, t) = \mathrm{Re} \left\{ \sum_{k=0}^{K} \sum_{m=-M+1}^{M} \begin{bmatrix} \theta_{km,s}(z_1, t) \\ \theta_{km,s}(z_2, t) \\ \theta_{km,s}(z_3, t) \\ \theta_{km,c}(0, t) \end{bmatrix} \exp(\mathrm{i}(k\alpha_x x + m\alpha_y y)) \right\}. \quad (2.8)$$

In our terminology, the lower thermal boundary condition (2.5) and the sensor equations (2.6) are, respectively, the input to and output from the nonlinear plant model.

The nonlinear equations, together with the boundary and the continuity equations are then solved numerically by using the pseudospectral, time-splitting integration technique (Gottlieb & Orszag 1977; Canuto *et al.* 1986; Bodenschatz, Pesch & Ahlers 2000). Marcus (1984) provided a detailed description of the implementation of the method for the Taylor-vortex flow simulations. Using the time-splitting method, an integration time step is split into three fractional steps. The first is a nonlinear fractional step, typically done using an explicit, second-order Adams–Bashforth scheme,

$$\boldsymbol{v}^{N+1/3} = \boldsymbol{v}^N + \Delta t \tfrac{3}{2} [\boldsymbol{v}^N \times \boldsymbol{\omega}^N + Pr Ra\theta^N \boldsymbol{k}] - \Delta t \tfrac{1}{2} [\boldsymbol{v}^{N-1} \times \boldsymbol{\omega}^{N-1} + Pr Ra\theta^{N-1} \boldsymbol{k}], \quad (2.9)$$

$$\theta^{N+1/3} = \theta^N - \Delta t \tfrac{3}{2} [\boldsymbol{v}^N \cdot \nabla\theta^N - w^N] + \Delta t \tfrac{1}{2} [\boldsymbol{v}^{N-1} \cdot \nabla\theta^{N-1} - w^{N-1}]. \quad (2.10)$$

The superscript N here denotes the time step and is not to be confused with the truncation number for the vertical dependence. A significant fraction of the total computation load occurs in computing the nonlinear terms. In the collocation space, the nonlinear terms are computed spatially by point-by-point multiplications. However, fast Fourier transforms (FFT) and inverse fast Fourier transforms (IFFT) have to be used to convert the field back and forth between the collocation and the Chebyshev–Fourier spaces. The fast Fourier transform (FFT) and inverse fast Fourier transform (IFFT) routines are obtained from the library of the *Numerical Recipes* (Press *et al.* 1992), with some minor modifications. For validation, these routines have been checked against the standard *Matlab* FFT and IFFT functions and match up to 15 decimal places. For typical flow fields, the truncation errors from FFT and IFFT due to aliasing are mainly small (Marcus 1984; Press *et al.* 1992). We note that, however, that the FFT method can still be computationally demanding for high-resolution solutions. The pseudospectral method is generally known to be efficient. There also exist other efficient methods not using the transforms, for instance, the reduced-order Galerkin method (Howle 1996).

After obtaining the $(N + 1/3)$th fractional step with the Adams–Basforth scheme, we compute the $(N + 1)$th step from the following equation,

$$(1 - Pr\Delta t \nabla^2)\boldsymbol{v}^{N+1} = \boldsymbol{v}^{N+1/3} - Pr\Delta t \nabla\pi, \quad (2.11)$$

subject to $\nabla \cdot \boldsymbol{v}^{N+1} = 0$. It is noted that, in general, $\nabla \cdot \boldsymbol{v}^{N+1/3} \neq 0$. The most straightforward procedure for solving (2.11) appears to be splitting the equation into a pressure step and a viscous step (we refer to it as the direct approach). In the pressure step, the flow field subject to a no normal-flow boundary condition at the walls can be solved from a Poisson equation, based on the property that the

pressure field is irrotational and the flow field satisfies the continuity constraint (2.3). Next, a diffusive fractional step completes the solution of the fractional velocity and temperature fields by prescribing the no-slip and thermal boundary conditions at the walls. As simple as it appeared, the scheme had problems computing the correct flow field. In his numerical simulation of Taylor vortex flow, Marcus (1984) reported large boundary errors using this direct approach. In his discussions it was argued that the shear may play a role and it is not clear whether a similar problem will occur for RBC. In our study we have applied the direct scheme in our preliminary simulations and observed large errors even for the open-loop simulations. Thus, it appears that the problem is common to both Taylor vortex flows and RBC. For more detail about the cause of the large boundary errors in the direct approach, we refer to Marcus (1984). Marcus identified the source of errors and developed a procedure to correct it. His remedy is to further split the fractional solution into a complementary and a particular solution so that the boundary conditions and the continuity equations are satisfied numerically. The procedure, however, involves the additional computation of several Green's functions and seems elaborate. Since the boundary-value problem corresponding to (2.11) is linear, we anticipate there are simpler alternative approaches to resolve the numerical difficulty. Here, we solve the problem involving the pressure and viscous forces as a single step, without splitting the pressure and viscous terms. First, we use the continuity equation as the constraint and eliminate the two horizontal velocity components in favour of the vertical component. Secondly, we obtain the solution of the boundary-value problem for w and θ. Finally, we recover u and v from w, Fourier mode by Fourier mode, again using the continuity equation. This scheme seems significantly simpler and has been tested here to be effective. Because of the simplicity, it is worth the description as an alternative approach to the time-splitting procedure.

By eliminating pressure from (2.11), we obtain a single scalar equation governing w,

$$(1 - Pr\Delta t\nabla^2)\nabla^2\partial_z w^{N+1} = \nabla_\perp^2 \partial_z w^{N+1/3} - \partial_{zz}^2\left(\partial_x u^{N+1/3} + \partial_y v^{N+1/3}\right). \tag{2.12}$$

The equation above is integrated in z, this gives

$$(1 - Pr\Delta t\nabla^2)\nabla^2 w^{N+1} = \nabla_\perp^2 w^{N+1/3} - \left(\partial_{xz}^2 u^{N+1/3} + \partial_{yz}^2 v^{N+1/3}\right). \tag{2.13}$$

The integration constant is zero because of the non-slip boundary condition. (This constant will depend on the initial conditions when the case of free-slip boundary conditions is considered). Equation (2.13) is of fourth-order spatially. It has to satisfy four boundary conditions, as follows,

$$w^{N+1} = 0, \quad \partial_z w^{N+1} = 0 \quad \text{at } z = 0, 1. \tag{2.14}$$

The fourth-order boundary-value problem, (2.12), determines w^{N+1}. After we have obtained w^{N+1}, the horizontal velocity components corresponding to w^{N+1} can be obtained by inverting the continuity and Helmholtz equations, Fourier mode by Fourier mode. In the expansion, w^{N+1} is given by

$$w^{N+1}(x, y, z, t) = \text{Re}\left\{\sum_{k=0}^{K} \sum_{m=-M+1}^{M} w_{km}^{N+1}(z, t)\exp(i(k\alpha_x x + m\alpha_y y))\right\}. \tag{2.15}$$

Similarly, the horizontal velocity components are

$$\begin{bmatrix} u^{N+1}(x, y, z, t) \\ v^{N+1}(x, y, z, t) \end{bmatrix} = \text{Re}\left\{\sum_{k=0}^{K} \sum_{m=-M+1}^{M} \begin{bmatrix} u_{km}^{N+1}(z, t) \\ v_{km}^{N+1}(z, t) \end{bmatrix} \exp(i(k\alpha_x x + m\alpha_y y))\right\}. \tag{2.16}$$

Each pair of coefficients $(u_{km}^{N+1}, u_{km}^{N+1})$ now satisfies a Helmholtz equation

$$\nabla_\perp^2 \begin{bmatrix} u_{km}^{N+1} \\ v_{km}^{N+1} \end{bmatrix} = \alpha_{km}^2 \begin{bmatrix} u_{km}^{N+1} \\ v_{km}^{N+1} \end{bmatrix}, \tag{2.17}$$

where $\alpha_{km} = \{(k\alpha_x)^2 + (m\alpha_y)^2\}^{1/2}$. The Helmholtz equation together with the continuity equation allows us to solve for $\boldsymbol{v}_{km}^{N+1}$ in terms of w_{km}^{N+1}, provided that $\alpha_{km} \neq 0$. The condition $\alpha_{km} \neq 0$ can occur in the case of a free-slip wall, but not in the case of a no-slip wall. We refer to the discussion of Cross & Hohenberg (1993, p. 970). The perturbation temperature field, on the other hand, is not constrained to have zero mean field. Using the continuity equation, we obtain the horizontal velocity components,

$$u_{km}^{N+1} = \frac{1}{\alpha_{km}^2} \partial_{xz}^2 w_{km}^{N+1}, \quad v_{km}^{N+1} = \frac{1}{\alpha_{km}^2} \partial_{yz}^2 w_{km}^{N+1}. \tag{2.18}$$

2.2. *The proportional feedback controller*

In the proportional feedback control, a proportional relationship is constructed between the input and output of the plant. As in the cases studied by Tang & Bau (1994) and Or *et al.* (2001), only one sensor plane is used and the control law in this case is

$$\theta_c(0, t) = -K_p \theta_s(z_s, t), \tag{2.19}$$

where K_p is a constant gain and z_s is the vertical height of the sensor plane. The controller is very simple for this case.

2.3. *The LQG controller*

The theory and design of the LQG controller was described in Or *et al.* (2001). In brief, the linear stability equations of the Fourier-decomposed system of convection and the measurement equation are given in matrix form, respectively, by

$$\dot{x} = \boldsymbol{A}x + \boldsymbol{B}u, \quad z = \boldsymbol{C}x, \tag{2.20}$$

where the entries of the state vector x are the Chebyshev coefficients of velocity and temperature perturbations; u (measured at plane $z = 0$) and z (measured at planes z_1, z_2 and z_3) are, respectively, the Fourier coefficients of the planar control and measured temperatures. Note that the Fourier-decomposed equations correspond to wavenumber α_{km} and Rayleigh number Ra. The following modifications to the original formulation of the controller model (Or *et al.* 2001) have been made here: (i) the vertical dependence is expanded in terms of the Chebyshev polynomials instead of the beam functions as the basis functions. The expansion procedure, originally based on the Galerkin method, has been converted to the tau method. In the improved numerical procedure, we obtain the exact condition $\boldsymbol{D} \equiv \boldsymbol{0}$, in contrast to the previous condition that $\boldsymbol{D} \to \boldsymbol{0}$ only as $N \to \infty$. (ii) We no longer consider the wavenumber as a prescribed parameter here. Instead, an individual modal controller is developed for each set of wavenumbers $(k\alpha_x, m\alpha_y)$. There is a set of state-space equations for each wave vector. In total, there are $2(K + 1)M$ sets of $\boldsymbol{A}$, $\boldsymbol{B}$ and $\boldsymbol{C}$ matrices to be processed.

The LQG controller is comprised of a Kalman filter and an optimal regulator. The Kalman filter equation and the optimal regulator equation corresponding to the state-space equations, (2.20), are, respectively,

$$\dot{\hat{x}} = \boldsymbol{A}^*\hat{x} + \boldsymbol{B}^*u + \boldsymbol{K}_f(z - \hat{z}), \quad \hat{z} = \boldsymbol{C}^*\hat{x}, \quad u = -\boldsymbol{K}_c\hat{x}, \tag{2.21}$$

$\theta_{km,c}(0,t)$
Control action

$\theta_{km,s}(z_s,t)$
Measurements

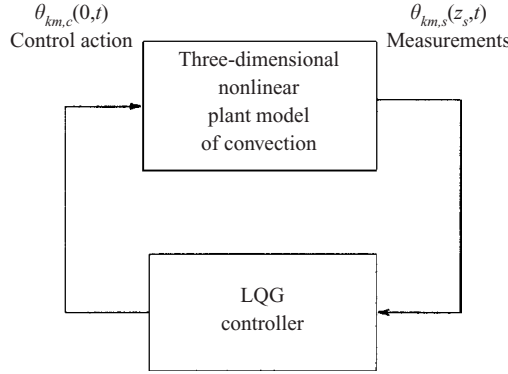Three-dimensional nonlinear plant model of convection

LQG controller

FIGURE 1. The LQG control loop diagram.

where x is the estimate state vector. We distinguish the matrices with asterisk superscripts to highlight that the system is computed at a nominal (designed) wavenumber and Rayleigh number, (α_{km}^*, Ra^*). The Kalman gain vector K_f and the optimal gain vector K_c are determined from separate steady-state algebraic Riccati equations. The Kalman filter is used here as a state observer rather than as an estimator since no noises are injected into the system simulation. The cost functional, weighting and filter parameters chosen for controller design are described in detail in Or *et al.* (2001) which will not be repeated here. For robustness, in the design, the Kalman filter input matrix G has been set equal to the control input matrix B, a step known as the loop transfer recovery to recover the full-state feedback performance of the optimal regulator. The weights for the objective functions, as well as the filter parameters and the loop transfer recovery are described in Or *et al.* (2001).

It is worth noting that the LQG controller is a variant of the H_∞ controller when the disturbance attenuation bound is infinite (see Rhee & Speyer 1991). In Or *et al.* (2001), robustness is demonstrated classically by having large gain and phase margins in the closed-loop response. Furthermore, if a full loop transfer recovery is achieved, the full-state feedback LQ regulator performance will have a robustness of $\pm 60°$ phase margin and 6 db to infinite gain margin. Since our system is non-minimal phased, only partial recovery is expected. Since large gain and phase margins were obtained for the linear system, the performance of the LQG controller in terms of robustness should not be expected to be significantly different from that of the H_∞ controller.

In figure 1, we show the three-dimensional nonlinear plant model. The control input and measurement output of the model are Fourier–Chebyshev coefficients rather than their collocation point values. On the other hand, in the physical plant (such as in laboratory experiments) the input and output are physical temperature distributions. Since the LQG controller is formulated in the modal space, when the upper block represents the plant instead of the model, an FFT and an IFFT have to be performed, respectively, at the input and output of the controller. In our case, the LQG controller takes the measurements from the three-dimensional nonlinear plant model (Fourier coefficients at sensor planes) as input and determines a control action (Fourier coefficients at actuator plane) as output. The estimate state vector represents the vertical structure and the state matrices A^*, B^*, C^* and D^* are computed in terms of the designed values of wavenumber and Rayleigh number, α_{km}^* and Ra^* (see equation (3.7) of Or *et al.* 2001).

The truncation numbers $(K = 32, M = 32, N = 32 + 1)$ considered here are of moderate size. It is still convenient to compute and pre-store the steady-state Kalman gain $\boldsymbol{K}_f$ and regulator gain, $\boldsymbol{K}_c$. However, it is not feasible to pre-store the state matrices $\boldsymbol{A}^*$ for all the wavenumbers. Instead, we compute $\boldsymbol{A}^*$ for each set of wavenumbers at each time step in the time loop. At each time step, the three sensor plane temperatures, in modal coefficients, $\theta_{km,s}(z_i, t)$ $(i = 1, 2$ and $3)$ (see (2.8)), are exported from the nonlinear plant model. There are $6(K + 1)M$ of such coefficients, corresponding to wavenumbers 0 to $K\alpha_x$ in the x dependence and $(-M + 1)\alpha_y$ to $M\alpha_y$ in the y dependence. These values are then fed into the controller which consists of the Kalman filter and the regulator. The controller processes the information based on the measured data and determines the control output in terms of a set of $2(K + 1)M$ modal coefficients for $\theta_{km,c}(0, t)$. These values are then input into the nonlinear model through the lower-wall boundary condition.

2.4. *Green's function for point sensors and actuators*

In some experimental implementations (Tang & Bau 1998a), the sensors and actuators are discrete rather than continuous. For the low-resolution point sensors and actuators (typically with spacing between array points of $O(d)$), it is desirable to stack the arrays of sensor and actuator points vertically on top of each other. Indeed, our result will show that the maximal effect of actuation caused by an impulse on the sensor plane occurs as a point collocated horizontally with the impulse. For a linear system, the controller input-to-output relationship can be expressed in the following integral form,

$$\theta_c(x, y, t) = \int \int \int G(x, y, t | x', y', t') \theta_s(x', y', t') \, \mathrm{d}x' \, \mathrm{d}y' \, \mathrm{d}t', \qquad (2.22)$$

where $\theta_c(x, y, t)$ and $\theta_s(x', y', t')$ are, respectively, the planar actuator and sensor temperature fields. Here, (x, y) and (x', y') denote coordinates for the actuator and sensor planes, respectively. The kernel $G(x, y, t, | x', y', t')$ is a Green's function (or an influence function). The first three arguments in G represent the effect and the last three represent the cause.

In principle, the input and output of the LQG controller can be represented by a linear differential operator L. The precise form of L need not be specified here, since for our purpose the Green's function will be computed spectrally. In terms of L, we can describe some general properties of Green's function. The input and output temperatures to the controller are governed by $L\theta_c = \theta_s$, subject to appropriate lateral boundary conditions in x, y. The Green's formula for any two arbitrary functions $u(x, y, t)$ and $v(x, y, t)$ can be written as the sum of an integral $\int \int \int (uLv - vL^+u) \, \mathrm{d}x' \, \mathrm{d}y' \, \mathrm{d}t'$ and a number of terms evaluated at the lateral boundaries $x = 0, 2\pi/\alpha_x$ and $y = 0, 2\pi/\alpha_y$. In the formula, L^+ is the adjoint operator of L. Now if further restrictions are imposed on u and v, the Green's formula produces some important property about the Green's function. Let $u = G(x, y, t | x_1, y_1, t')$ and $v = G^+(x, y, t | x_2, y_2, t')$ where G and G^+ satisfy, respectively,

$$\left. \begin{aligned} LG(x, y, t | x_1, y_1, t') &= \delta(x - x_1)\delta(y - y_1)\delta(t - t'), \\ L^+G^+(x, y, t | x_2, y_2, t') &= \delta(x - x_2)\delta(y - y_2)\delta(t - t'). \end{aligned} \right\} \qquad (2.23)$$

In addition, G and G^+ satisfy the appropriate lateral boundary conditions and adjoint boundary conditions so that the boundary terms in the Green's formula vanish. The

Green's formula becomes

$$\int\int\int (G^+ LG - GL^+ G^+)\,dx'\,dy'\,dt' \equiv 0. \tag{2.24}$$

Substituting (2.23) into (2.24), we obtain Maxwell's reciprocity relationship $G(x_2, y_2, t|x_1, y_1, t') = G^+(x_1, y_1, t|x_2, y_2, t')$. In our problem, the lateral boundary conditions are periodic. The differential operators in x and y are even in ∂_x and ∂_y. The linear operator L is self-adjoint, i.e. $L \equiv L^+$ and the symmetric relationship holds,

$$G(x_2, y_2, t|x_1, y_1, t') = G(x_1, y_1, t|x_2, y_2, t'). \tag{2.25}$$

The symmetry relationship above can be interpreted as follows: at a given time $t > t'$, an actuator output of the controller at (x_2, y_2) due to a unit impulsive sensor input of the controller at (x_1, y_1) and time t' is equal to the actuator output at (x_1, y_1) due to a unit impulse sensor input at (x_2, y_2) and time t'.

Of particular interest here is the shape of the actuator temperature $\theta_c(x, y, t)$ generated by a unit impulse temperature at a sensor point (x_p, y_p), say, at $t = t_p$. The spatial roll-off of the actuator temperature affects the spatial resolution of the spacing between sensor points. Let the impulsive measurement be

$$\theta_s(x', y', t') = \delta(x' - x_p)\delta(y' - y_p)\delta(t' - t_p), \tag{2.26}$$

from (2.22) we obtain the Green's function

$$\theta_c(x, y, t) = G(x, y, t|x_p, y_p, t_p). \tag{2.27}$$

For each Fourier mode that corresponds to the wave vector $(k\alpha_x, m\alpha_y)$ (where $-K/2 \leqslant k \leqslant K/2$ and $-M/2 \leqslant m \leqslant M/2$), the coefficient represents an entry of measurement vector z in the filter equation, (2.21). We then have

$$u(z, k\alpha_x, m\alpha_y, t) = \int_0^t \exp(\boldsymbol{A}^* - \boldsymbol{K}_f \boldsymbol{C}^*)(t - \tau)z(\tau)\,d\tau. \tag{2.28}$$

Note that the homogeneous solution due to the initial condition decays rapidly and does not contribute for sufficiently large t. After the z and u of all the Fourier modes are computed, a FFT will transform the two sets of coefficients to $\theta_s(x, y, z_s, t)$ and $\theta_c(x, y, 0, t)$, respectively. When $\theta_s(x, y, z_s, t)$ is impulsive according to (2.26), then (2.28) gives the Green's function.

3. Numerical results

3.1. *Nonlinear convection*

Above the value $Ra = Ra_{c0} \approx 1707.76$, the no-motion state gives rise to steady two-dimensional convection rolls. Depending on the value of Pr, these rolls in turn will become unstable at still higher values of Ra, making transitions to two-dimensional oscillatory convection or steady three-dimensional convection depending on the value of the Prandtl number. Cross & Hohenberg (1993) give considerable detail about the bifurcation diagram.

Before engaging in the closed-loop numerical simulations, it is worth performing some comparisons to known results, as check cases for validating the nonlinear plant model. In Clever & Busse (1974), selective Nusselt number values for the two-dimensional convection solution were published. Table 1 shows the values of the Nusselt number, Nu, for several different values of Ra at $Pr = 0.71$ and 7.0 for

Ra	$Pr = 0.71$	$Pr = 7.0$
2000	1.210 (1.212)	1.214 (1.214)
2500	1.472 (1.475)	1.475 (1.475)
10 000	2.653 (2.661)	2.608 (2.618)

TABLE 1. Nusselt number values for two-dimensional rolls.

two-dimensional rolls at $\alpha_x = 3.117$ ($\alpha_y = 0$). The Nusselt number is a measure of the convective heat transfer, defined as the value of temperature gradient at either upper or lower wall,

$$Nu = 1 + \sum_{n=0}^{N} \theta_{00n} \frac{\mathrm{d}T_n(z)}{\mathrm{d}z}\bigg|_{z=0,1}, \tag{3.1}$$

where the first two zero indices of θ_{00n} correspond to $k = m = 0$ so that the sum represents the temperature gradient averaged over the horizontal plane. In the absence of an internal heat source, the values of Nu evaluated at $z = 0$ and $z = 1$ should be equal. Our open-loop, steady-state solutions are obtained at truncation numbers $K = 16$, $M = 8$ and $N = 16$, for $\alpha_x = 3.117$ and $\alpha_y = 0$ (transverse rolls). In table 1, the values published in Clever & Busse (1974) are shown in parentheses. In all cases, the difference between our value and theirs is less than 0.4%. For values of wavenumber $\alpha_x = 2.2$ and 2.6, respectively, where $Pr = 7$ and $Ra = 10\,000$, we obtain $Nu = 2.465$ and 2.548 versus their values 2.473 and 2.557. We further note that Nu should not depend on the orientation of rolls. As a consistency check, we compare the Nu of our solutions between the longitudinal ($\alpha_x = 0$, $\alpha_y \neq 0$) and transverse rolls ($\alpha_x \neq 0$, $\alpha_y = 0$). The difference of the Nu values is found to be less than 0.02%.

3.2. *Proportional feedback control*

We now turn to the proportional feedback control problem. From the results of Tang & Bau (1994) and Or *et al.* (2001), oscillatory convection occurs when the proportional gain K_p becomes sufficiently large. At $K_p = 6$, for instance, the linear theory at $Pr = 7$ predicts that an oscillatory instability is preferred over the steady-state rolls. The closed-loop threshold of stability is $\alpha_c = 3.73$ and $Ra = 3.63Ra_{c0}$, with the frequency of oscillation equal to 20.4. For the same values of Ra and wavenumber we use the steady state two-dimensional rolls as the initial conditions for our time-domain simulation. Our results appear to be consistent with the prediction of linear theory. Figure 2 shows the behaviour of Nu of the closed-loop solutions at $K_p = 6$ for two values of Ra/Ra_{c0}: at 3.55 (solid) and 3.65 (dashed). In both curves, the open-loop steady two-dimensional rolls are used as the initial condition. These rolls are obtained at $Ra/Ra_{c0} = 3.65$ and $\alpha_x = 3.73$ which yield $Nu = 2.273$. In figure 2 the solid curve shows stable behaviour whereas the dashed curve is unstable. The neutral curve has Ra/Ra_{c0} approximately equal to 3.60. This value is in close agreement with the result of linear theory. Furthermore, the oscillatory behaviour in the curves indicate a frequency of about 40.3, again consistent with eigenvalue prediction of 2×20.4 of the linear theory. It is noted that Nu has a harmonic frequency equal to twice the fundamental frequency.

The oscillatory convection appears to have a two-dimensional roll planform. The more interesting finding according to the numerical simulations is that this oscillatory solution is not unique for the given set of external parameters. It turns out when we prescribe an additional small perturbation field in the y-dependence, for the same
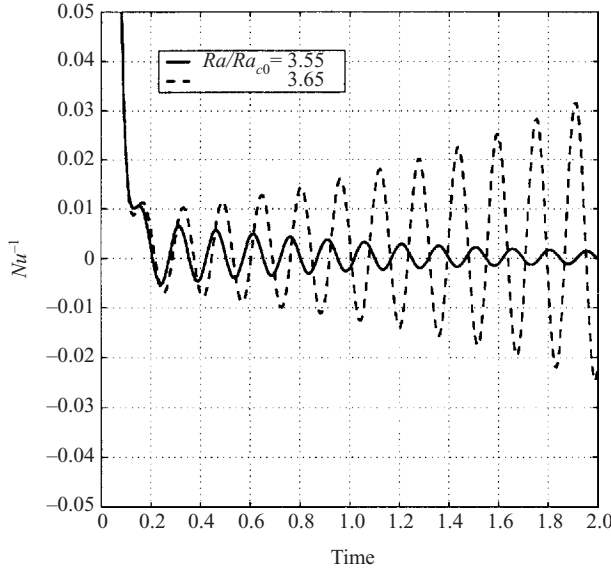
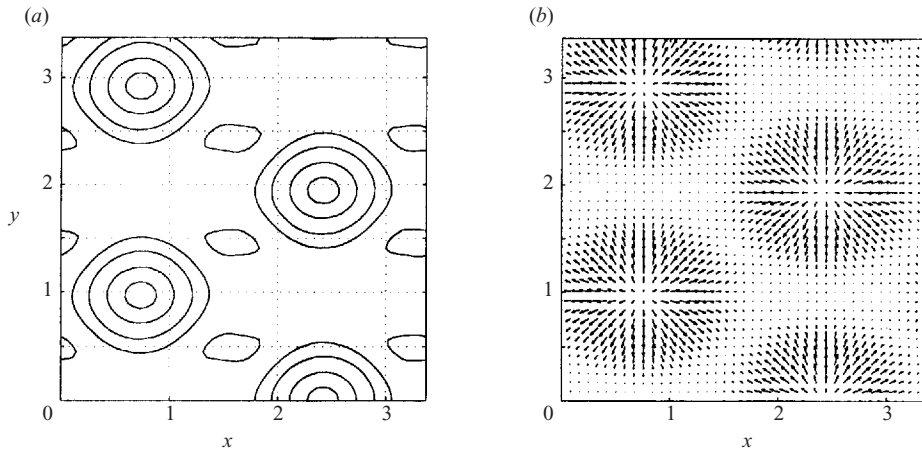FIGURE 2. Nusselt number of oscillatory convection.

FIGURE 3. Closed-loop solution: g-type hexagon pattern.

values of K_p, Ra and α_x, the closed-form solution will not settle at the two-dimensional oscillatory branch if the cross-roll perturbation is not small. For sufficiently large cross-roll perturbations, the solution will settle down at a subcritical branch. In this case, the horizontal planform solution is three-dimensional, which resembles the g-type hexagons (Or & Kelly 2001). Depending on the asymmetry in the perturbation temperature, hexagon cells with sinking motion near the centre of the cell and rising motion near the cell wall is referred to as the g-type. For the ℓ-type hexagons the opposite is true. In figure 3, we show (*a*) the planform corresponding to temperature at the lower wall ($z = 0$) and (*b*) the planform corresponding to horizontal velocity components at horizontal plane $z = 0.1$ (the velocity components vanish at the lower wall owing to a non-slip boundary condition). The three-dimensional hexagonal convection is a steady-state pattern and corresponds to $Nu = 1.4352$. The hexagonal
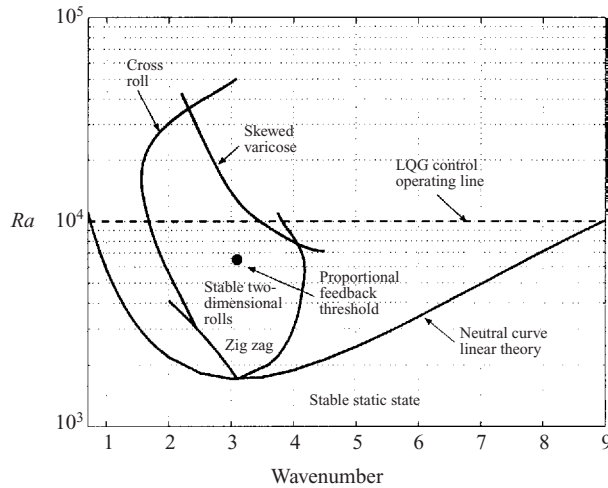
FIGURE 4. A sketch of the stability boundaries for the uncontrolled layer at $Pr = 7.0$.

solution induced by the controller action has been studied in considerable detail (see Shortis & Hall 1996; Or & Kelly 2001) based on weakly nonlinear analysis. Here, we actually obtain the solution from a direct numerical simulation. We summarize several important conclusions based on the results presented. (i) The solutions obtained from our fully nonlinear three-dimensional pseudospectral plant model have been checked and agree reasonably well against known published results from other independent methods. (ii) The proportional feedback controller induces a subcritical range of g-type hexagonal convection, which appears to be captured in the nonlinear simulations. Near the stability threshold of the closed-loop system with sufficiently large gain, both two-dimensional oscillatory convection and three-dimensional steady-state hexagonal convection can co-exist in the same parameter region. Next, we consider the closed-loop simulation using the LQG controller.

3.3. *Closed-loop simulations using the LQG controller*

We investigate the closed-loop system with an operating condition of the plant model at $Pr = 7.0$ and $Ra = 10^4$. In the set-up, the controller gains K_f and K_c are steady states, precomputed and stored. The actual controller and the nonlinear plant models are implemented in *FORTRAN* and *MATLAB*. This controller is implemented according to the description in §2.3.

In figure 4, we provide a sketch of the stability diagram of the uncontrolled dynamics at $Pr = 7$ (see Busse & Clever 1979, figure 1 for the original plot). The stability boundary of the purely conduction (static) state is the lowest parabolic-shaped curve. At each Ra above the minimum of this neutral curve (supercritical), the linear theory predicts an outer band of wavenumbers in which the basic state is unstable. However, at each supercritical Ra, the stable finite-amplitude convection occurs in a narrower band of wavenumbers. At $Pr = 7$, the stable finite-amplitude convection in the inner band corresponds to steady two-dimensional convection rolls. For $Ra = 10^4$ (the dashed line in figure 4), the inner band of wavenumbers is bounded on the lower side by the cross-roll instability at $\alpha \approx 1.75$ and on the higher side by the skew-varicose instability at $\alpha \approx 3.5$. At this Ra, the inner band of wavenumbers is significantly smaller than the outer band obtained from the linear theory, which

gives approximately 0.74 and 9.0, respectively. The stability boundaries are in general *Pr* dependent.

The stable two-dimensional convection rolls are characterized by a single wavenumber, but it can be any value within the inner band. Laboratory experiments (see Cross & Hohenberg 1993) using different initial conditions had demonstrated that the stable pattern can have a non-unique wavenumber. On the other hand, certain experiments performed by letting *Ra* vary either as a slow function of time or by inducing a spatial ramp in the layer thickness indicate that the rolls are realized with a unique wavenumber. Since our goal here is to eliminate the convection pattern, the detailed properties of the nonlinear solution do not concern us other than as the initial condition for our closed-loop solutions.

The closed-loop simulation is demanding computationally in the sense that the entire outer band of wavenumbers should be covered in the stabilization of the basic state. In our simulation, the fundamental wavenumbers α_x and α_y are selected so that the expansion covers the entire inner band, but falls short of the outer band. We argue that this arrangement is reasonable and we use the truncation numbers $K = M = N = 32$. The nonlinearity has the role of limiting the wavenumber of the convection pattern to the inner band. As the initial condition for the closed-loop simulation, we let $\alpha_x = 1.0$ in the open-loop run with appropriate initial condition. We obtain a steady, two-dimensional roll pattern with a wavenumber of 3.0. In the closed-loop simulation, we add in a small perturbation of cross-rolls superimposed on the steady finite-amplitude rolls. The added perturbation assures that the initial condition used is three-dimensional.

The closed-loop simulation results are shown in figures 5(*a*)–5(*g*). Since the transition is two-dimensional, it suffices to reveal the flow fields by showing the cross-sectional view in the (z, x)-plane. In figures 5(*a*)–5(*c*), we show the transient pattern of the perturbation isotherms in the (x, z)-plane (with basic temperature subtracted). The three isotherm patterns (figures 5*a*–5*c*) of the disturbance field are snapshots obtained at $t = 0$, 0.05 and 0.2 diffusive time units, respectively. Note that the upper and lower wall are both the perturbation isotherm of zero temperature. The solid (dashed) lines indicate positive (negative) increments of temperature. The same increment of temperature applies to all three panels. Figure 5(*a*) shows the cross-section of the steady-state convection rolls used as the initial condition at $t = 0$. Shortly after the controller is turned on at $t = 0$, figure 5(*b*) shows that a steep thermal boundary-layer pattern develops near the lower wall at $t = 0.05$. This boundary temperature perturbation possesses an opposite sign to the perturbation in the bulk of the layer of fluid, and therefore exerts a cancellation effect, which tends to drive the fluid towards an isothermal state. Figure 5(*c*) shows at a later instant ($t = 0.2$) that the isotherm pattern indeed settles towards a static state. Here, the isotherms correspond to a residual temperature distribution of about 1.5% of the temperature shown in figure 5(*a*). The residual temperature continues to approach zero asymptotically in time.

In figures 5(*d*)–5(*f*) we show the quiver plots of the velocity field corresponding to isotherms in figures 5(*a*)–5(*c*). The arrow sizes in figures 5(*e*)–5(*f*) are according to the true relative scale. For illustration of the flow field we deliberately magnify the arrows in figure 5(*f*). Note that the velocity rolls are shifted by a phase of $\pi/2$ relative to the isotherm rolls. The upward (downward) motion of fluid is associated with the positive (negative) isotherms, as indicated in the figures. From figure 5(*e*), we observe that the upwelling and downwelling regions are significantly perturbed by the control action. As a result, a secondary row of vortices near the lower wall
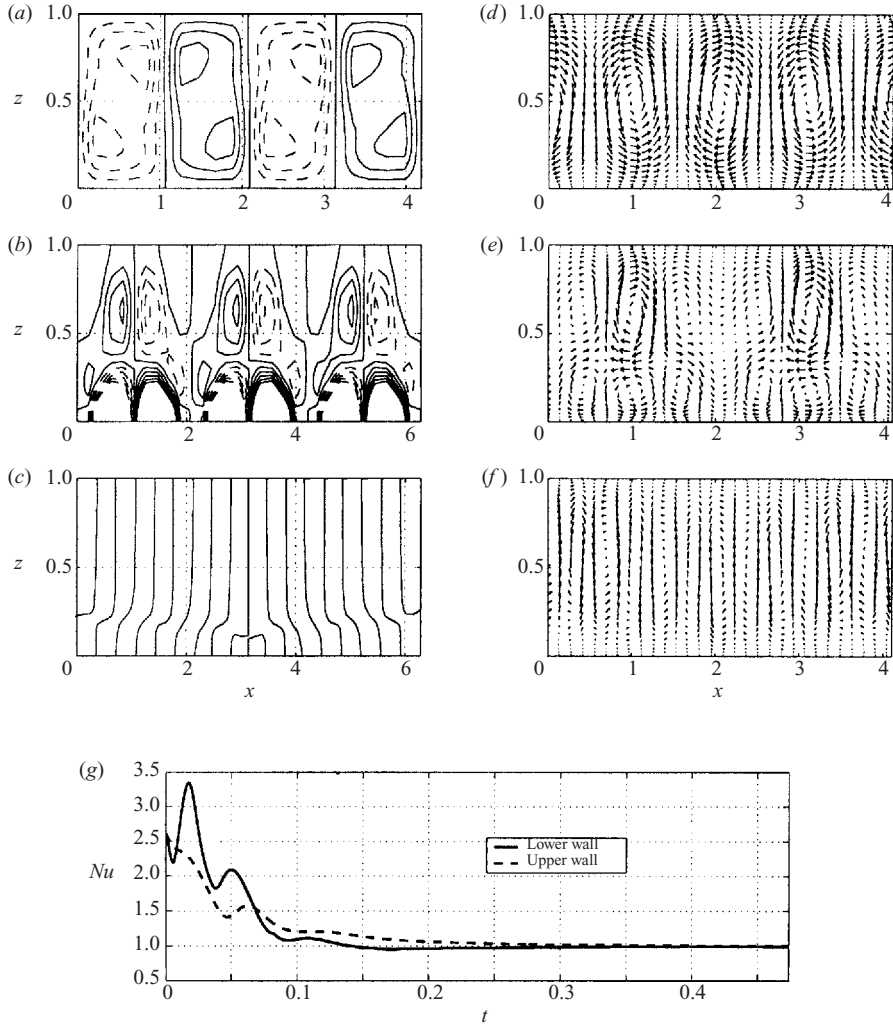
FIGURE 5. (*a*)–(*c*) Transient patterns of isotherm under controller action; (*d*)–(*f*) correspond-
ing velocity quivers of the flow patterns; (*g*) Time response of Nusselt numbers at the lower
and upper wall ($Ra = 10^4$ and $Pr = 7.0$) (*a*), (*d*) $t = 0$; (*b*), (*e*) 0.05; (*c*), (*f*) 0.2.

is apparent. In figure 5(*e*), the convective motion becomes so weak that the vortex
structure is no longer visible. Finally, we show the two Nusselt numbers in figure 5(*g*)
in time as the indicator for convective heat transport. The lower (solid) and upper
(dashed) curves are based on the horizontal-mean temperature gradient at the lower
and upper walls, respectively. The gradient is computed normal to the walls. As the
thermal actuator action is switched on, a large transient perturbation develops near
the lower wall, indicating an increase in local heat flux from the actuator action. The
lower Nusselt number shoots up considerably higher than the upper Nusselt number
initially for a brief duration. Subsequently, the upper Nusselt number is greater than
the lower value, as the heat in the bulk of fluid is transferred away. Between $t = 0$
and $t = 0.474$, we determined through integration that the areas under the curves are
0.5635 (solid line) and 0.5628 (dashed line). The two integral values will converge to
the same value in time, as a constraint of the conservation of heat.
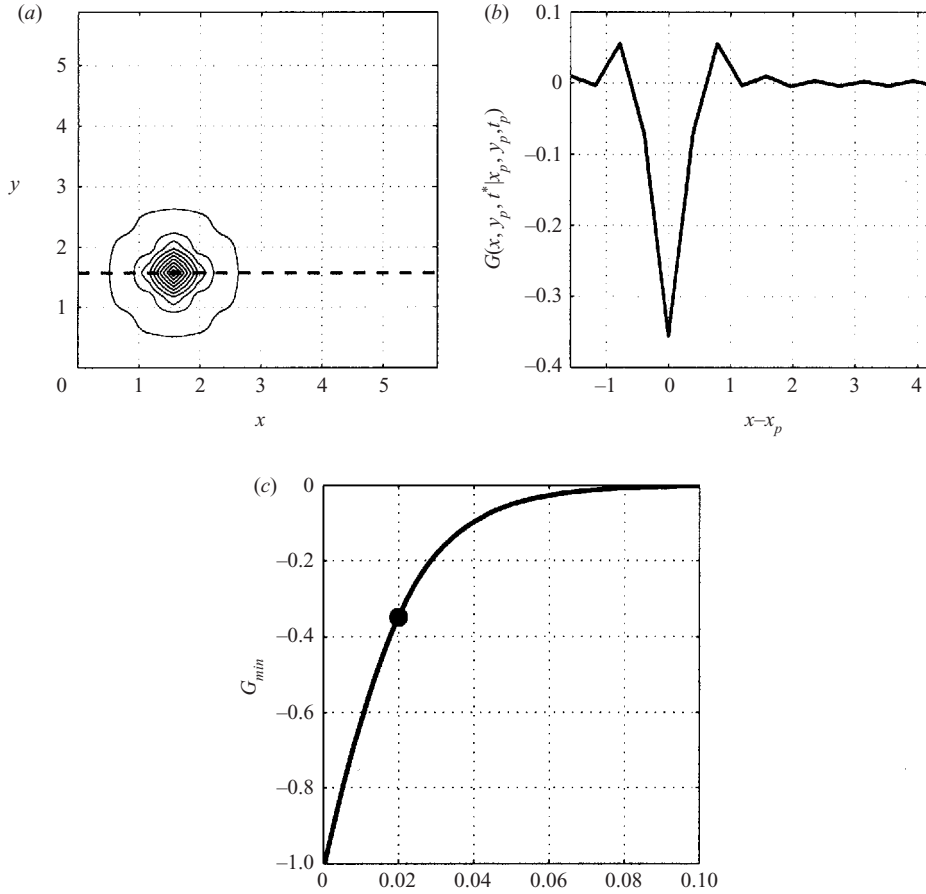
FIGURE 6. (a) Isotherms of the response of temperature on the actuator plane owing to an impulse source temperature on the sensor plane; (b) variation of the response temperature along the dashed line of (a); (c) change of G_{min} with t^*.

For a related drag reduction control problem, Cortelezzi & Speyer (1998) developed a robust reduced-order controller. It is beyond the present scope to consider a reduced-order controller for this nonlinear simulation. Here, on the other hand we determine the spatial roll-off characteristic of the controller based on the Green's function approach. The roll-off characteristics will shed light on the spatial resolution of the arrays of discrete sensors and actuators required for a successful control. A good spatial roll-off implies that relatively few measured points are required to achieve an effective control (see Bamieh & Dahleh 2001). We refer to the description in §2.4. Consider the same case in the numerical simulation for $Pr = 7$ and $Ra = 10^4$ and a length scale of the layer corresponding to $\alpha_x = 1$ and $\alpha_y = 1$. Figure 6(a) shows the contour of the Green's function $G(x, y, t|x_p, y_p, t_p)$, which is the response temperature on the actuator plane $z = 0$ owing to an impulse temperature $\delta(x - x_p)\delta(y - y_p)\delta(t - t_p)$ on the sensor plane $z_s = 0.3$. Here, we let $x_p = 1.5$, $y_p = 1.5$ and $t_p = 0$, $l^* = 20\Delta t$ with $\Delta t = 10^{-3}$. Figure 6(b) shows the response temperature profile as a function of $x - x_p$ along the dashed line designated in figure 6(a). The response temperature corresponds to $G(x, y_p, t^*|x_p, y_p, t_p)$ (with $t^* > t_p$). The result shows that the function has a negative minimum, here denoted by G_{min}. The minimum is collocated horizontally

with the sensor impulse. The negative temperature generated is intended to cancel the disturbance temperature created by the impulsive temperature. Of particular significance is how steep the response curve (in V-shaped) is, implying that the influence zone about the sensor point is small. From figure 6(b), the base width of the V-shape curve is about the width of one roll, assuming that the length scale of the roll does not differ significantly from its critical value. In order for the controller to stabilize the convective disturbance, the spacing between successive points in the array cannot be greater than the effective width of the response temperature.

The plots in figure 6(a)–6(b) represent a snapshot at $t = t^*$. We observed that as t^* increases from 0, the shape and width of the temperature profile (see figure 6b) have changed little, but the magnitude of the minimum decreases rapidly. In figure 6(c), we show the change of the temperature at the minimum, G_{min}, with t^*. The large dot in figure 6(c) denotes the point corresponding to the snapshot of figures 6(a)–6(b). Since the system is diffusive, the response temperature decays monotonically in time, as expected.

4. Experimental considerations

For implementation of the LQG feedback control design, an experiment of RBC is considered. This effort will be guided by the result of the nonlinear simulation, modified for air at room temperature (with $Pr \approx 0.7$) as the working fluid. Although the closed-loop numerical results presented earlier in the paper is for the case $Pr = 7.0$ only, our supplementary analysis completed only recently at $Pr = 0.71$ has revealed that there is no significant difference in the closed-loop response between the two Prandtl numbers for the condition $Ra = 10^4$.

For RBC, previous experiments demonstrate that the initial and onset conditions, as well as the realized convection pattern, are predictable under controlled experimental conditions (Cross & Hohenberg 1993). Complex situations in applications such as variations of material properties, occurrence of concentration gradient and solutal convection, presence of horizontal basic temperature gradient, sidewall effects, defects in pattern, etc., are not included.

In the experimental apparatus, the upper and lower walls will be of two types of material with a large range of heat conductivity. The two walls have large aspect ratio to the layer depth, and may have different thermal boundary conditions. Miniature strain gauge type heaters will be strategically placed at the lower wall as actuator (with separation between heaters determined by the wavelength of the pattern to be controlled). For air, it is convenient to use the holographic interferometry as the sensing technique. Such a sensor can detect temperature differential to high precision. Our LQG controller design has been validated using simulated sensor data. Eventually, for implementation in the experiment, a reduced-order LQG controller will be developed. The three-dimensional pseudospectral model will be modified to accommodate the spatial and temporal dynamics of the sensors and actuators, guided by laboratory observations and the experimental data.

5. Conclusion

The goal achieved in this study is a successful demonstration through numerical simulations that a fully nonlinear steady and preferred state of convection in a horizontal layer of fluid can be reverted to the no-motion state by closed-loop controller action. The simulated results here show the performance of the LQG

controller at $Ra = 10^4$ and $Pr = 7$. At this Ra, the proportional feedback controller is ineffective according to the linear theory. For even higher values of Ra, stabilization is likely to be achievable with the LQG controller by using higher spatial resolution in the simulation, but we have not pushed for that result. The reason is that for realistic modelling at high Ra the effects of the discrete actuator and actuator delay are important considerations as well. Although a general stability proof cannot be inferred from the nonlinear simulation of a few initial conditions, the results do indicate that the linear controller appears quite responsive in suppressing important finite disturbances.

The numerical method used here to develop the nonlinear plant model is pseudospectral spatially. The integration of the model dynamics equation is performed by a time-splitting technique. We have adopted the conventional scheme developed in Marcus (1984) (also see Canuto *et al.* 1986). However, since some significant modification of the scheme has been made, we validate our fully nonlinear three-dimensional plant model by comparing check cases against published results, in particular, from Clever & Busse (1974) and Busse & Clever (1979). The agreement appears reasonably good. Moreover, the direct simulation verifies the results of the weakly nonlinear analysis (Or & Kelly 2001) about the presence of the controlled-induced subcritical g-hexagon solution.

We have also examined the shape function of the actuator response by computing the Green's function of the LQG controller. The shape of the actuation temperature determines the order of the horizontal distance between points of the sensor/actuator arrays in term of the layer gap thickness d. This information is of critical importance when the more realistic pointwise sensor and actuator are used instead of the continuous ones.

REFERENCES

BAMIEH, B. & DAHLEH, M. 2001 Energy amplification in channel flows with stochastic excitation. *Phys. Fluids* **13**, 3258–3269.

BODENSCHATZ, E., PESCH, W. & AHLERS, G. 2000 New developments in Rayleigh–Bénard Convection. *Annu. Rev. Fluid Mech.* 709–778.

BUSSE, F. H. & CLEVER, R. M. 1979 Instabilities of convection rolls in a fluid of moderate Prandtl number. *J. Fluid Mech.* **91**, 319–335.

CANUTO, C., HUSSAINI, N. Y., QUARTERONI, A. & ZANG, T. A. 1986 *Spectral Methods in Fluid Dynamics*. Springer.

CLEVER, R. M. & BUSSE, F. H. 1974 Transition to time-dependent convection. *J. Fluid Mech.* **65**, 625–645.

CORTELEZZI, L. & SPEYER, J. L. 1998 Robust reduced-order controller of laminar boundary layer transition. *Phys. Rev. E* **58**, 1906–1910.

CROSS, M. C. & HOHENBERG, P. C. 1993 Pattern formation outside of equilibrium. *Rev. Mod. Phys.* **65**, no. 3, part 2.

GOTTLIEB, D. & ORSZAG, S. A. 1977 *Numerical Analysis of Spectral Methods: Theory and Applications*. SIAM-CBMS, Philadelphia.

HOWLE, L. E. 1996 A comparison of the reduced Galerkin and pseudospectral methods for simulation of steady Rayleigh–Bénard convection. *Intl J. Heat Mass Transfer* **39**, 2401–2407.

HOWLE, L. E. 1997*a* Linear stability analysis of controlled Rayleigh–Bénard convection using shadowgraphic measurement. *Phys. Fluids* **9**, 3111–3113.

HOWLE, L. E. 1997*b* Control of Rayleigh–Bénard convection in a small aspect ratio container. *Intl J. Heat Mass Transfer* **40**, 817–822.

Howle, L. E. 1997*c* Active control of Rayleigh–Bénard convection. *Phys. Fluids* **9**, 1861–1863.

Howle, L. E. 2000 The effect of boundary properties on controlled Rayleigh–Bénard convection. *J. Fluid Mech.* **411**, 39–58.

Marcus, P. S. 1984 Simulation of Taylor–Couette flow. Part 1. Numerical methods and comparison with experiment. *J. Fluid Mech.* **146**, 45–64.

Or, A. C., Cortelezzi, L. & Speyer, J. L. 2001 Robust feedback control of Rayleigh–Bénard convection. *J. Fluid Mech.* **437**, 175–202.

Or, A. C. & Kelly, R. E. 2001 Feedback control of weakly nonlinear Rayleigh–Bénard–Marangoni convection. *J. Fluid Mech.* **440**, 27–47.

Press, W. H., Teukolsky, S. A., Vetterling, W. T. & Flannery, B. P. 1992 *Numerical Recipes. The Art of Scientific Computing*, 2nd edn. Cambridge University Press.

Rhee, I. & Speyer, J. L. 1991 A game theoretic approach to a finite-time disturbance attenuation problem. *IEEE Trans. Automat. Contr.* **36**, 1021–1032.

Shortis, T. A. & Hall, P. 1996 On the effect of feedback control on Bénard convection in a Boussinseq fluid. *NASA Contractor Rep.* 198280: ICASE Rep. 96-9.

Tang, J. & Bau, H. H. 1993 Stabilization of the no-motion state in Rayleigh–Bénard convection through the use of feedback control. *Phys. Rev. Lett.* **70**, 1795–1798.

Tang, J. & Bau, H. H. 1994 Stabilization of the no-motion state in the Rayleigh–Bénard problem. *Proc. R. Soc. Lond.* A **447**, 587–607.

Tang, J. & Bau, H. H. 1998*a* Experiments on the stabilization of the no-motion state of a fluid layer heated from below and cooled from above. *J. Fluid Mech.* **363**, 153–171.

Tang, J. & Bau, H. H. 1998*b* Numerical investigation of the stabilization of the no-motion state of a fluid layer heated from below and cooled from above. *Phys. Fluids* **10**, 1597–1610.

APPENDIX B:
Gain-Scheduled Controller for the Suppression of Convection at High Rayleigh
Number

Gain-scheduled controller for the suppression of convection at high Rayleigh number

A. C. Or and J. L. Speyer

Department of Mechanical and Aerospace Engineering, University of California, Los Angeles, California 90095-1597, USA
(Received 14 June 2004; revised manuscript received 28 October 2004; published 4 April 2005)

Recent studies in the feedback control of Rayleigh-Bénard convection indicate that one can sustain the no-motion state at a moderate supercritical Rayleigh number (Ra) using only proportional compensation. However, stabilization occurs at a much higher Rayleigh number using linear-quadratic-Gaussian (LQG) control synthesis. The restriction is that the convection model is linear. In this paper, we show that a comparable degree of stabilization is achievable for a fully nonlinear convection state. The process is demonstrated in two stages using a fully nonlinear, 3D Boussinseq model, compensated by a reduced-order LOQ controller and a gain-schedule table. In the first stage a fully-developed convective state is suppressed through the control action at a moderate supercritical Ra. After the residual convection decays to a sufficiently small amplitude, in the second stage, we increase the Ra by a large step and switch the compensator gains using the gain-schedule table. During this change the control action is in place. Our nonlinear simulation results suggest that the nonlinear system can be stabilized to the limit predicted by the linear analysis. The simulation shows that the large Ra jump induces a large transient temperature in the conductive component, which appears to have very small impact on the stabilization.

I. INTRODUCTION

Considerable interest has been demonstrated in the suppression of convection using the optimal control methods [1]. A glimpse at some important results can be found in [2] using the Boussinesq model for Rayleigh-Bénard convection (RBC). The suppression of the onset of RBC by feedback control was investigated through analyses, experiments, and numerical simulations by a number of authors. The results were published in [3–11]. Potential industrial applications of the technique occur in several areas, such as material processing, moulding, and crystal growth. The outlook is encouraging.

The proportional feedback control used by Tang and Bau [3,7,8] and by Howle [4–6,11] offers a simple, intuitive way to control the system. The mechanism of suppression corresponds to the spatial stabilization of the unstable perturbation temperature field by the temperature control. From a control analysis point of view, a proportional control law is often considered insufficient. To account for the complete spatial-temporal dynamics, linear-quadratic-Gaussian (LQG) synthesis offers much better performance, as demonstrated in [1,9,10]. LQG synthesis also provides a systematic and optimal methodology to design a high-order robust compensator that guarantees a certain level of relative stability margins. Furthermore, with LQG synthesis there is an existing body of modern control theory literature to aid in the issues of controller implementation, systematic order reduction, and gain scheduling.

We published two studies in applying the LQG synthesis for controlling RBC. The first study is a closed-loop linear stability analysis [9], in which detailed stability boundary curves were computed. The no-motion state can be stabilized up to 14.5 times the critical Rayleigh number Ra_c for the case of moderate Prandtl number (Pr=7.0). Beyond this limit the LQG controller allows islands of instability to form below Ra=14.5 times of Ra_c.

The linear stability results is very restricted because in real applications convection has finite amplitudes. In the second study, a three-dimensional nonlinear plant model [10] was developed using the pseudo-spectral method. Using LQG synthesis of [9], we demonstrated that a fully nonlinear initial steady convection state at about 6 times the critical Rayleigh number can be damped out by control action. The no-motion state is sustained.

In all the studies [1–10], the measurements and control actions were assumed to be spatially continuous. No sensor or actuator dynamics were included. In a more recent study by Howle [11], it was demonstrated that the finite wall thickness in the boundaries adds additional actuator dynamics and alters the onset mode of instability. Here, this added latency has not been included. This area is of interest for future investigations.

In this study our goal is to demonstrate that a fully non-linear convection state can be suppressed, and the convection-suppressed, no-motion state can be raised to a Ra value comparable to the stability limit dictated by the linear analysis. A two-stage gain-schedule approach is considered here. Furthermore, a reduced-order LQG controller has been developed for this task.

II. 3D NONLINEAR PLANT MODEL

Consider an infinite layer of Boussinesq fluid (see the schematic of Fig. 1). The upper wall is maintained at temperature T_2^* and the lower wall temperature at $T_1^* + \beta \Delta T^* + \theta_c^*$, where $T_1^* > T_2^*$; the flag β is set to zero prior to the step jump in Ra and equal to one after the jump; ΔT^* is the step increase in lower-wall temperature corresponding to the Ra step. These are the conductive components of the temperature. To suppress convection, a temperature control $\theta_c^*(x, y)$ is generated on the actuator plane assumed to coincide with the lower wall. This is a perturbation temperature.
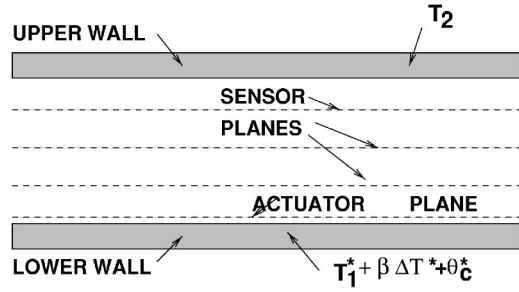
FIG. 1. Schematic of a section of the 3D fluid layer.

There are three embedded sensor planes in the layer, which measure the interior field temperatures at three different levels, $z_s^{(i)}$ $(i=1,2,3)$. The perturbation sensor temperatures from the conductive component are denoted as $\theta_s^*(x,y,z_s^{(i)})$.

Due to the step increase in Ra, a transient temperature is generated in the conductive component of the total temperature after the step increase. The heat equations for the static conductive temperature and transient conductive temperature, and for the perturbation temperature due to convection are derived from first principles in the Appendix. In the presence of convection, the total temperature is decomposed into the conductive and convective components. The conductive temperature has a transient component as well. The nominal conductive temperature is the static component. The conductive temperature field is stable. The convective temperature has a nominal of zero. The control loop is designed to drive this perturbation component to zero. In the nondimensional mathematical form, the quantities d, d^2/κ, κ/d, κ/d^2, $\rho(\kappa/d)^2$, and $(T_1^*-T_2^*)$ (before the Ra step) and $(T_1^*+\Delta T^* -T_2^*)$ (after the Ra step), are used as the scales of length, time, velocity, vorticity, pressure, and temperature, where d is the layer thickness, κ and ρ are the mean thermal diffusivity and density of the fluid.

The governing nondimensional Oberbeck-Boussinesq equations are

$$\mathrm{Pr}^{-1}\partial_t \mathbf{v} = \mathrm{Pr}^{-1}\mathbf{v}\times\boldsymbol{\omega} + \mathbf{k}\mathrm{Ra}\theta - \boldsymbol{\nabla}\pi_e + \nabla^2 \mathbf{v}, \qquad (1)$$

$$\partial_t \theta = -\mathbf{v}\cdot\boldsymbol{\nabla}\theta + w(1-\partial_z\widetilde{\Theta}) + \nabla^2\theta, \qquad (2)$$

$$\partial_t\widetilde{\Theta} = \partial_{zz}^2\widetilde{\Theta}, \qquad (3)$$

$$\boldsymbol{\nabla}\cdot\mathbf{v} = 0, \qquad (4)$$

where $\mathbf{v}=(u,v,w)$ is the velocity vector field, $\boldsymbol{\omega}=\boldsymbol{\nabla}\times\mathbf{v}$ is the vorticity, $\pi_e=\pi+\mathbf{v}\cdot\mathbf{v}/2$ is the effective pressure head, $\widetilde{\Theta}(z,t)$ is the transient component in the conductive temperature, θ is the perturbation temperature due to convection, and $\mathbf{k}$ is unit vector in the z direction. The two external parameters are the Rayleigh number and the Prandtl number, respectively, defined by $\mathrm{Ra}=\alpha g\Delta T^* d^3/\nu\kappa$ and $\mathrm{Pr}=\nu/\kappa$ where α is the coefficient of thermal expansion and ν is the mean kinematic viscosity. The continuity equation (4) is for an incompressible flow.

The upper and lower wall velocity field conditions are nonpermeable and nonslip,

$$\mathbf{v}(x,y,0,t) = \mathbf{0}, \quad \mathbf{v}(x,y,1,t) = \mathbf{0}. \qquad (5)$$

The upper and lower wall transient conductive temperatures have a zero initial condition before the step jump, since the layer is in a steady state heat conduction prior to the step increase of Ra. After the step increase, at $t=t^+$, the initial condition for $\widetilde{\Theta}$ is given by

$$\widetilde{\Theta}(z,t^+) = -\frac{\Delta T^*(1-z)}{(T_1^*+\Delta T^*-T_2^*)}. \qquad (6)$$

The boundary conditions are homogeneous,

$$\widetilde{\Theta}(0,t) = 0, \quad \widetilde{\Theta}(1,t) = 0. \qquad (7)$$

The upper-wall boundary condition for the perturbation temperature is homogeneous. The lower-wall boundary condition for the perturbation temperature includes the temperature control $\theta_c(x,y,t)$, which is generated by the actuator action. The upper and lower thermal boundary conditions for the perturbation temperature are

$$\theta(x,y,1,t) = 0, \quad \theta(x,y,0,t) = \theta_c(x,y,t). \qquad (8)$$

The temperature field is measured on the three embedded sensor planes at the levels $z=z_s$ $(s=1,2,3)$. Since the conductive temperature field in the layer can be determined independently, we can subtract it from the total to obtain the perturbation temperature measurements. The perturbation sensor temperature measurements are

$$\theta_s(x,y,t) = \theta(x,y,z_s,t), \quad s=1,2,3. \qquad (9)$$

In the numerical scheme the three-dimensional (3D) dependent variables u, v, w, p, and θ are expressed by the following finite triple sums:

$$\begin{bmatrix} u \\ v \\ w \\ p \\ \theta \end{bmatrix}(x,y,z,t) = \mathrm{Re}\left\{ \sum_{n=0}^{N}\sum_{k=0}^{K}\sum_{m=-M+1}^{M} \begin{bmatrix} u_{kmn} \\ v_{kmn} \\ w_{kmn} \\ p_{kmn} \\ \theta_{kmn} \end{bmatrix}(t)T_n \right.$$
$$\left. \times(z)e^{i(k\alpha_x x+m\alpha_y y)} \right\}. \qquad (10)$$

where Re denotes the real part of the sum; α_x and α_y are the fundamental wave numbers in the x and y directions, respectively. The two fundamental wave numbers are prescribed. Here, the number of total coefficients can be reduced to half by only including the coefficients for $k\geq 0$, because all the dependent variables are real (see detailed description in [10]). The functions $T_n(z)$ $(n=0,1,\dots)$ denote the Chebyshev polynomials. A linear coordinate transformation is used to convert the Chebyshev function domain from the function domain $-1\leq z<1$ to our physical domain $0\leq z<1$. The per-

turbation temperature control θ_c and measurement temperatures θ_s ($s=1,2,3$), are planar. They are expanded as double sums,

$$
\begin{bmatrix} \theta_s(z_1,t) \\ \theta_s(z_2,t) \\ \theta_s(z_3,t) \\ \theta_c(0,t) \end{bmatrix}(x,y,t) = \mathrm{Re}\left\{ \sum_{k=0}^{K}\sum_{m=-M+1}^{M} \begin{bmatrix} \theta_{km,s}(z_1,t) \\ \theta_{km,s}(z_2,t) \\ \theta_{km,s}(z_3,t) \\ \theta_{km,c}(0,t) \end{bmatrix} \right.
$$
$$
\left. \times e^{i(k\alpha_x x + m\alpha_y y)} \right\}. \tag{11}
$$

III. THE REDUCED-ORDER LQG COMPENSATOR

The LQG synthesis method was discussed in detail in [9]. In the study, the LQG compensator used is full ordered, that is, the compensator has the same order as the 3D nonlinear convection model. The controller was demonstrated to be effective in removing the convection state, reverting the layer back to its no-motion state for $\mathrm{Ra}=10^4$, about 5.8 times the critical value. In this paper, the full-order compensator is replaced by a reduced-order compensator. A methodology for increasing Ra was developed without destabilizing the controlled state. This is a gain scheduling approach.

To design a reduced-order compensator, the linear Boussinesq equations are expressed in a state-space form for each Fourier-decomposed mode [corresponding to wave numbers $(k\alpha_x, m\alpha_y)$]. The state-space system includes the corresponding measurement (sensor) equations and the control (actuator) equations. We remark that these are the linearized equations about the no-motion state, not about the nonlinear convective state. For the simplicity of notations, the indices for the wave numbers are omitted. It is clear that there is a distinct set of state-space equations for each pair of wave numbers for each Fourier mode for each Rayleigh number. The state space equation is expressed as

$$\dot{\mathbf{x}} = \mathbf{A}\mathbf{x} + \mathbf{B}\mathbf{u}, \tag{12}$$

where the state vector $\mathbf{x}$ consists of the Chebyshev coefficients for the velocity and the temperature perturbations for wave number pair $(k\alpha_x, m\alpha_y)$; u is the Fourier coefficient of the temperature control according to Eq. (11). The sets of state space equations (12) corresponding to different wave-number pairs are decoupled in a linear sense.

From Eqs. (11) and (10), we denote the measurement temperature Fourier coefficients by the three-row vector $\mathbf{z}$; $\mathbf{z}$ consists of measurement on 3 planes z_1, z_2, z_3, which can be expressed in terms of the state vector by the matrix equation

$$\mathbf{z} = \mathbf{C}\mathbf{x}. \tag{13}$$

We show a block diagram for the control loop between the compensator and the plant model by a schematic in Fig. 2. The LQG compensator consists of a Kalman filter and an optimal regulator. The fixed-gain Kalman filter equation and the optimal regulator equation are, respectively,
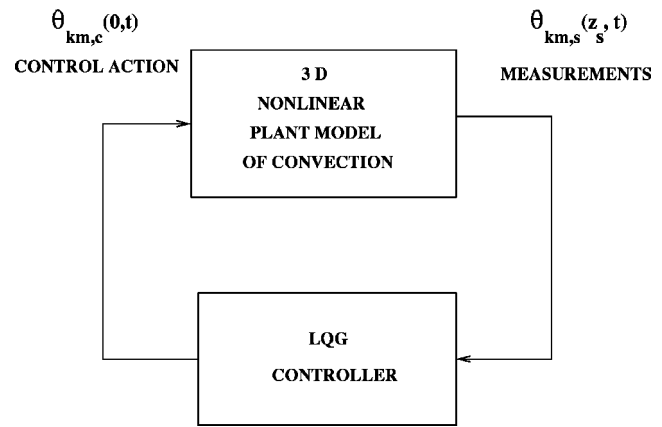

FIG. 2. The control loop diagram.

$$\dot{\hat{\mathbf{x}}} = \mathbf{A}\hat{\mathbf{x}} + \mathbf{B}\mathbf{u} + \mathbf{K}_f(\mathbf{z}-\hat{\mathbf{z}}), \quad u=-\mathbf{K}_c\hat{\mathbf{x}}, \tag{14}$$

where vector $\hat{\mathbf{x}}$ consists of the state estimates. The following measurement equation relates the estimates of measurements to the estimates of the true states,

$$\hat{\mathbf{z}} = \mathbf{C}\hat{\mathbf{x}}. \tag{15}$$

The steady-state Kálman gain vector $\mathbf{K}_f$ and the regulator gain vector $\mathbf{K}_c$ are determined from two steady-state algebraic Riccati equations (AREs) [1,9].

To determine the controller gain $\mathbf{K}_c$, the states $\mathbf{x}$ and control u are quadratically penalized in an integral cost criterion. The associated weightings are used in the controller AREs. To determine the filter gain $\mathbf{K}_f$, we assumed that Gaussian noises are added to the dynamics and the measurements. The power spectral densities are used as the design parameters in the AREs to form the gains. The LQG compensator at each Ra number consists of $2(K+1)M$ sets of state space matrices $(\mathbf{A}, \mathbf{B}, \mathbf{C}, \mathbf{D})$ (where $\mathbf{D}=\mathbf{0}$), and the same number of sets of gains $\mathbf{K}_f, \mathbf{K}_c$. There is no cross coupling between the sets of equations. Each set is designed to compensate for a Fourier mode corresponding to a wave number pair. In the full-order controller formulation, the dimension of $\mathbf{A}$ ranges from 64 to 128, K and M range from 32 to 64. The compensator becomes very large.

We have considered two different approaches to design the order-reduced compensator. The first approach is to seek a balance between the input and output relationships of the plant model. The second approach is to seek a balance between the input and output relationships of the compensator. The state space system is first transformed to a Schur canonical form and then ordered block by block in a balanced realization scheme (grammian-based). The reduced-order compensator is then constructed based on the reduced-order dynamics and their input-output relationships.

The first approach appeared to be quite effective when applied to controlling the laminar boundary layer transition [12]. However, when applied to Rayleigh-Bénard convection, the reduced-order compensator is not as robust as it should be. Some preliminary simulation results indicate that an order reduction by a factor of 2 is possible. Further reduction makes the closed-loop response unstable.

The first approach is not robust. Our ultimate goal is to use a reduced-order compensator to control a full-order non-linear plant model. The reason that we perform a balance realization on the linearized plant model, and then truncate the plant model, is because we want to use the reduced-order linear plant model to design the reduced-order compensator. In the second approach, we do not truncate the plant model. We first design a full-order compensator for the full-order plant model, just as in [9]. Then, we seek to perform a balance realization on the compensator instead, and then truncate compensator model. By doing that we have to compute the full-order Kalman gains $\mathbf{K}_f$ and full-order regulator gain $\mathbf{K}_c$ based on the full-order plant model with state space ($\mathbf{A}$, $\mathbf{B}$, and $\mathbf{C}$). Then, we perform a balance realization on the compensator input and output. The compensator inputs the measurement vector $\mathbf{z}$ and outputs the control vector $\mathbf{u}$.

From Eq. (14), we obtain the following state space equations for the full-order compensator,

$$\dot{\hat{\mathbf{x}}} = \mathbf{A}_c\hat{\mathbf{x}} + \mathbf{B}_c\mathbf{z},$$

$$\mathbf{u} = \mathbf{C}_c\hat{\mathbf{x}} + \mathbf{D}_c\mathbf{z}. \qquad (16)$$

The subscript "c" denotes the compensator, where the state space matrices are given by

$$\mathbf{A}_c = \mathbf{A} - \mathbf{B}\mathbf{K}_c - \mathbf{K}_f\mathbf{C} + \mathbf{K}_f\mathbf{D}\mathbf{K}_c,$$

$$\mathbf{B}_c = \mathbf{K}_f, \quad \mathbf{C}_c = -\mathbf{K}_c, \quad \mathbf{D}_c = \mathbf{0}, \qquad (17)$$

where $\mathbf{D}_c = \mathbf{0}$. To reiterate, in the first approach the balance realization is performed on ($\mathbf{A}, \mathbf{B}, \mathbf{C}$). In the second approach, the balance realization is performed on ($\mathbf{A}_c, \mathbf{B}_c, \mathbf{C}_c, \mathbf{D}_c$) instead. It is worth noting that the dynamics of $\mathbf{A}_c$ can be distinctively different from those of $\mathbf{A}$. The compensator dynamics now depends on the gain vectors as the input and output matrices.

A grammian-based balance realization is just one way to perform the balancing. A typical grammian-based routine is by solving the Lyapunov-type equations using the polynomial methods. The polynomial routines are not effective for large matrices. Here, we consider an approximate method. First, we apply a similarity transformation $\mathbf{x} = \mathbf{P}\mathbf{x}_1$, in which the transformation $\mathbf{P}$ diagonalizes $\mathbf{A}_c$. This transformation converts ($\mathbf{A}_c, \mathbf{B}_c, \mathbf{C}_c, \mathbf{D}_c$) into ($\mathbf{A}_{c1}, \mathbf{B}_{c1}, \mathbf{C}_{c1}, \mathbf{D}_{c1}$). If there are nondistinct eigenmodes, then we have to use the Schur canonical transformation instead. The transformation is

$$\mathbf{A}_{c1} = \mathbf{P}^{-1}\mathbf{A}_c\mathbf{P}, \quad \mathbf{B}_{c1} = \mathbf{P}^{-1}\mathbf{B}_c,$$

$$\mathbf{C}_{c1} = \mathbf{C}_c\mathbf{P}, \quad \mathbf{D}_{c1} = \mathbf{D}_c, \qquad (18)$$

where $\mathbf{A}_{c1}$ is now in a diagonal form. We denote the diagonal entries of this matrix by λ_i ($i = 1, 2, \ldots, N$). We allow the diagonal entries to be expressed in complex conjugate pairs.

Second, we define a score parameter for each compensator mode, denoted as σ_i ($i = 1, 2, \ldots, N$), where

$$\sigma_i = |\mathbf{b}_i||\mathbf{c}_i|/|\lambda_i|, \quad i = 1, 2, \ldots, N, \qquad (19)$$

$\mathbf{b}_i$ is the ith row of $\mathbf{B}_{c1}$ and $\mathbf{c}_i$ is the ith column of $\mathbf{C}_{c1}$. Then we perform a reordering, in which the eigenmodes in

($\mathbf{A}_{c1}, \mathbf{B}_{c1}, \mathbf{C}_{c1}, \mathbf{D}_{c1}$) are ranked according to the magnitude of the score parameter. The modes are arranged in the order of importance. The unimportant modes at the end will be truncated. A truncated, reduced-order set is denoted by ($\mathbf{A}_{c2r}, \mathbf{B}_{c2r}, \mathbf{C}_{c2r}, \mathbf{D}_{c2r}$), with the state vector $\mathbf{x}_{1r}$ (subscript "r" stands for reduced-order set).

The reduced-order compensator is described by

$$\dot{\hat{\mathbf{x}}}_{1r} = \mathbf{A}_{c2r}\hat{\mathbf{x}}_{1r} + \mathbf{B}_{c2r}\mathbf{z},$$

$$\mathbf{u} = \mathbf{C}_{c2r}\hat{\mathbf{x}}_{1r} + \mathbf{D}_{c2r}\mathbf{z}. \qquad (20)$$

IV. RESULTS

The preferred convection pattern is steady, two-dimensional (2D) finite-amplitude rolls. We start at $Ra = 10^4$ and use the steady convection rolls as the initial condition. Although the preferred wavenumber of the rolls is about 3.1, in our simulation, the fundamental wavenumbers are chosen to be at $\alpha_x = 1.0$ and $\alpha_y = 1.0$. So, the steady rolls occur as the longitudinal rolls (parallel to y axis) in the second Fourier harmonic. Three-dimensional zero-mean Gaussian noises (zero mean, standard deviation equal to 10^{-6}) are added to each coefficient in the initial fields. This ensures that if 3D instabilities occur, there exists perturbations for them to grow. The full-order nonlinear plant model has a resolution of 2×128 Chebyshev modes in the vertical direction (for both vertical velocity and temperature) and 32×32 Fourier modes in the horizontal direction. Note that the horizontal velocity is obtainable from the vertical velocity through the continuity equation. In the reduced-order compensator, only eight Chebyshev modes (complex) are retained. The same number of Fourier modes is used in the horizontal direction. The analysis shows that 8 Chebyshev modes is the minimum for effective control.

A. Closed-loop simulation prior to the Ra increase

The first-stage of simulation is performed using the first set of gains in the gain-schedule table. The simulation is performed until the residual convection is sufficiently small. The simulation shows that a time period of 0.4 unit is sufficient for the purpose. With a time step of $\Delta t = 0.0004$, we sample the output every five time steps. The maximum temperature control recorded occurs right at the start, i.e., at $t = 0.004$. The temperature control produces a sharp peak in the transient phase of roughly 0.15 time unit wide. This peak has a maximum roughly of 1.3 times the conductive temperature difference imposed across the upper and lower walls, that is, ΔT. This $1.3\Delta T$ may be considered high for experimental implementations. It all depends on the saturation limit of the actuator. If saturation occurs, then we have to reduce the Ra value of the initial condition.

The question of using a linear controller to control a nonlinear system needs an explanation. In fact, the linear system consists of only the one Fourier mode. Therefore, in the linear sense the controller is a single-mode controller [3–6,9]. The nonlinear system consists of an infinite number of Fourier modes, all except one are generated by the nonlinear
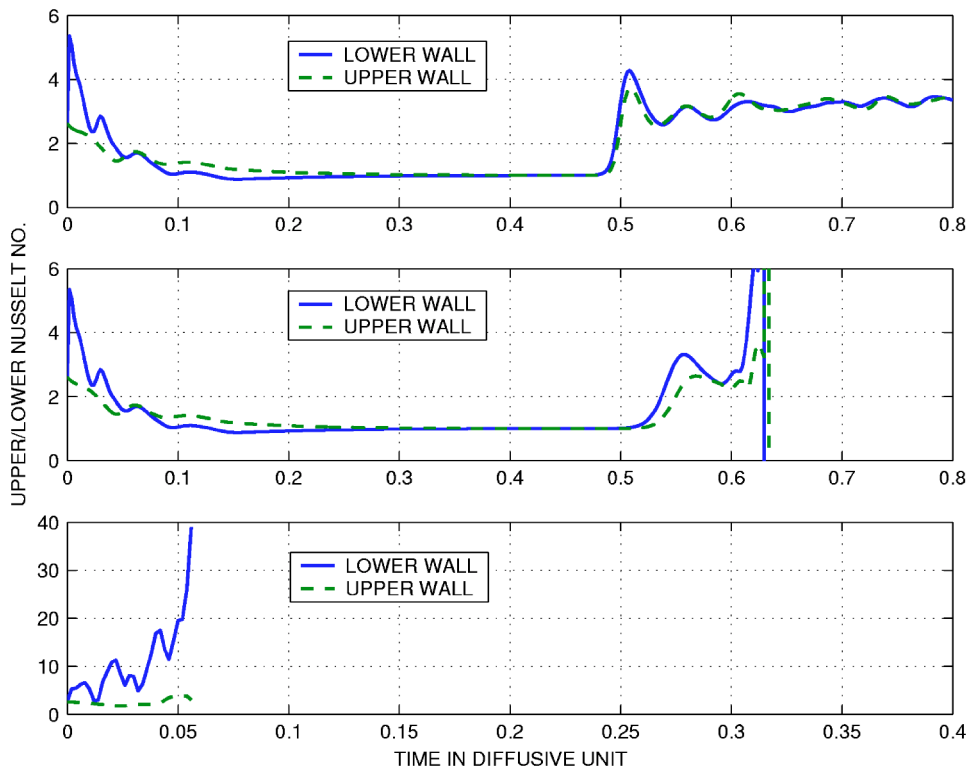
FIG. 3. Closed-loop responses on three test cases.

terms. Other than the Fourier modes, there always exists a mean temperature field as well. The linear controller controls each Fourier mode, as well as the mean field, individually. Even though each mode is treated as linear by the controller, a linear controller has been proven effective. In fact, it should be effective, as long as the higher-order terms in the amplitude expansion corresponding to a particular Fourier mode is either stabilizing or insignificant. Therefore, the temperature control containing a horizontal mean component is obvious but was not explicitly mentioned in [9]. This mean component is reasonably large too. At the peak of the temperature control, this component is about $-0.35\Delta T$. It tends to zero as convection is suppressed.

The Nusselt number Nu is defined as the ratio of the total (convective and conductive) to the purely conductive heat transfer. This parameter is a measure of the degree of convective activities. In the closed-loop response, it is also a measure of the effectiveness of the controller. In Figs. 3 and 4, the Nusselt numbers at the lower wall (Nu_1, solid line) and upper wall (Nu_2, dashed line) are plotted as functions of time. When $Nu_1=Nu_2=1.0$, the layer is purely conductive, i.e., there is no convection motions. However, the conductive state can be transient. When $Nu_1>Nu_2$, relative to conduction, net heat is pumped into the layer via the lower wall. This situation is observed at the beginning of the closed-loop simulation (for time less than 0.07) in every case, indicating that the controller starts by pumping net heat into the layer. When $Nu_2>Nu_1$, net heat (relative to conduction) is extracted from the layer. It is possible for the transience to cause $Nu_1<1.0$ as convection is damping out, as seen in the conductive case (see Fig. 4). At small convection amplitude (as the Nusselt number approaches 1.0), the nominal simulation (see Fig. 4) shows that the upper-wall Nusselt number

has value greater than 1.0 and the lower-wall Nusselt number has value less than 1.0. This linear behavior shows that the controller action is to extract net heat (relative to conduction) from the layer, thereby reducing the convection energy.

B. Gain scheduling, Ra stepping and the transient response of the conductive temperature

The gain scheduling is a means to allow the filter and control gains to vary during the closed-loop simulation. Typically, a gain table is constructed. The Ra range is divided into intervals. Each interval corresponds to a new set of gains. In the simulation, as Ra is increased through the intervals in time, the gains are switched to preserve the control performance. For implementation, it is more convenient to increase Ra by steps. A step jump causes transience in the conductive temperature component. This may in turn cause perturbations in the convective field. In this study, we consider only a two-interval gain-table, since each set of gains is extremely large even for the reduced-order controller [32×32 sets of reduced-order state space ($\mathbf{A}, \mathbf{B}, \mathbf{C}, \mathbf{D}$)]. We use a large step increase in Ra to assess the performance. The key, however, is not to destabilize the closed-loop system.

In the simulation we consider a step increase of Ra from 10^4 to 2×10^4. The simulation following the step at $t=t^+$ $=0.4$ unit continues for 0.4 time unit. The total simulation time is 0.8 unit.

Before performing the nominal simulation, we consider three test cases (shown in the three panels of Fig. 3). The purpose of the tests is for sanity checks and also for a better understanding of the closed-loop response in general. In the test case 1 (see Fig. 3, upper panel), the control action is disconnected right after the Ra step increase at $t=t^+=0.4$.
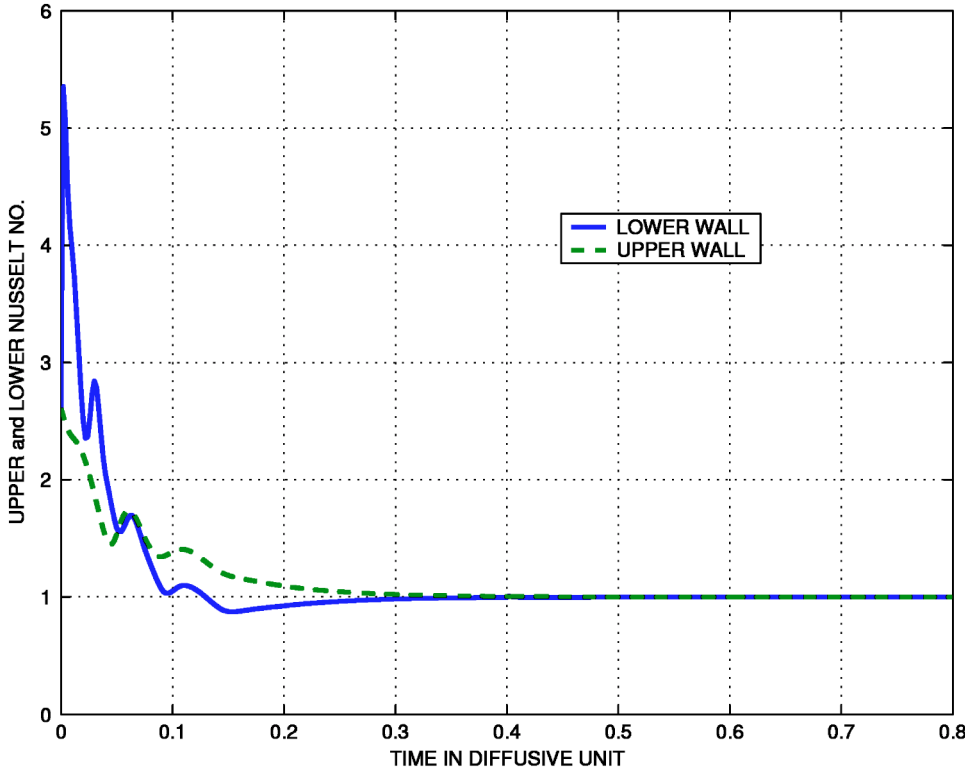
FIG. 4. Closed-loop upper and lower Nusselt numbers.

The remaining simulation has no feedback control. The key observation is that it takes a long duration for convection to build up again. Eventually, the layer has reverted the suppressed state to full-blown, finite-amplitude steady-state of convection. The behavior is indicated by the Nu_2 (dashed line) and Nu_1 (solid line). The curves converge to its steady state value at about 3.0.

In the test case 2 we maintain a closed loop throughout the simulation. However, we do not switch the gains at the step increase of Ra. Figure 3 (the middle panel) shows that the original set of gains is ineffective to maintain the no-motion state. Even worse than the test case 1, the closed loop response displays finite-time divergence. In this case, the system does not settle to a steady state. It blows up.

A set of gains designed at a higher Ra is not necessarily effective to control the layer at a lower Ra. In the test case 3, we use the second set of gains (designed at $Ra = 2 \times 10^4$) to control convection before the Ra step increase (the steady state at $Ra = 10^4$). The result (Fig. 3, lower panel) shows that the closed loop response is divergent.

Finally, we turn to the nominal case of the two Ra-step simulation. In this case, we use the gains according to the gain table. show the closed-Loop response in Fig. 4. At $t = t^+ = 0.4$, we see a very small kink in the solid curve corresponding to Nu_1, due to the transient conductive temperature. The important observation is that the transient conductive temperature has very little impact on the residual convection.

Unfortunately, the Nusselt number plots do not show the detailed transience of the residual convection on the scale used to plot Fig. 4. It is of interest to show the control temperature θ_c in the closed-loop response. Referring to Eq. (11), we define the plotted quantity $\|\theta_c\|$ as

$$\|\theta_c\| = \left\{ \sum_{k=0}^{K} \sum_{m=-M+1}^{M} \theta_{km,c}(0,t)\overline{\theta_{km,c}(0,t)} \right\}^{1/2} . \quad (21)$$

This measure is plotted in a semilogarithm scale (see Fig. 5). The regions of steep slopes indicate locations where a cross over zero has occurred. The maximum of the mean temperature control occurs at the beginning of the simulation. The maximum value is 1.27. Near $t = 0.4$, a distinct jump is observed. This is due to the conductive temperature transience caused by the step increase in Ra. The dominant coefficient (greater than 96% of the norm, corresponds to the coefficient for $k = 3$ and $m = 0$, as expected. This coefficient represents the longitudinal convection rolls at a wave number 3.0, as prescribed. All the coefficients for $m \neq 0$ vanish. The results suggest that a large step increase of Ra is benign. The large transient conductive temperature does not destabilize the closed-loop system.

In Fig. 6, we plot the transient conductive temperature, $\widetilde{\Theta}(z,t) = \Theta(z,t) - \Theta_{ss}(z)$ at several time points, at $t = 0.4$, 0.48, 0.56, and 0.72. The quantity converges to zero fairly rapidly.

V. CONCLUSIONS

In this study two important steps have been advanced using a robust control synthesis for the problem of suppression of convection: (i) a reduced-order compensator and (ii) a simulation based on a two-step gain-schedule table. For compensator order reduction, the simulation results show that eight Chebyshev modes is the minimum for an effective performance. In stepping the Ra by a large increment using the gain schedule table, an interesting observation is that a large
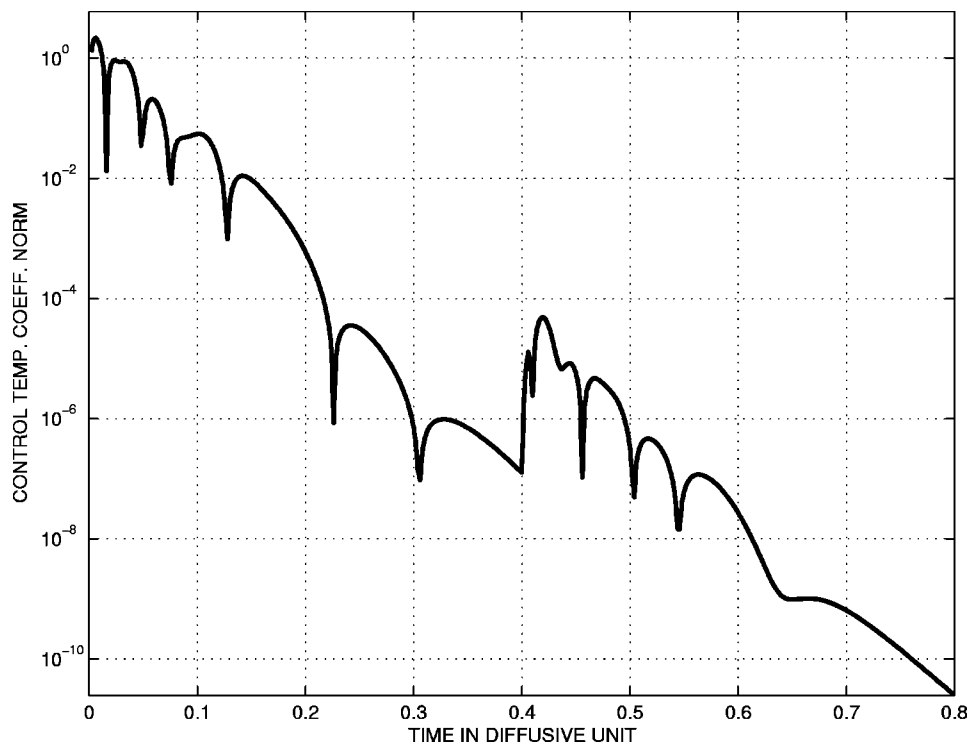
FIG. 5. Norm of closed-loop control temperature coefficients.

Ra step is accompanied by a large transient conductive temperature, but does not cause a significant transient response in the convective fields. As long as the residual convection prior to the step jump of Ra remains small, the destabilizing effects of the transient conductive temperature is insignificant. In this study the two-step Ra gain table used for demonstration purpose. A more refined, multistep gain table may be necessary for laboratory implementations. In conclusion, to suppress a fully nonlinear convection, the gain-schedule approach is a means to achieve a performance up to the linear stability limit.
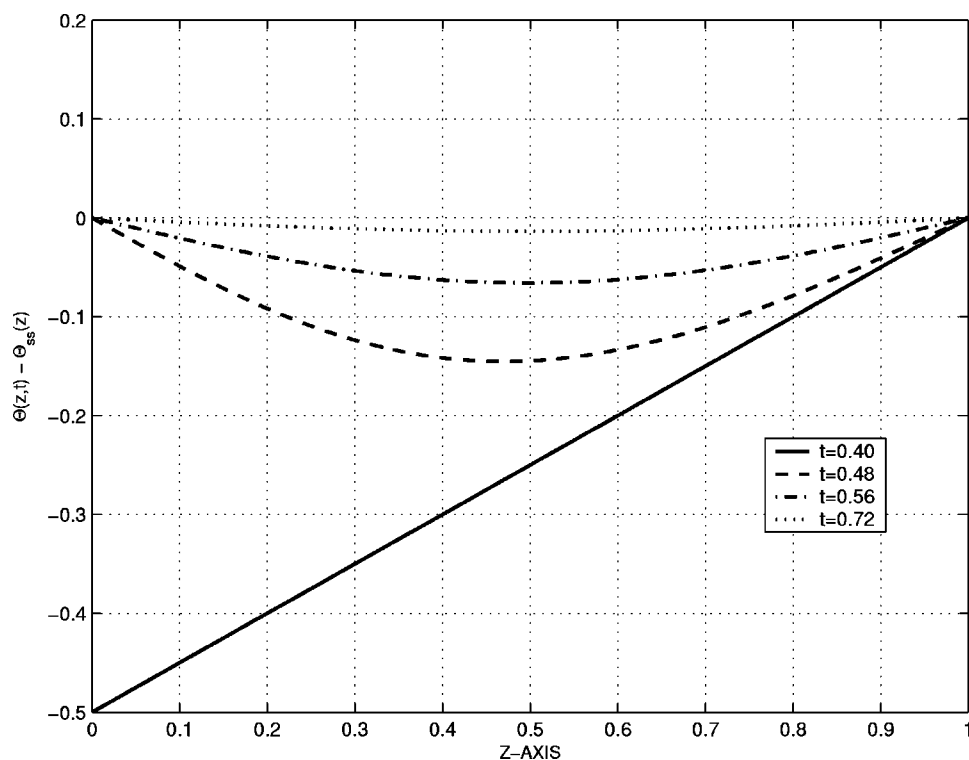
ACKNOWLEDGMENT

FIG. 6. Time plot of the transient conductive temperature.

APPENDIX: DERIVATION OF THE MODEL EQUATIONS

The dimensional form of the Boussinesq system consists of the momentum equation,

$$\partial_t \mathbf{v}^* + \mathbf{v}^* \cdot \boldsymbol{\nabla} \mathbf{v}^* = \frac{1}{\rho} \boldsymbol{\nabla} (p^* + \rho g z) - \alpha g (T_0^* - T^*) \mathbf{k} + \nu \nabla^2 \mathbf{v}^*,$$

(A1)

where in the buoyant force term, T_0^* is a reference temperature (at $z=0$). The heat equation is

$$\partial_t T^* + \mathbf{v}^* \cdot \boldsymbol{\nabla} T^* = \kappa \nabla^2 T^*.$$

(A2)

The velocity field $\mathbf{v}^* = (u^*, v^*, w^*)$ satisfies the incompressibility condition

$$\boldsymbol{\nabla} \cdot \mathbf{v}^* = 0.$$

(A3)

We use (x, y, z) and t to denote dimensional as well as nondimensional Cartesian coordinates and time for simplicity. The asterisk highlights dimensional variables. For nondimensionalization the layer thickness d and d^2/κ are used for scaling length and time; ν and κ denote the viscous and thermal diffusivity, respectively; ρ is the mean density of the fluid; α is the coefficient of thermal expansion and g is the gravitational acceleration. The upper (at $z=1$) and lower (at $z=0$) walls of the layer are prescribed, respectively, at temperatures T_2^* and T_1^* with $T_1^* > T_2^*$.

The fluid temperature, $T^*(x, y, z, t)$, is decomposed into a conductive temperature $\Theta^*(z, t)$ and a convective (perturbation) temperature $\theta(x, y, z, t)$,

$$T^*(x, y, z, t) = \Theta^*(z, t) + \theta^*(x, y, z, t).$$

(A4)

For most studies in RBC, a static (nominal) state is used,

$$\Theta^* = \Theta_{ss}^* = T_1^* - (T_1^* - T_2^*) z.$$

(A5)

For $Ra > Ra_c$, the steady perturbation temperature $\theta^* \neq 0$ does not vanish.

Here the full set of equations are rederived for the case when the conductive temperature is not in a steady state. The gain schedule algorithm is applied, when the Rayleigh number is increased incrementally in steps. Consider the conductive state to be static as described by Eq. (A5) at $t = t^-$. In the closed-loop response $\theta(x, y, z, t) \approx 0$ as convection is suppressed. At $t = t^+$ the lower wall temperature is increased to $T_1^* + \Delta T^*$, where $t^- \approx t^+$. The conductive temperature after the jump is given by

$$\Theta^*(z, t) = \Theta_{ss}^*(z) + \widetilde{\Theta}(z, t),$$

(A6)

$$\Theta_{ss}^*(z) = (T_1^* + \Delta T^*) - (T_1^* + \Delta T^* - T_2^*) z.$$

The transient conductive temperature $\widetilde{\Theta}(z, t)$ is governed by

$$\partial_t \widetilde{\Theta}^* = \kappa \partial_{zz}^2 \widetilde{\Theta}^*,$$

(A7)

subjected to initial and boundary conditions

$$\widetilde{\Theta}^*(z, 0) = -\Delta T^*(1 - z), \quad \widetilde{\Theta}^*(0, t) = 0, \quad \widetilde{\Theta}^*(1, t) = 0.$$

(A8)

Next, we incorporate the decomposed temperatures into the governing equations (A1) and (A2). The conductive temperature is balanced by pressure. Equation (A1) gives

$$\partial_t \mathbf{v}^* + \mathbf{v}^* \cdot \boldsymbol{\nabla} \mathbf{v}^* = -\frac{1}{\rho} \boldsymbol{\nabla} (\pi^*) + \alpha g \theta^* \mathbf{k} + \nu \nabla^2 \mathbf{v}^*,$$

(A9)

$$\pi^* = p^* + \rho g z + \int_0^z [\Theta^*(0, t) - \Theta^*(z', t)] dz'.$$

This equation has the same form regardless of the conductive temperature. Separating the total temperature into the conductive and perturbation components, the heat equation becomes

$$\partial_t \theta^* + \mathbf{v}^* \cdot \boldsymbol{\nabla} \theta^* = -w^* \partial_z \Theta^* + \kappa \nabla^2 \theta^*.$$

(A10)

Equations (A3), (A7), (A9), and (A10) provide the governing equations.

Introducing the nondimensional scaling, the full nondimensional governing equations of the plant model are

$$Pr^{-1}(\partial_t \mathbf{v} + \mathbf{v} \cdot \boldsymbol{\nabla} \mathbf{v}) = -\boldsymbol{\nabla} \pi + Ra \, \theta \mathbf{k} + \nabla^2 \mathbf{v},$$

(A11)

$$\boldsymbol{\nabla} \cdot \mathbf{v} = 0,$$

(A12)

$$\partial_t \theta + \mathbf{v} \cdot \boldsymbol{\nabla} \theta = w(1 - \partial_z \widetilde{\Theta}) + \nabla^2 \theta,$$

(A13)

$$\partial_t \widetilde{\Theta} = \partial_{zz}^2 \widetilde{\Theta}.$$

(A14)

In the gain schedule approach, the step increase in Ra imparts a discontinuity in the thermal field of the system. This condition translates an initial condition for the conductive temperature at $t = t^+$,

$$\widetilde{\Theta}(z, t^+) = -\frac{\Delta T^*(1 - z)}{(T_1^* + \Delta T^* - T_2^*)}.$$

(A15)

Thus a transient response follows each jump $\widetilde{\Theta}$ where $\widetilde{\Theta} \rightarrow 0$ as the conductive temperature approaches steady state.

[1] A. E. Bryson and Y. C. Ho, *Applied Optimal Control* (Hemisphere, New York, 1975).

[2] M. C. Cross and P. C. Hohenberg, Rev. Mod. Phys. **65**, 851 (1993).

[3] J. Tang and H. H. Bau, Proc. R. Soc. London, Ser. A **447**, 587 (1994).

[4] L. E. Howle, Phys. Fluids **9**, 3111 (1997).

[5] L. E. Howle, Int. J. Heat Mass Transfer **40**, 817 (1997).

[6] L. E. Howle, Phys. Fluids **9**, 1861 (1997).

[7] J. Tang and H. H. Bau, J. Fluid Mech. **363**, 153 (1998).

[8] J. Tang and H. H. Bau, Phys. Fluids **10**, 1597 (1998).

[9] A. C. Or, L. Cortelezzi, and J. L. Speyer, J. Fluid Mech. **437**, 175 (2001).

[10] A. C. Or and J. L. Speyer, J. Fluid Mech. **483**, 111 (2003).

[11] L. E. Howle, J. Fluid Mech. **411**, 39 (2000).

[12] L. Cortelezzi and J. L. Speyer, Phys. Rev. E **58**, 1906 (1998).

APPENDIX C:

Robust Control for Convection Suppression in a Fluid Layer: The Effects of
Boundary Properties, Actuator Lag and Major Parameter Uncertainties

Robust control for convection suppression in a fluid layer: The effects of boundary properties, actuator lag, and major parameter uncertainties

A. C. Or and J. L. Speyer

Department of Mechanical and Aerospace Engineering, University of California, Los Angeles, California 90095-1597, USA

The robustness of control is a requirement to maintain a fluid layer at conductive equilibrium heated to a highly supercritical condition. Robustness determines how much uncertainties, or design parameter mismatches, can be tolerated. Both linear stability analysis and three-dimensional fully nonlinear simulations are used for the study of the linear quadratic Gaussian (LQG) controller. The parameter mismatches from the nominal conditions are introduced into the plant model, while the LQG compensator assumes nominal conditions. The mismatches arise from boundary properties, actuator lag, sensor level uncertainty, and wall thickness, as well as from the major parameters such as Prandtl number, Rayleigh number, wave number, and truncation number in the reduced-order model. The results suggest that the LQG compensator action can preserve closed-loop stability at over ten times the critical Rayleigh number, provided that the mismatches in the sensor level and wall thickness are small. Mismatches in the Prandtl number and wall material properties have little impact. Mismatches in Rayleigh number and wave number are relatively benign compared with the sensor and thickness parameters. Techniques for measuring the plant output temperature at multiple levels with sufficient accuracy may be an implementation challenge.

I. INTRODUCTION

Fluid flow control has become a rapidly growing area of research, that combines traditional knowledge of fluid dynamics and numerical computations and modern estimation and control theory. A particular well-known problem that has been pursued by investigators with interest in recent years is the convection suppression in a layer of fluid at supercritical condition (a simple two degree-of-freedom analogy is controlling an inverted pendulum about its vertical position).

The goal of analysis is to develop a robust compensator design for convection suppression using a modern control synthesis approach. The Boussinesq model of Rayleigh-Bénard convection has been investigated quite vigorously because the experimental configuration can be modeled and simulated with high fidelity. In Refs. [1,2] a purely proportional feedback control law is shown to produce encouraging results, even though the control law is well known for its limitations. Another limitation is the choice and placement of temperature sensors, Howle [1,3] measured the mean temperature, averaged over the fluid depth (by shadowgraph technique); Tang and Bau [2,4] measured the temperature only at a single level along the fluid depth. Neither has provided temperature measurements sufficient to characterize the disturbance mode shapes along the direction of the layer depth. The mixed findings, discrepancies between theoretical and experimental results reported by the authors, may very well be due to the lack of robustness of control, the simple feedback control law, as well as the crude sensor outputs and lack of observability.

Measuring disturbance temperatures at multiple levels improves the system observability significantly. In our model, knowledge of temperatures at three interior levels of the fluid layer is assumed. This is a significant assumption. For an actual laboratory implementation, the remote infrared (IR)

sensing technique is probably the only viable way to acquire such knowledge. Furthermore, for a complete horizontal coverage of the fluid layer, it will probably require a high-frequency scanning and sensing technique. This technique is available for many applications but is not investigated in this study.

To improve the robustness of control we have developed a linear quadratic Gaussian (LQG) control synthesis compensator [5]. The LQG design with loop transfer recovery (LTR) is well known and proven to give robust performance in many applications. The LQG-LTR compensator is applied to a three-dimensional, fully nonlinear model [6] developed based on a Boussinesq system of equations treated by a spectral, time-splitting technique (see Marcus [7]). The results show that the linear compensator is effective in damping out an initial state of finite-amplitude convection at a higher Ra than that reported in Refs. [1,4]. The linear compensator is modally distributed. Although the compensator built for each Fourier mode is linear, controlling all Fourier harmonic modes is nonlinear in the sense that all these modes are generated by the advective nonlinearities. Two further significant advances in the compensator design are reported in Ref. [8]. These are (i) the successful building of an order-reduced LQG compensator, and (ii) the developing of a gain schedule algorithm.

This paper aims at the robustness of the LQG compensator. To enhance the fidelity of the existing plant models (linear model for stability analysis and fully nonlinear and three-dimensional for simulations), we incorporate finite walls to replace the isothermal boundary condition. A finite-wall model is studied by Howle [9]. In the parameter region studied the closed-loop behavior has an interesting oscillatory mode. As for our LQG compensator model, both the idealized and finite-wall versions are used. To avoid confusion, we denote the compensator with idealized boundary condi-
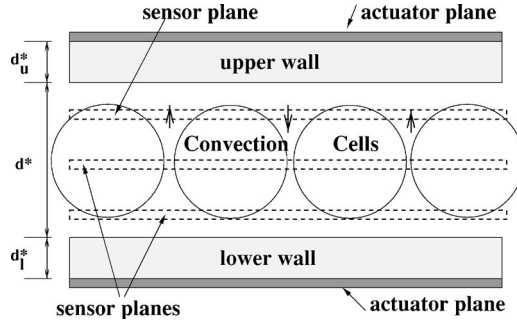
FIG. 1. The sensor and actuator location in the fluid layer.

tions [5] as C1 and the compensator with finite conductive walls as C3. Also, in addition to using one actuator plane at the bottom wall (referred as a single-plane actuator), an additional actuator plane at the upper wall (referred as a double-plane actuator) is used. For the evaluation of controller robustness, in our previous study [5], the plant, like the compensator, is set at the nominal parameters.

In Ref. [5], the Nyquist criterion provides the indicator for robustness. The Nyquist criterion gives the total margin. Moreover, no detailed investigation of the stability margin as a function of the wave number is provided. In this study, effects that impact robustness will be sorted out individually, as a function of wave number. The stability margins are obtained with respect to the Rayleigh number, actuator lag, sensor-plane depth uncertainty, wall thickness uncertainty, and single-plane versus double-plane actuators. Besides computing the stability limiting curves based on linear models, we also introduce a singular-value bound as a more conservative criterion for robustness, which is applicable to multi-input-multi-output (MIMO) plant systems. Besides the linear stability, we also investigate robustness using a fully nonlinear, three-dimensional (3D) simulation tool.

II. MATHEMATICAL FORMULATION

A. Plant model

In Fig. 1 we show a schematic of a section of an infinite layer of fluid, bounded by two finite-conductive walls with finite thickness. The fluid layer has thickness d^* [in this paper an asterisk denotes dimensional variables or compensator parameters (at nominal conditions)]. The outer surfaces of the lower and upper walls are prescribed at temperatures T_2^* and T_1^*, respectively. The upper and lower wall of thicknesses are d_u^* and d_ℓ^*. For nondimensional scalings we use the external temperature difference $\Delta T^* = T_2^* - T_1^*$ as the temperature scale and the fluid layer thickness d^* as the length scale. In addition, the fluid thermal diffusive time scale d^{*2}/κ^* is used for scaling time, where κ^* is the fluid's thermal diffusivity. The equilibrium conductive temperature modified by the presence of the finite walls is derived in the Appendix. In the nondimensional form, the fluid is governed by the Oberbeck-Boussinesq (OB) equations,

$$\text{Pr}^{-1}\partial_t \mathbf{v} = \text{Pr}^{-1}\mathbf{v} \times \boldsymbol{\omega} + \mathbf{k}\text{Ra}\theta - \boldsymbol{\nabla}\pi_e + \boldsymbol{\nabla}^2\mathbf{v}, \quad (1)$$

$$\partial_t \theta = -\mathbf{v} \cdot \boldsymbol{\nabla}\theta + w + \boldsymbol{\nabla}^2\theta, \quad (2)$$

$$\boldsymbol{\nabla} \cdot \mathbf{v} = 0, \quad (3)$$

where $\mathbf{v} = (u, v, w)$ is the velocity vector field, $\boldsymbol{\omega} = \boldsymbol{\nabla} \times \mathbf{v}$ is the vorticity, $\pi_e = \pi + \mathbf{v} \cdot \mathbf{v}/2$ is the effective pressure head, θ is the perturbation temperature with respect to the equilibrium conductive state. The z direction is directed upward and $\mathbf{k}$ is the unit vector.

The plant system has two external nondimensional parameters: the Rayleigh number and the Prandtl number. The Prandtl number is $\text{Pr} = \nu^*/\kappa^*$, where ν^* is the kinematic viscosity. The Rayleigh number is defined in terms of the outer-wall temperature difference and the fluid layer thickness, $\text{Ra} = \alpha^* g \Delta T^* (d^*)^3/\nu^*\kappa^*$, where α^* is the coefficient of thermal expansion. All the material properties are assumed constant. Note that Ra here is defined based on the outer wall-to-wall temperatures ΔT^* but fluid thickness d^*. The effective Ra_f should be defined based on the fluid boundary temperatures. In the Appendix, Ra_f is derived from Ra, by replacing d^* with d^*h, where h is a nondimensional factor. Equation (3) is the continuity equation for incompressible flow.

In addition to the OB equations describing the fluid layer, the lower and upper wall walls are governed only by the heat-transfer equations,

$$\partial_t \theta_\ell = \kappa_\ell \boldsymbol{\nabla}^2 \theta_\ell, \quad (4)$$

and

$$\partial_t \theta_u = \kappa_u \boldsymbol{\nabla}^2 \theta_u, \quad (5)$$

where $\kappa_\ell = \kappa_\ell^*/\kappa^*$ and $\kappa_u = \kappa_u^*/\kappa^*$.

The kinematic boundary conditions applied to the velocity field in the fluid layer, which are defined as the nonpermeable and nonslip conditions,

$$\mathbf{v}(x, y, 0, t) = \mathbf{0}, \quad \mathbf{v}(x, y, 1, t) = \mathbf{0}. \quad (6)$$

The fluid-wall interfacial thermal boundary conditions are dynamic, not prescribed. They are matched conditions of temperatures and heat flux,

$$\theta(x, y, 0, t) = \theta_\ell(x, y, 0, t),$$

$$\partial_z \theta(x, y, z, t)|_{z=0} = k_\ell \partial_z \theta_\ell(x, y, z, t)|_{z=0} \quad (7)$$

and

$$\theta(x, y, 1, t) = \theta_u(x, y, 1, t),$$

$$\partial_z \theta(x, y, z, t)|_{z=1} = k_u \partial_z \theta_u(x, y, z, t)|_{z=1}. \quad (8)$$

The parameters k_ℓ and k_u are the thermal conductivity ratios of the upper and lower wall materials defined in the Appendix, respectively.

The thermal actuators correspond to the prescribed outer wall thermal boundary conditions,

$$\theta_\ell(x, y, -d_\ell, t) = u_\ell(x, y, t), \quad (9)$$

where $u_\ell(x, y, t)$ is the temperature control input imposed at lower wall, and

$$\theta_u(x,y,1+d_u,t) = u_u(x,y,t), \qquad (10)$$

where $u_u(x,y,t)$ is the temperature control input imposed at upper wall in case of two actuator planes. The control inputs to the plant u_ℓ and u_u are functions of the sensor outputs from the plant. Like in Ref. [5], we consider three sensor planes, located at $z=z_{sk}$, $k=1,2,3$. The sensor planes measure temperatures

$$z_{sk}(x,y,t) = \theta(x,y,z_{sk},t), \quad k=1,2,3. \qquad (11)$$

The spectral decomposition of the three-dimensional velocity and temperature field variables and the fractional step, time-splitting method for integrating the fully nonlinear OB system of equations are described in detail in Ref. [6]. Details are provided in the references therein, in particular, by Marcus [7]. Here, only the addition of the conductive walls into the existing numerical scheme, described by Eqs. (4) and (5), will be mentioned with no repetitions.

Unfortunately, a direct incorporation of Eqs. (4) and (5) using the existing fractional-step approach [6] is numerically unstable. So, the three heat equations have to be solved simultaneously. Referring to Ref. [6], we add to the physical dependent variables two thermal fields (θ_ℓ,θ_u), besides the existing fields (u,v,w,p,θ). All the fields have independent variables (x,y,z,t), where each field has the same (x,y) coordinate ranges, but θ_ℓ, θ, and θ_u have different z coordinate ranges. We use three column vectors to represent the corresponding Fourier-Chebyshev coefficients $(\boldsymbol{\theta}_\ell,\boldsymbol{\theta},\boldsymbol{\theta}_u)$ corresponding to the physical field variables $(\theta_\ell,\theta,\theta_u)$.

The finite wall temperature distribution has a simple closed-form solution if the diffusive term in the diffusive equations dominates and the time derivative term is negligible [10]. In general, a numerical solution is computed. At the nth time step (not fractional step), the wall temperatures are expressed as

$$\boldsymbol{\theta}_\ell^{(n+1)} = \mathbf{b}_1(\boldsymbol{\alpha}^T\boldsymbol{\theta}^{(n)}) + \mathbf{b}_2 u_\ell^{(n)}, \quad \boldsymbol{\alpha} = [1,-1,1,-1,\dots]^T,$$

$$\boldsymbol{\theta}_u^{(n+1)} = \mathbf{b}_3(\boldsymbol{\beta}^T\boldsymbol{\theta}^{(n)}) + \mathbf{b}_4 u_u^{(n)}, \quad \boldsymbol{\beta} = [1,1,1,1,\dots]^T, \quad (12)$$

where $\mathbf{b}_j$ $(j=1,4)$ are obtained by inverting the two matrix equations for the wall heat equations. The implicit Euler and tau method are used here. For the lower wall heat equation, its lower boundary condition is the lower wall control and its upper boundary condition can be either the interfacial temperature matching condition or the interfacial heat flux matching condition. Similar conditions for the boundary conditions of the upper wall heat equation are developed, although we choose the interfacial temperature matching conditions as the boundary conditions for solving the wall heat equations. The two scalar controls, u_ℓ and u_u are either functions of (x,y,t) (in physical space) or (k_x,k_y,t) (in Fourier space). In this way, the wall temperatures are explicitly solved in terms of the two control parameters and the fluid layer temperature distribution.

We can now replace the idealized lower and upper boundary conditions [i.e., $\theta(x,y,0,t)=u_\ell(x,y,t)$ and $\theta(x,y,1,t)=u_u(x,y,t)$] previously used [6] by the following conditions, respectively:

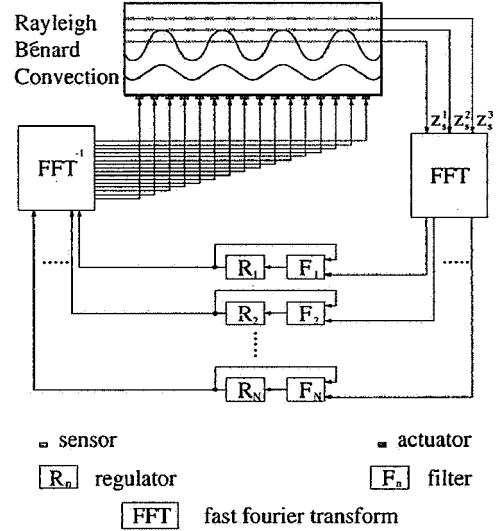FIG. 2. The LQG control loop diagram.

$$\left(\boldsymbol{\alpha}^T\mathbf{D} - \frac{k_\ell}{d_\ell}(\boldsymbol{\beta}^T\mathbf{D}\mathbf{b}_1)\boldsymbol{\alpha}\right)\boldsymbol{\theta}^{(n+1)} = \frac{k_\ell}{d_\ell}(\boldsymbol{\beta}^T\mathbf{D}\mathbf{b}_2)u_\ell^{(n)},$$

$$\left(\boldsymbol{\beta}^T\mathbf{D} - \frac{k_\ell}{d_\ell}(\boldsymbol{\alpha}^T\mathbf{D}\mathbf{b}_3)\boldsymbol{\beta}\right)\boldsymbol{\theta}^{(n+1)} = \frac{k_\ell}{d_\ell}(\boldsymbol{\alpha}^T\mathbf{D}\mathbf{b}_4)u_u^{(n)}, \quad (13)$$

where $\mathbf{D}$ is the first derivative matrix defined for $z=0,1$ for the Chebyshev coefficients $(\theta\to\partial_z\theta$ corresponds to $\boldsymbol{\theta}\to\mathbf{D}\boldsymbol{\theta})$. If the interfacial temperature matching conditions are used for the wall temperatures, then the interfacial heat flux matching conditions have to be used for the fluid, and vice versa. It can be shown that, as $k_\ell/d_\ell\to\infty$, the lower wall boundary condition approaches the idealized boundary condition used in our previous studies. A similar condition holds for the upper wall boundary condition. An actuator lag for the controls is incorporated as an additional plant state.

B. Modally distributed LQG compensator

The LQG compensator design is described in detail in Ref. [5]. We will not repeat the details here. In brief, each compensator (denoted as a transfer function matrix $\mathbf{K}_{mn}$ below, $m=1,2,\dots,N_x$, $n=1,2,\dots,N_y$, see Fig. 2), is of the linear quadratic Gaussian and loop transfer recovery (LQG-LTR) type. The LTR approximation provides almost the full-state feedback performance of $\pm 60°$ phase margin and -6 dB to ∞ in lower and upper gain margins, by allowing the observer weighting parameter $\beta\to\infty$ [11]. As in our previous design [6], we use $\beta=10^3$. We use the regulator weighting parameter $\gamma=0.1$. Note that $\gamma\to 0$ corresponds to unlimited control authority. In addition to the compensator parameters γ and β, the compensator has system model that involves the major physical parameters of the problem; the Rayleigh number as Ra^* and the wave number as (mk_x^*,nk_y^*) (the asterisk denotes nominal values). When the nonlinear plant yields a solution described by a 2D wave number array (mk_x,nk_y) for $m=1,2,\dots,N_x$, and $n=1,2,\dots,N_y$, then the compensator consists of $N=N_xN_y$ single-wave-number sub-
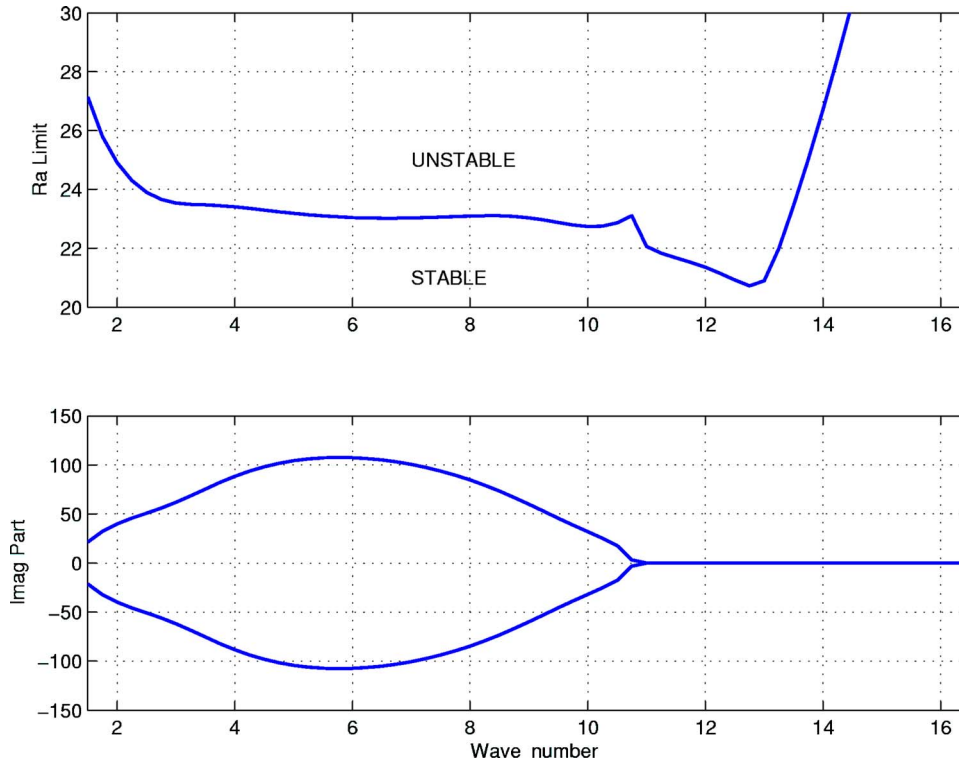
FIG. 3. (Color online) Stability margin in Ra vs k for Pr=7.0 (upper panel) and corresponding imaginary eigenvalue (lower panel).

compensators. A kth subcompensator consists of a Kalman filter F_k and a optimal regulator R_k $(k=1,2,\ldots,N)$. The three levels of temperatures in Fig. 2 are denoted by Z_1, Z_2, and Z_3. The output from the kth compensator is either one or two scalar controls, depending on one or two actuator planes used. The corresponding plant parameters (without asterisk, with uncertainties) can differ from the compensator parameters (with asterisk, at nominal conditions). Figure 2 presents a block diagram showing the Fourier-decomposed nonlinear plant. All inputs and outputs are Fourier-Chebyshev coefficients. Each Fourier mode disturbance corresponding to wave numbers (mk_x,nk_y) is controlled by a LQG compensator $\mathbf{K}_{mn}$ designed at the nominal wave numbers (mk_x^*,nk_y^*). The greater the difference between the compensator and plant parameters while preserving closed-loop stability, the more robust the compensator, i.e, the greater the stability margins. We denote the compensator corresponding to idealized thermal boundary condition as C1, and the one incorporating finite walls as C3. The reduced-order compensator [8] is used here. Since our focus is on robustness, we will not deal with the transient conductive state nor will the gain-scheduling algorithm be used.

III. RESULTS

A. Linear stability using a single-plane actuator

In the linear stability study, a linearized plant dynamical model is used. We assume the material properties of the upper and lower walls to be the same, corresponding to aluminum at room temperature. The walls have thickness 1/10 of the fluid depth. For the working fluid using water we have Pr=7.0, $K_l=K_u=400$, and $\kappa_l=\kappa_u=670$. Using air we have Pr=0.7, $K_l=K_u=8800$, and $\kappa_l=\kappa_u=4.2$ instead.

1. Major parameter uncertainties

Our nominal model consists of one actuator, located at outer surface of the lower wall, at $z=-d_l$ and three sensor planes, located at $z_{s1}=0.2$, $z_{s2}=0.5$, and $z_{s3}=0.8$. These are optimal sensor locations according to our previous analysis [5]. The nominal $\mathrm{Ra}^*=20\,\mathrm{Ra}_c$, where $\mathrm{Ra}_c\approx1707.762$ is the critical Rayleigh number. The LQG compensator is designed at the nominal values (denoted by an asterisk). In the nonlinear simulations [6–8] the compensator consists of an array of single-k controllers. The nominal wave number k^* is an array evenly spaced wave numbers covering the entire unstable band at Ra^*. In the linear stability analysis, the nominal wave number k^* is a prescribed parameter that can be varied across the unstable band. Here the compensator is assumed to be designed at (k^*,Ra^*). At nominal condition, the plant model has $k=k^*$ and $\mathrm{Ra}=\mathrm{Ra}^*$. For robustness investigation, we vary k and Ra from their nominal values.

The eigenvalue analysis indicates that the closed-loop system using the steady-state LQG compensator is always stable at the nominal condition, i.e., at $k=k^*$ and $\mathrm{Ra}=\mathrm{Ra}^*$ even when Ra^* is as large as $100\mathrm{Ra}_c$. However, at high Ra exceeding, say, $20\mathrm{Ra}_c$, the least stable eigenvalue becomes sensitive to small changes in the prescribed parameter. This is an indication of weakening of robustness at large Ra.

In the following, we vary the plant parameter Ra from the nominal value $\mathrm{Ra}^*=20\mathrm{Ra}_c$ to see how far the system can tolerate the change before becoming unstable. The result presents the stability margin $\Delta\mathrm{Ra}=\mathrm{Ra}-\mathrm{Ra}^*$ in terms of the wave number k^*. In doing so we assume that the plant wave number k is unchanged from the nominal value k^*. In Figs. 3 and 4, we show the results Ra vs k for the case at Pr=7.0 and Pr=0.7, respectively. The margin $\Delta\mathrm{Ra}$ is the range above 20. For the two values of Pr, the results appear very similar. The
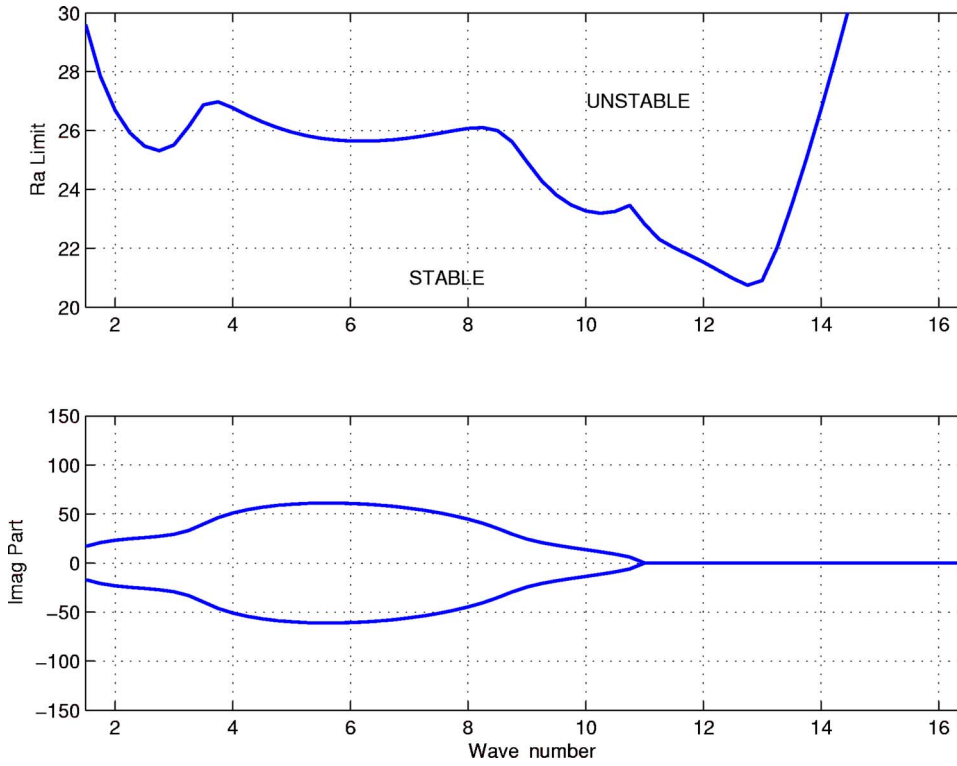
FIG. 4. (Color online) Stability margin in Ra vs k for Pr=0.7 (upper panel) and corresponding imaginary eigenvalue (lower panel).

margin in Ra (upper panels) dips to a minimum near $k=13$. Although the minimal margin occurs at approximately four times the critical wave number $k_c \approx 3.117$, in the nonlinear simulations presented later, we see no sign that short-wave modes are being excited. In fact, nonlinearity is stabilizing by cascading disturbances to shorter and shorter harmonic modes that promote diffusions. Beyond $k=13$, the modal diffusive terms become very large and stabilizing; the Ra margin is expected to increase unboundedly. The pair of imaginary eigenvalues with zero real part is shown in the lower panels. The result shows that, for positive plant uncertainty in Ra (i.e., $\text{Ra} > \text{Ra}^*$), the closed-loop behavior first becomes unstable to an oscillatory mode at lower wave number and to a monotonic mode at higher wave number. For negative plant uncertainty in Ra (i.e., $\text{Ra} < \text{Ra}^*$), the closed-loop behavior is always stable.

We turn to the wave number margins. Here we assume there is no uncertainty in Ra, i.e., $\text{Ra} = \text{Ra}^* = 20\text{Ra}_c$. We vary the nominal wave number k^* and at each value of k^* we determine the Δk margins, $\Delta k = k - k^*$, where there are two values of Δk, the upper and lower Δk stability limit. Again, we consider the cases of Pr=7.0 (Fig. 5) and Pr=0.7 (Fig. 6). Again, we see that the behavior for both cases are very similar. In both cases, the upper Δk margin (upper curve) increases steeply beyond $k^*=8$. The lower k margin (lower curve) behaves in a rather complicated fashion. The margin diverges between $k^*=4.0$ and 5.0 but between $k^*=5.0$ and the Δk minimum near $k^*=13$, the margin is quite flat. Then, beyond $k^*=13$, the lower Δk margin increases linearly. It appears that the stability margin is weakest near $k^*=13$, which means that the closed-loop system is least robust with respect to, or most vulnerable to, unstable mode onset for a spatial length scale corresponding to $k^*=13$, or a wavelength $\lambda^* = 2\pi/k^*$, approximately 1/2 of the layer depth.

We emphasize that the three-level sensor configuration is important for robustness. Decreasing the number of sensor planes or moving the outer sensor planes towards the wall will erode the state observability. As a result, closed-loop stability is only achievable at much lower Ra^*.

2. Actuator lag

A potential destabilizing effect arises from the actuator lag. Both finite conductivity and electronic processing in the thermal actuator contribute to the actuator lag. A first-order lag effect is incorporated in the linearized plant model and later in the nonlinear plant, described by the transfer function (TF) $G_d = \omega_d/(s + \omega_d)$ where s is the Laplace-transformed value. This TF has to be modeled in between the compensator output u_o and the plant input u_i. Because of the lag, we have

$$\dot{u}_i + \omega_d u_i = \omega_d u_o. \tag{14}$$

For large ω_d, or small lag time constant $\tau_d = 2\pi/\omega_d$, the effect is small, i.e., $u_o \approx u_i$. But for large τ_d, the lag can be destabilizing. To model the actuator lag, we write the linear plant state-space equation as $\dot{\mathbf{x}} = \mathbf{A}\mathbf{x} + \mathbf{B}u_i$, where u_i is given in Eq. (14). The compensator output u_o can be used as the input to the plant model, modified as

$$\begin{bmatrix} \dot{\mathbf{x}} \\ \dot{u}_i \end{bmatrix} = \begin{bmatrix} \mathbf{A} & \mathbf{B} \\ \mathbf{0} & -\omega_d \end{bmatrix} \begin{bmatrix} \mathbf{x} \\ u_i \end{bmatrix} + \begin{bmatrix} \mathbf{0} \\ \omega_d \end{bmatrix} u_o,$$

$$\mathbf{y} = \begin{bmatrix} \mathbf{C} & 0 \end{bmatrix} \begin{bmatrix} \mathbf{x} \\ u_i \end{bmatrix}. \tag{15}$$
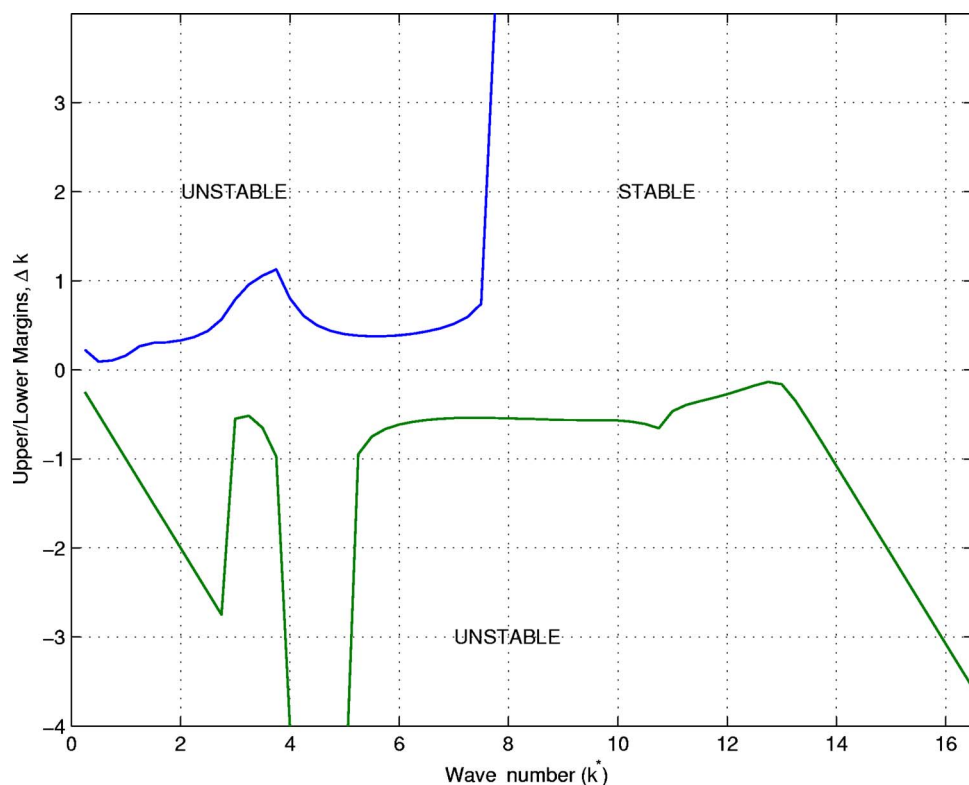
FIG. 5. (Color online) Margins Δk vs k^* for Ra=20Ra$_c$, Pr=7.0.

In Fig. 7, we show the destabilizing effect of the actuator lag by plotting the real part of the least stable eigenvalue (growth rate) versus wave number. In this case, both plant and compensator parameters are set to the same condition, with $k=k^*$, Ra=Ra*=20Ra$_c$. The left panel shows the case for Pr=7.0 and the right panel shows the case for Pr=0.7. In both cases, the least-stable eigenvalue (real) is shown as a function of the wave number (k) for three lag time constants, τ_d=0.001, 0.003, and 0.005. These are in nondimensional time unit. In the wave-number band between $k=3$ and $k=8$ for the case of Pr=7.0, a sufficiently large lag time-constant causes instability. For the case Pr=0.7, however, the lag has
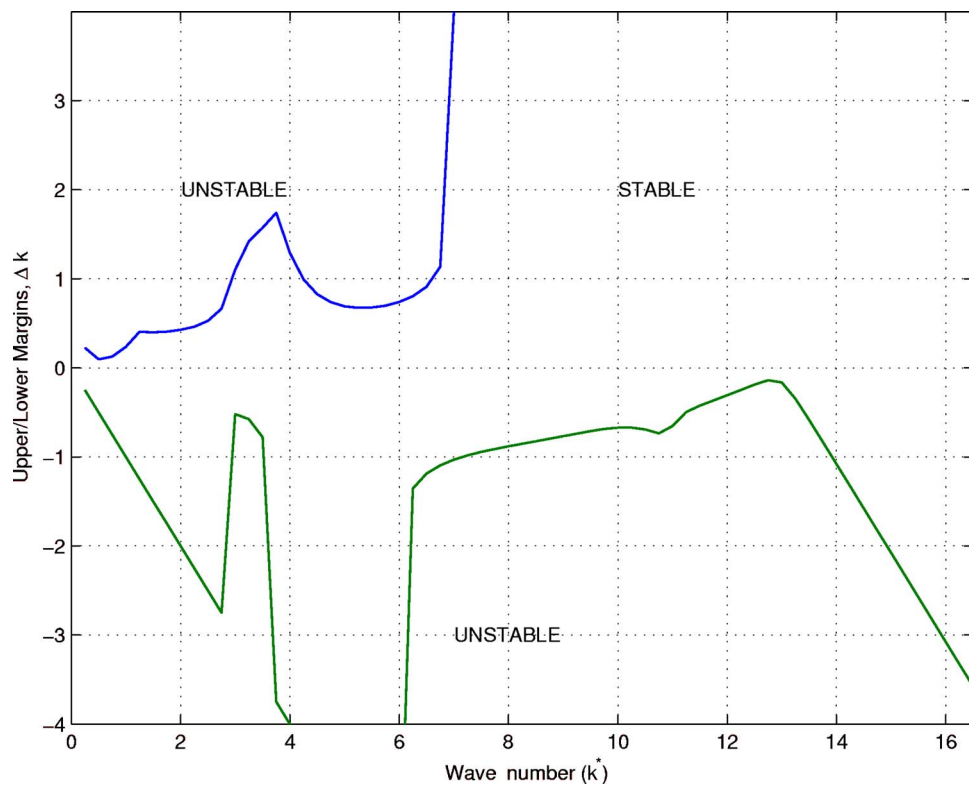
FIG. 6. (Color online) Margins Δk vs k^* for Ra=20Ra$_c$, Pr=0.7.
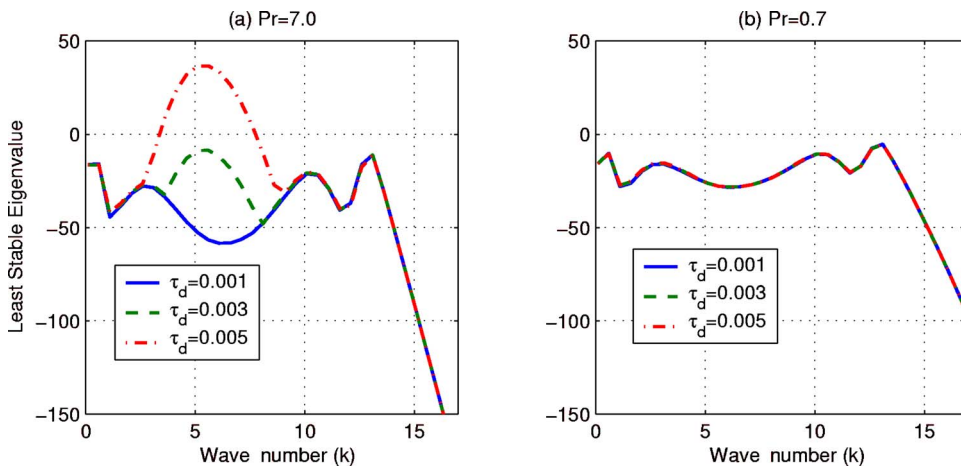
FIG. 7. (Color online) Least stable eigenvalue vs k with actuator lag.

no destabilizing effect. For the case Pr=0.7, τ_d=0.003 almost drives the Fourier mode at k=5 unstable. For the case Pr=0.7, the actuator lag is more destabilizing for higher wave number. The eigenvalue peaks near k=13.

The nondimensional time scale is d^2/κ. For water and layer thickness d=0.5 cm, one nondimensional time unit =176 s at standard temperature pressure (STP). For air κ is about 145 times that of water. In order to get the same nondimensional time scale d for air has to be 12 times that of d for water. For the nondimensional time scale, if the layer thickness is 0.5 cm, say for water at STP, a physical lag τ_d =0.001 corresponds to 0.18 s, roughly; and that for air is only 0.001 s. One can always stretch the physical lag time for the same value of τ_d, by increasing the layer depth of air. In order to maintain the same Ra for air (Ra is proportional to d^3/κ for a given temperature difference), however, this implies decreasing the temperature difference for air.

3. Sensor plane depth uncertainty

The sensor-plane depth uncertainty turns out to be a difficult problem. The nominal sensor plane depths are z_1^*=0.2, z_2^*=0.5, and z_3^*=0.8 (scaled by the fluid layer thickness). Consider the compensator model to have these nominal values but the plant model has corresponding plane depths of $z_1=z_1^*+\Delta z_1$, $z_2=z_2^*+\Delta z_2$, and $z_3=z_3^*+\Delta z_3$ where the perturbations are due to uncertainties. We assume each of Δz_i is a zero-mean Gaussian number with standard deviation 0.01. Consider the case Pr=7.0, Ra=Ra*=2000, $k=k^*$=3.5. We use the C3 compensator for the three-layer plant model. Figure 8 shows the results for 5000 Monte Carlo runs. For each realization of error $(\Delta z_1, \Delta z_2, \Delta z_3)$, the closed-loop, least stable eigenvalue is computed. If the real part is less than or equal to zero, a dot is shown in the plot. The ensemble shows where the stable region lies on the 3D error space. Panels
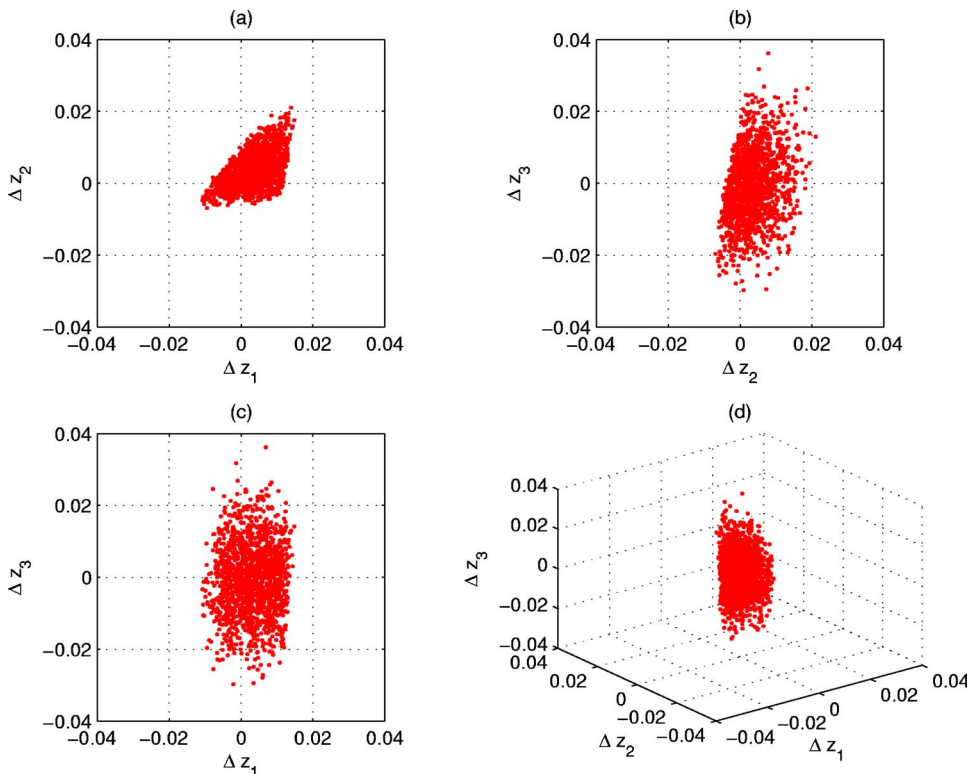

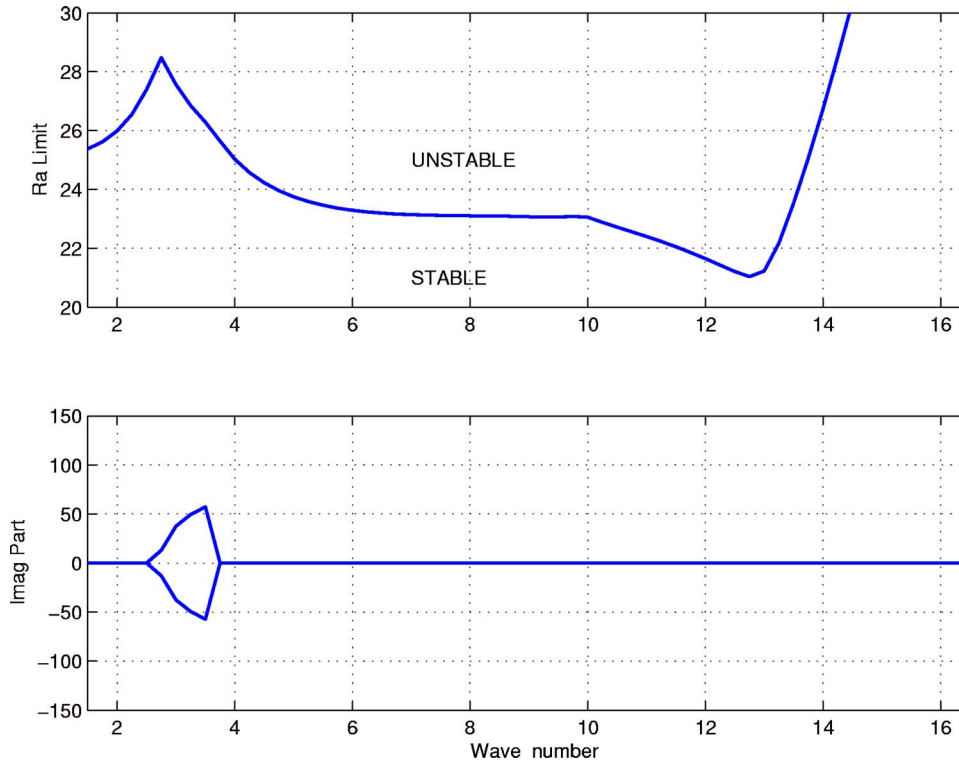FIG. 8. (Color online) Stable region in the 3D error space from 5000 Monte Carlo runs.

FIG. 9. (Color online) Stability margin in Ra vs k for Pr=7.0 (upper panel), and corresponding imaginary eigenvalue (lower panel).

(a)–(c) are projection of the points (stable) onto the Δz_1 vs Δz_2 plane, Δz_2 vs Δz_3 plane, and Δz_1 vs Δz_3 plane, respectively. The last panel shows the 3D plot of the points. The unstable points are not shown. The figures use a uniform scale per axis from −0.04 to 0.04. The results indicate that (i) the stable region in the 3D error space is quite small; (ii) Δz_3 appears to be the least significant error among the three, relatively speaking. It means the sensor plane farthest from the actuator plane can tolerate largest uncertainty; (iii) both Δz_1 and Δz_2 are important. However, the shape of the stable region is not symmetric with respect to the sign of error. It appears less destabilizing if the first and second sensor planes are moving away from the actuator, more destabilizing if both are moving towards the actuator. It is worse if one is moving away but the other is moving towards the actuator. The sensor-plane depth errors can be a significant challenge in the laboratory implementation.

B. Linear stability using two actuator planes

It is of interest to see if there will be improvement in the robustness by the addition of an extra actuator plane on the outer face of the upper wall. This addition makes the plant a three-input-two-output system. We choose to show the case Pr=7.0 only. In Fig. 9, we show the Ra margin in k as in the nominal case. The margin curves are very similar to the ones before. Only a very slight improvement in margins is evident. The improvement is not significant. Compared the second panel between Figs. 3 and 9, the k band for imaginary part of the least-stable eigenvalue becomes significantly smaller. In Fig. 10, we show the upper and lower k margins vs k. Again, the improvement with an additional actuator is small.

1. Singular-value bounds

Doyle and Stein [11] develop an approach to use the singular values bounds for relative stability measure in finite-dimensional, linear-time-invariant (FDLT) systems. The conditions give bounds that guarantee stability but these are not necessarily tight bounds, therefore, more conservative. To illustrate the idea, it is more convenient to use the transfer function (TF) notation. The TF between input and output of the state-space system $(\mathbf{A},\mathbf{B},\mathbf{C},\mathbf{D})$, corresponding to the standard dynamical and output equations $\dot{\mathbf{x}}=\mathbf{A}\mathbf{x}+\mathbf{B}\mathbf{u}$ and $\mathbf{y}=\mathbf{C}\mathbf{x}+\mathbf{D}\mathbf{u}$ (after Laplace transform) is $\mathbf{y}(s)=\mathbf{G}(s)\mathbf{u}(s)$, where $\mathbf{G}(s)=\mathbf{C}(s\mathbf{I}-\mathbf{A})^{-1}\mathbf{B}+\mathbf{D}$. Here, we use $\mathbf{G}(s)$ to denote the plant TF. In the following, both plant and compensator TFs correspond to a single-wave-number model. There are two common ways to model uncertainties. One is by additive perturbation to the nominal $\mathbf{G}(s)$, $\mathbf{G}'=\mathbf{G}+\Delta\mathbf{G}$. The other is by multiplicative perturbation to the nominal $\mathbf{G}(s)$, $\mathbf{G}'=(\mathbf{I}+\mathbf{L})\mathbf{G}$, where $\mathbf{L}$ is a multiplicative error model derived based on $\mathbf{G}'$ and $\mathbf{G}$. Here, the latter way is adopted. To keep the uncertainties within bounds, we require $\overline{\sigma}(\mathbf{L})<\ell_m(\omega)$ for some prescribed function of frequency, $\ell_m(\omega)$. Here $\overline{\sigma}$ and $\underline{\sigma}$ denote the upper and lower bound singular values, respectively. The LQG compensator, denoted by $\mathbf{K}(s)$ is defined by state space system $((\mathbf{A}^*-\mathbf{K}_f\mathbf{C}^*-\mathbf{B}^*\mathbf{K}_c),\mathbf{K}_f,-\mathbf{K}_c\mathbf{D}^*)$, where $\mathbf{K}_f$ and $\mathbf{K}_c$ are the filter and regulator gains, respectively. Otherwise, the matrices are identical to those of the linearized plant.

There are two ways consider breaking the loop of a compensated plant. One is by breaking the loop at the plant output [see Fig. 11(a)]. This case gives a compensated plant TF equal to $\mathbf{GK}(s)$ and the other is by breaking the loop at the plant input [see Fig. 11(b)]. In both figures, the dashed line in

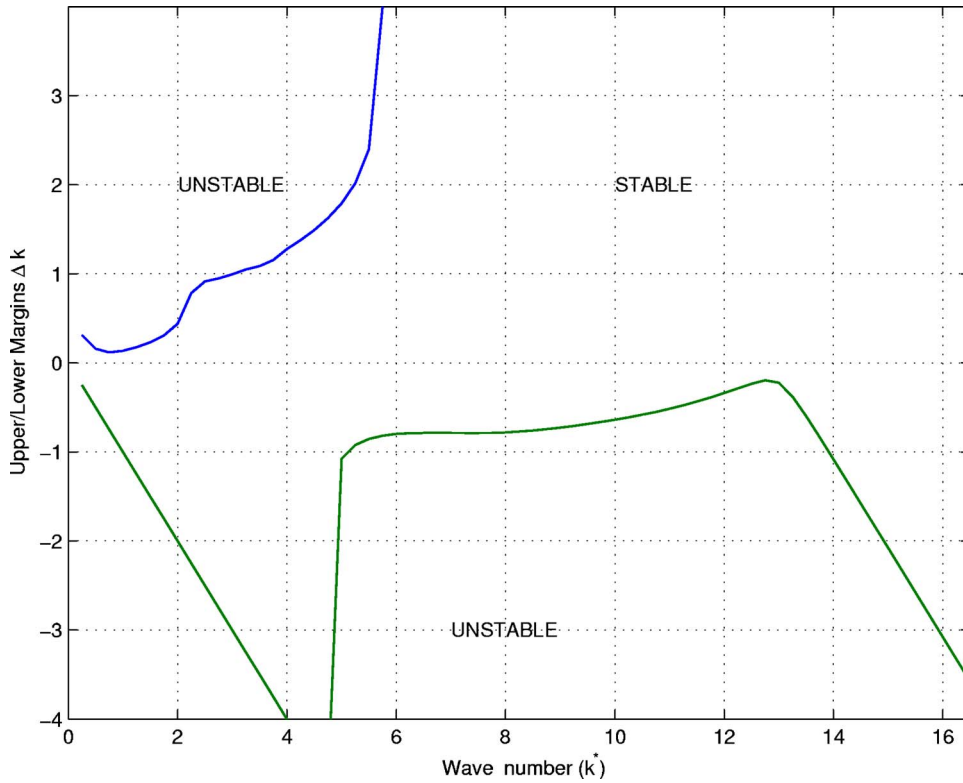FIG. 10. (Color online) Margins Δk vs k^* for Ra$=20$Ra$_c$, Pr $=7.0$.

the loop denote the broken loop. This case gives a compensator plant TF of $\mathbf{KG}(s)$ (note that the matrix columns correspond to the inputs and matrix rows correspond to the outputs). In Ref. [5], we considered a plant with one actuator plane (one input) and three sensor planes (three outputs). Therefore the dimensions of $\mathbf{G}(s)$ is 3×1. The compensator takes the three plant outputs as measurements to produce one control therefore the dimension of $\mathbf{K}(s)$ is 1×3. The advantage by breaking the loop at the plant input is that we obtain a single-input-single-output (SISO) $\mathbf{GK}(s)$. Therefore, as demonstrated in Ref. [5], the relative stability can be effectively analyzed using gain and phase margins, based on the classical Nyquist criterion.

Here, the Doyle and Stein condition provides an independent means to assess the stability margins, apart from the parameter margin curves from the direct closed-loop computation. We consider two actuator planes and three sensor planes. The Nyquist criterion can no longer be applied. Consider breaking the loop at the plant output (the argument is

(a) Breaking the Loop at Plant Output. $TF = GK$

(b) Breaking the Loop at Plant Input. $TF = KG$

FIG. 11. Block diagram showing breaking the compensated plant loop.

equally valid for breaking the loop at the plant input. In the present case, however, the plant has two plant inputs versus three outputs, we caution that the 3×3 matrix $\mathbf{GK}$ is rank deficient by 1). Doyle and Stein [11] noticed that to guarantee stability in the presence of uncertainties, $\mathbf{G'K}(s)$ has to preserve the system dimensions of $\mathbf{GK}(s)$. If the compensated plant has equal inputs and outputs, then the generalized Nyquist criterion on the determinant is that the number of encirclement of $\det(\mathbf{I+G'K})$ remains unchanged from $\det(\mathbf{I+GK})$. Preserving the system dimensions means that the lower bound of the singular value of $\mathbf{I+G'K}$ is positive definite. That is,

$$0 < \underline{\sigma}[\mathbf{I} + (\mathbf{I+L})\mathbf{GK}]. \qquad (16)$$

Since $(\mathbf{I+GK})$ is full rank, we pull it out as the common factor. Then, we require

$$0 < \underline{\sigma}[\mathbf{I} + \mathbf{LGK}(\mathbf{I+GK})^{-1}] \qquad (17)$$

for all ω and $\mathbf{L}$, or

$$\overline{\sigma}[\mathbf{GK}(\mathbf{I+GK})^{-1}] < 1/\ell_m. \qquad (18)$$

Using the matrix identity

$$\mathbf{GK}(\mathbf{I} + \mathbf{GK})^{-1} \equiv [\mathbf{I} + (\mathbf{GK})^{-1}]^{-1} \qquad (19)$$

the stability condition according to Ref. [11] is

$$\overline{\sigma}[\mathbf{L}(\omega)] < \underline{\sigma}[\mathbf{I} + (\mathbf{GK})^{-1}], \qquad (20)$$

where the right-hand term is referred to as the matrix return difference of the loop and $\ell_m(\omega)$ represents the singular-value bound of the error model $\overline{\sigma}(\mathbf{L}(\omega))$. Note that $\mathbf{GK}$ commutes with $(\mathbf{I+GK})^{-1}$. In the following, we apply the Doyle-Stein's stability condition to investigate two separate
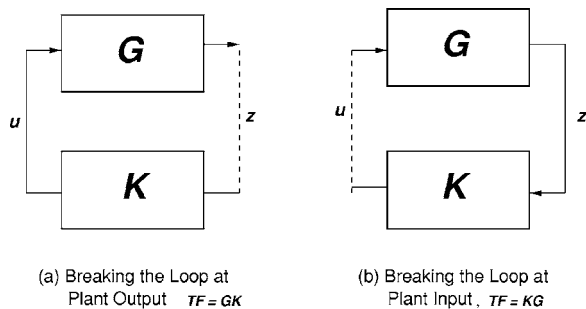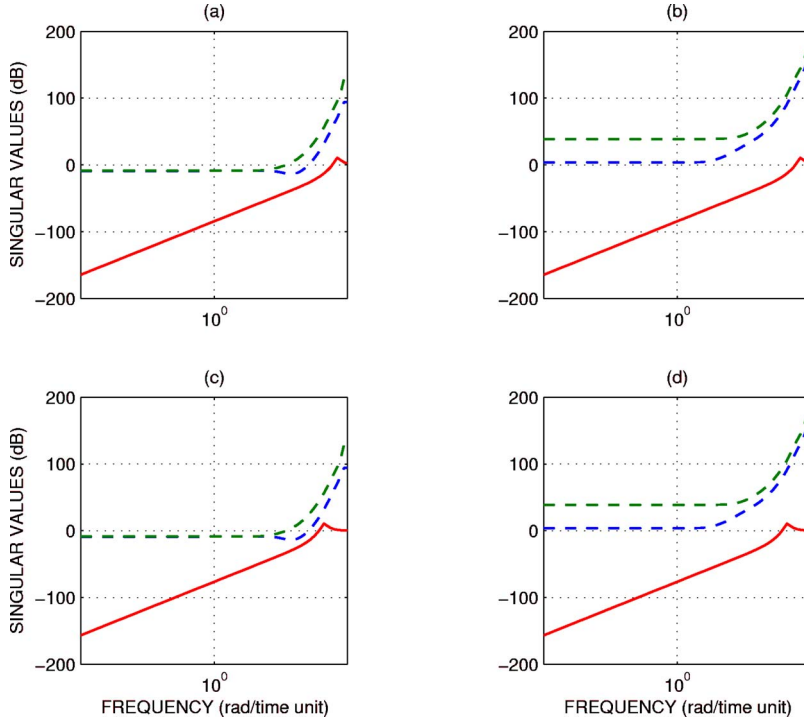
FIG. 12. (Color online) Singular-value bounds with the actuator error model.

problems. One is the actuator lag. The other is the finite wall thermal properties. The actuator is based on a second-order lag model according to Ref. [12]. Let L (for this case a scalar) be given by

$$\bar{\sigma}(L(\omega)) = \left| \frac{s^2 + 2\xi\omega_a s}{s^2 + 2\xi\omega_a s + \omega_a^2} \right| \, s = j\omega. \qquad (21)$$

A damping factor $\xi=0.15$ is used but ξ is not a sensitive parameter. Decreasing ξ to 0.05 gives roughly the same results. In Figs. 12(a) and 12(b), we show the case $\omega_a=5000$ and in Figs. 12(c) and 12(d), we show $\omega_a=2000$. These are nondimensional frequencies. The corresponding physical frequencies are typically two orders of magnitude lower. The left panel corresponds to $k=6.5$ and the right panel to $k=13.0$. The higher wave-number system appears more robust with respect to the actuator lag than the lower wave number. In each panel the two dashed curves correspond to the lower-bound singular values [see the right-hand side of inequality (20)]. The solid curve shows $\bar{\sigma}(L)$. The stability margin corresponds to the gap between the lower dashed curve and the solid curve. The larger the gap, the greater the margin. The result appears fairly consistent with those of Fig. 7. The upper-bound singular value of the actuator lag is shown in the lowest curve in each panel of the figure. Now, the lag time constant is $\tau_a=2\pi/\omega_a$. The smaller ω_a the greater the lag and the more destabilizing the lag effect becomes. The closed-loop system remains stable. The physical implication is this. For water as fluid, an actuator lag time constant of 0.5 s will not trigger instability. For air at STP, this time constant is shortened by a factor of roughly 150 times. It appears that if the physical dimensions are unchanged, controlling convection in air requires a much higher-bandwidth controller than in water. Next, we address the problem of uncertainties of the finite wall thermal properties. Here, we

construct a plant error model, denoted by $\Delta\mathbf{A}$ and $\Delta\mathbf{B}$ (where $\mathbf{C}$ and $\mathbf{D}$ are not affected) by the following. Let $\Delta\kappa_u=\Delta\kappa_\ell = \Delta\kappa$ and $\Delta K_u=\Delta K_\ell=\Delta K$. We compute the derivatives $\partial\mathbf{A}/\partial\kappa$, $\partial\mathbf{B}/\partial\kappa$, $\partial\mathbf{A}/\partial K$, and $\partial\mathbf{B}/\partial K$. So

$$\Delta\mathbf{A} = \frac{\partial\mathbf{A}}{\partial\kappa}\Delta\kappa + \frac{\partial\mathbf{A}}{\partial K}\Delta K,$$

$$\Delta\mathbf{B} = \frac{\partial\mathbf{B}}{\partial\kappa}\Delta\kappa + \frac{\partial\mathbf{B}}{\partial K}\Delta K. \qquad (22)$$

Note that the error model affects only the plant and the compensator remains at nominal parameters. From the error model, it is somewhat tedious, but quite straight forward to generate the TF version of the error $\mathbf{L}$ by keeping the first-order error terms (the derivation will not be produced here). Figures 13(a) and 13(b) shows the singular-value bounds for the same wave numbers $k=6.5$ and 13.0, respectively. In this case, we let $\Delta\kappa$ and ΔK to be 25% of the nominal values. The dashed curves are the same as in Fig. 12. The pair of lower solid curves represent the two singular values of $\mathbf{L}(\omega)$. The solid and dashed curves very barely intersect for the $k=6.5$ case near $\omega \approx 700$. It appears that stability is preserved in the presence of 25% uncertainties in the wall thermal properties (both diffusivity and conductivity), about the nominal values.

C. 3D nonlinear closed-loop simulations

1. Model setup and assumptions

The compensator is linear, set at the nominal parameters and the plant model is 3D, nonlinear with uncertainties about the nominal parameters. The closed-loop system in the presence of uncertainties is investigated by examining the
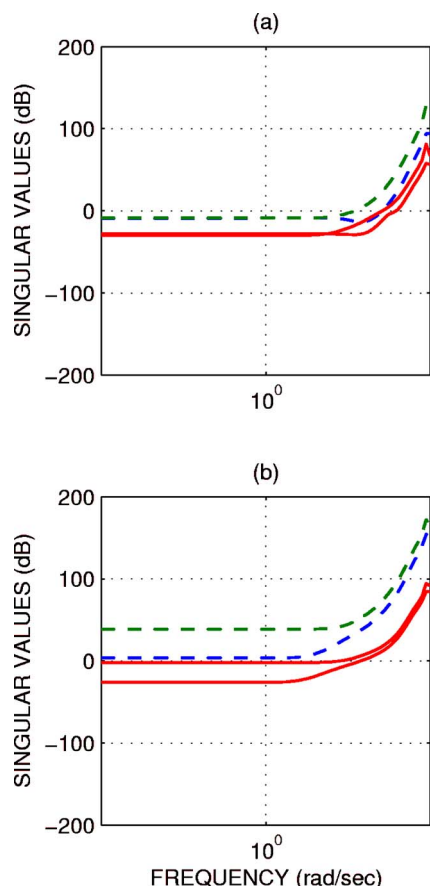
FIG. 13. (Color online) Singular-value bounds with the finite wall property error model.

closed-loop time response of the upper and lower-wall Nusselt numbers. Like in Refs. [6–8], the measure of the residual convection can be effectively shown using the Nusselt number plots. The Nusselt numbers at the upper and lower wall measure the ratios of total heat flux (convective and conductive) to the conductive heat flux leaving and entering the fluid layer. As Nusselt number approaches the value 1.0, the fluid layer convection is removed. Robustness is determined based on how much mismatches can be tolerated before the closed-loop system is unstable.

Although the parameter field is extremely vast, we have simulated a large number of cases but for limited space only a selective number of representative cases are presented. Since the focus of this paper is the robustness of the closed-loop system with respect to parameter mismatches, the Rayleigh number is set at a constant during the simulation. No gain-schedule algorithm [8] will be engaged. The nominal parameters are set at $Pr=7.0$, $Ra^*=2 \times 10^4$, $k_x^*=k_y^*=1.0$. Unlike the linear analysis, these are fundamental wave numbers. The nominal geometric and material properties, sensor and actuator configurations are the same as in the linear analysis (see first paragraph of Sec. III A). The simulations correspond to 32×32 Fourier modes (horizontal). The integration and output sampled step is $\Delta t=0.004$. The simulation period T is 0.4 time units. Only one set of initial condition is used, corresponding to the residual state of the closed-loop simulation at $t=0.4$ presented in Ref. [8]. We use two ver-

sions of the LQG compensator, C1 and C3, designs based on a one-layer and three-layer model, respectively. Both are based on a reduced-order linear model consisting of only eight vertical complex modes (contrast to 64 vertical real modes in the plant model).

2. Finite wall properties

We selected a handful of cases to characterize the closed-loop behavior (both stable and unstable cases included). Figure 14(a) shows the upper and lower Nusselt number responses when the compensator C1 is used. The plant parameters are set at nominal. Note that the compensator has idealized thermal boundary conditions whereas the plant has finite walls incorporated. The upper (dashed) and lower Nusselt number (solid) show convection damped out in time. We then switch to compensator C3, the time response (not shown here) is visibly indistinguishable from that of Fig. 14(a).

Keeping the plant at nominal condition, now we reduce the upper and lower wall's thermal conductivity and diffusivity values each by 50%. The closed-loop system is stable with C1 as well as C3.

Next, we increase both wall thicknesses from the nominal value to $d_\ell=d_u=0.15$. Compensator C1 is not capable of suppressing convection any longer. Figure 14(b) shows the initial response. Eventually, the solution diverges. Using compensator C3, with the nominal wall thicknesses at 0.1, C3 still cannot damp out convection. In this case, the solution takes longer to diverge (plot not shown).

We conclude that the mismatches in wall thermal properties between the compensator and plant up to 50% is easily tolerated. But the mismatch in wall thickness is significantly more sensitive.

3. Simulations with actuator lag

In evaluating the actuator lag, we reset all the plant parameters to nominal values. To incorporate the first-order actuator lag, the last of Eqs. (15) has to be incorporated into the time-splitting algorithm of the 3D nonlinear plant model. We rewrite the equation for the lower plane actuator (similar equation for the upper plane actuator),

$$\dot{u}_{\ell i} = -\omega_d u_{\ell i} + \omega_d u_{\ell o}. \tag{23}$$

Subscript o denotes the output from the compensator and i denotes the input to the plant; the lag frequency $\omega_d=2\pi/\tau_d$. We attempted to integrate the above first-order equation by the explicit Euler scheme. The closed-loop solution is numerically unstable. We switch to the implicit Euler scheme,

$$u_{\ell i}^{(n+1)} = \frac{u_{\ell i}^{(n)} + \Delta t \omega_d u_{\ell o}^{(n+1)}}{1 + \Delta t \omega_d}, \tag{24}$$

which is numerically stable. For a lag time constant τ_a as large as 3×10^{-2}, C1 successfully stabilizes the system. Surprisingly, this time constant is significantly higher than that predicted by the linear stability result (see Fig. 7). With C3, the performance is only slightly better. We increase the lag time constant to $\tau_a=0.1$, ten times as large. In Fig. 14(c), we show the time response. The closed-loop system is unstable.
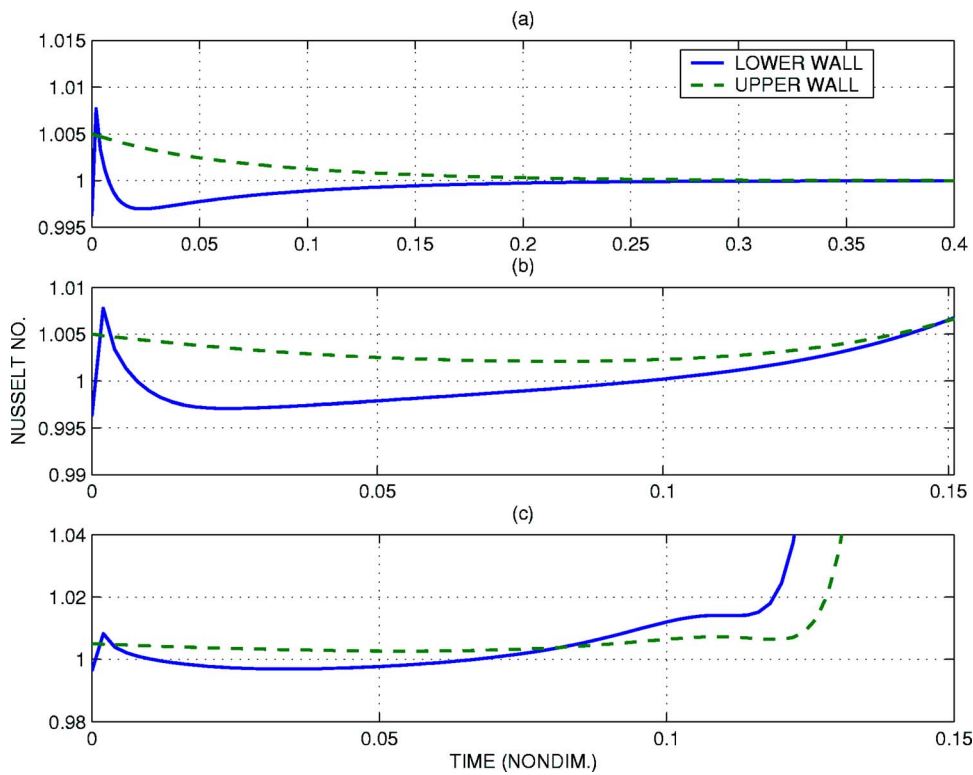
FIG. 14. (Color online) Case studies in the nonlinear simulations.

4. Major parameter uncertainties

The most benign major parameter mismatch by far is the Prandtl number. At nominal conditions, we can reduce Pr from 7.0 to 0.7 in the plant (compensator remains at Pr =7.0) without destabilizing the closed-loop time response.

For Rayleigh number, previous results indicate that the higher the nominal value Ra* (here Ra*=2×10^4), the smaller the plant uncertainty in Ra can be tolerated. Here, we let Ra=1.05Ra* (5% uncertainty), C1 is capable of stabilizing the no-motion state. However, when we set Ra=1.1Ra$_c^*$, now C1 is fighting very hard. We show the time response in Fig. 15(a). Considerable improvement is demonstrated by using C3 instead, as the time response shown in panel (b). But the system is still unstable. The Ra margin in the 3D
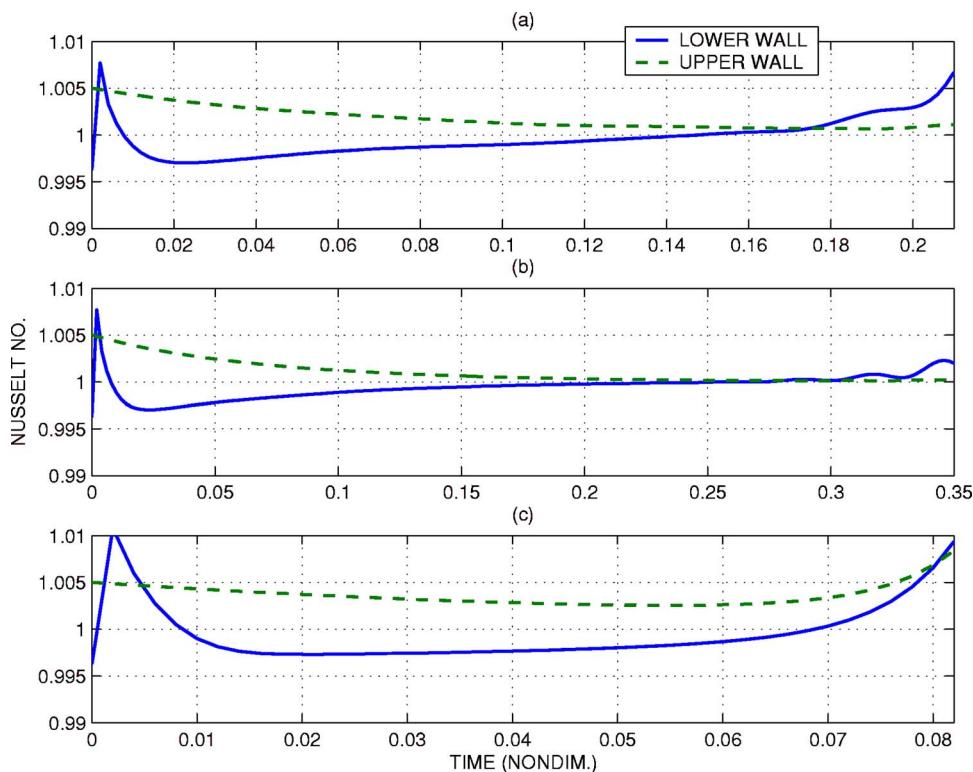

FIG. 15. (Color online) More case studies in the nonlinear simulations.

nonlinear model appears weaker than that predicted by the linear stability model (see Fig. 3).

5. Simulations with sensor plane level mismatch

Last, we consider the sensor plane level mismatch. The sensor level appears to be a sensitive parameter to the closed-loop stability. Even though we cannot run as many Monte Carlo cases as in the linear stability study (see Fig. 8), we ran several cases with level mismatch with standard deviation (STD) ±0.02 randomly (zero mean, Gaussian) added to the three nominal levels. The closed-loop responses remain stable. However, when we increase the mismatch STD to ±0.05, the closed-loop system is unstable. Figure 15(c) shows the time response for a case, with z_s=0.15, 0.55, and 0.85).

In examining the time responses of the Nusselt numbers, it seems puzzling at first to see that the convective disturbance is damped out to a very small amplitude in all cases initially, but the control action cannot sustain stability in some cases. The explanation is as follows. The initial time responses depend on the initial condition of the states. Since only one set of initial states is used, it is not surprising that the initial responses for all cases are similar. The simulation time appears adequate for the unstable modes to re-organize. The main point is that we have to simulate long enough to pass the initial transient period. The asymptotic response is what determine stability.

There is no specific mention about how the sensors can be implemented. It should be understood that the conventional, invasive-type of temperature sensors are probably not practical. Through private communications, however, it comes to our knowledge that certain infrared (IR) optical temperature sensing techniques (remote sensing) are available. Such optical remote-sensing method can probe temperatures at various depths in the layer, to very high accuracy. If the field-of-view of the sensor cannot cover the total horizontal span of the entire layer, a high-frequency scanning technique can be used to reconstruct the temperature field. For laboratory implementations, the remote-sensing method in measuring the temperatures should be further investigated.

IV. CONCLUSION

This study is to assess the amount of mismatches in the plant parameters (for a particular sensor and actuator configuration) that can be tolerated by the LQG compensator, before the closed-loop system turns unstable. This assessment is an important step towards any potential future laboratory implementation. The assessment is done by keeping the compensator operating at the nominal values and introducing mismatches to the plant model.

Based on the results from both the linear stability study and the nonlinear time-domain simulations, we draw the following conclusions: (i) Introducing the finite wall to the fluid layer does not have a significant impact in altering the closed-loop stability properties. The thermal conductive and diffusive properties of the walls in the study correspond to a good conducting material. The case of poor conducting material has not been considered. Therefore the idealized ther-

mal boundary condition used in Refs. [5–8] appears adequate. The current results indicate that using the compensator C1 (with idealized boundary conditions) versus the finite-wall compensator C3 does not make any significant difference at all. For potential laboratory implementation, the dynamical model with idealized boundary conditions is probably adequate. (ii) Using two actuator planes on both walls does not show significant improvement in performance over using one actuator plane on the lower wall. Using two actuator planes reduces the load carried by one actuator plane. (iii) For the parameter mismatches in Rayleigh number, wall conductive and diffusive properties, wall thickness and sensor level locations, the linear stability results shows considerably larger margins than those obtained from the fully nonlinear simulations. For the actuator lag, however, it is the other way. The nonlinear results show more margins that from the linear results. Both linear and nonlinear results indicate that the Pr mismatch is insignificant. Mismatched Pr value anywhere in the range of 0.7–7.0 is tolerated. (iv) The more sensitive mismatches arise from the wall thicknesses and the sensor level locations. Both linear analysis and nonlinear simulations indicate that only small mismatches in these parameters can be tolerated at Ra=11.7Ra$_c$ (nominal value). Reducing the nominal Ra will reduce the sensitivity for given thickness and level mismatches.

In conclusion, the LQG compensator design is adequate to suppress convection in the vicinity of 10–15 times the critical Ra. The implementation of the actuator does not seem to be a challenge. The study shows that significant actuator lag can be tolerated. The major challenge appears to be in the sensors. The problem of sensitivity of stability margins to the sensor levels may require a novel temperature measurement technique to resolve. Rather than the invasive method, it is desirable to use the IR remote-sensing technique, coupled with a scanner approach. In principle, such technique can deliver temperature measurements at several levels of the fluid layer simultaneously, rapidly and accurately. Further investigation of the advanced sensing method is necessary for potential laboratory experiments.

APPENDIX: CONDUCTIVE TEMPERATURE PROFILE

Let the outer surfaces of the upper and lower walls be prescribed at temperatures T_1^* and T_2^*, respectively. Let the layer thicknesses from below up be d_1^*, d^*, and d_u^*. Use the fluid layer thickness d^* and the temperature difference $\Delta T^* = T_2^* - T_1^*$ as the scales for length and temperature, respectively, so that we note the nondimensional variables (no asterisk) $T=T^*/\Delta T^*$, $z=z^*/d^*$, $T_1=T_1^*/\Delta T^*$, $T_2=T_2^*/\Delta T^*$, $d_l=d_l^*/d^*$, $d=1$, and $d_u=d_u^*/d^*$. Let T_3 and T_4 be the nondimensional temperatures at the inner upper and lower walls. The constant dimensional heat flux Q^* in the layers is given by
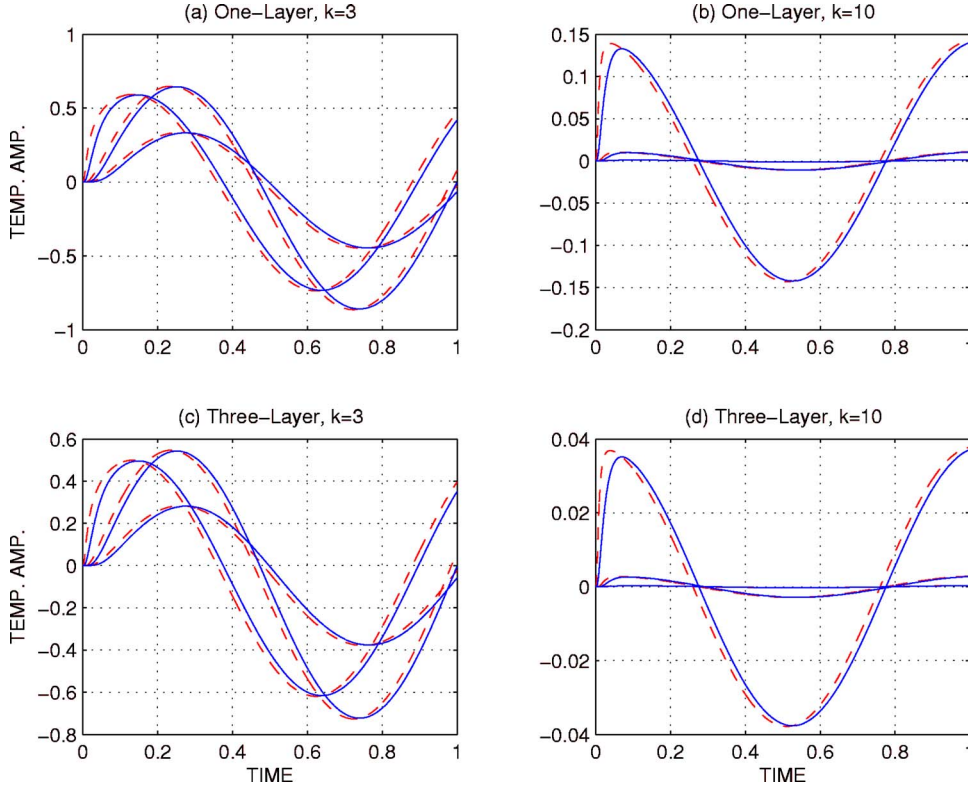
FIG. 16. (Color online) Sensor temperature comparison for one-layer vs three-layer, with (solid) and without (dashed) actuator lag.

$$Q^* = \frac{k^*\Delta T^*}{d^* h}, \quad h = 1 + d_u + d_l, \tag{A1}$$

where h is the nondimensional factor given in Eq. (A1). The temperatures T_3 (at upper wall inner surface) and T_4 (at lower wall inner surface) are

$$T_3 = T_1 + d_u/(k_u h), \quad T_4 = T_2 - d_l/(k_l h). \tag{A2}$$

We denote the thermal conductivity ratios $k_l = k_l^*/k^*$ and $k_u = k_u^*/k^*$. The temperature in the three layers as a function of z is

$$T(z) = \begin{cases} T_2 - (z + d_l)/(k_l h), & -d_l \leq z \leq 0, \\ T_4 + (T_3 - T_4)z, & 0 < z \leq 1, \\ T_1 + (1 + d_u - z)/(k_u h), & 1 < z \leq 1 + d_u. \end{cases} \tag{A3}$$

The effective Rayleigh number is the fluid interface-to-interface Rayleigh number. This number is given by $\mathrm{Ra}_f = \alpha^* g \Delta T^* (T_4 - T_3) d^{*3}/v^* \kappa^*$. We derive that

$$\mathrm{Ra}_f = \left(1 - \frac{d_l}{k_l h} - \frac{d_u}{k_u h}\right)\mathrm{Ra}, \tag{A4}$$

with $\mathrm{Ra}_f < \mathrm{Ra}$.

It is helpful to show the plant input-output relationship, at least for the linear case in subcritical condition. Consider $\mathrm{Pr} = 7.0$, $\mathrm{Ra} = 0.9\mathrm{Ra}_c$, let the nominal wall thermal conductivity and diffusivity values be reduced by 50% (for exaggeration). Consider a strong actuator lag with time constant $\tau_a = 0.1$. Consider a single, 2D Fourier mode of control at wave number of $k = 3$ and at $k = 10$. The control is the input temperature to the plant, with amplitude (Fourier coefficient) $u = \cos(2\pi ft)$ (here $f = 1$). The plant outputs are the temperature amplitudes at the nominal sensor plane levels $z_s = 0.2$, 0.5, and 0.8. Figure 16 shows the time responses of the control. On the left column, the upper and lower panel correspond to the one-layer and three-layer case, respectively. The wave number of the spatial sinusoidal disturbance is $k = 3$. The time responses in the two panels are very close, suggesting that, at least for the purely conductive case, the idealized wall and finite wall boundary conditions are about the same. The dashed curves (no lag, i.e., $\tau_a = 0$) are close to the solid curves (with lag, $\tau_a = 0.1$) despite the large actuator lag time constant. Note that the peaks shift to the right as zs is increased. However, for $k = 3$ the temperature maximum occurs at the midplane rather than at the sensor plane closest to the actuator. Similarly, we show the responses on the right column. The right column corresponds to the larger wave number, $k = 10$. For the small-scale control, the temperature amplitude rapidly attenuates when moved away from the actuator plane. Unlike in the case of $k = 3$, the temperature amplitude drops monotonically as z_s is increased. It suggests that small-scale control can exist only in the region close to the actuator plane.

[1] L. E. Howle, Phys. Fluids **9**, 1861 (1997).

[2] J. Tang and H. H. Bau, J. Fluid Mech. **363**, 153 (1998).

[3] L. E. Howle, Int. J. Heat Mass Transfer **40**, 817 (1997).

[4] J. Tang and H. H. Bau, Proc. R. Soc. London, Ser. A **447**, 587 (1994).

[5] A. C. Or, L. Cortelezzi, and J. L. Speyer, J. Fluid Mech. **437**, 175 (2001).

[6] A. C. Or and J. L. Speyer, J. Fluid Mech. **483**, 111 (2003).

[7] P. S. Marcus, J. Fluid Mech. **146**, 45 (1984).

[8] A. C. Or and J. L. Speyer, Phys. Rev. E **71**, 046302 (2005).

[9] L. E. Howle, J. Fluid Mech. **411**, 39 (2000).

[10] A. C. Or and R. E. Kelly, J. Fluid Mech. **440**, 27 (2001).

[11] J. C. Doyle and G. Stein, IEEE Trans. Autom. Control **AC-24**, 607 (1979).

[12] J. L. Speyer *et al.*, J. Guid. Control Dyn. **7**, 695 (1984).

APPENDIX D:
Sustained Sub-laminar Drag in a Fully Developed Channel Flow

Sustained sub-laminar drag in a fully developed channel flow

By TAEGEE MIN, SUNG MOON KANG, JASON L. SPEYER
AND JOHN KIM

Department of Mechanical and Aerospace Engineering, University of California, Los Angeles,
CA 90095-1597, USA

It is shown, by direct numerical simulations, that the skin-friction drag in a fully developed channel can be sustained below that corresponding to the laminar profile when the flow is subjected to surface blowing and suction in the form of an upstream travelling wave. A key mechanism that induces the sub-laminar drag is the creation of positive (negative) Reynolds shear stress in the wall region, where normally negative (positive) Reynolds shear stress is expected given the mean shear. This mechanism is contained in the linearized Navier–Stokes equations, thus allowing linear analysis of the observed phenomena. When applied to a fully developed turbulent channel flow, skin-friction drag is also significantly reduced by an upstream travelling wave, demonstrating that the surface blowing and suction in the form of such a wave is also effective in fully developed turbulent flows. Consideration of the energy budget shows a possibility of net drag reduction in turbulent channel flows with the present open-loop control.

1. Introduction

The minimum sustainable drag in a fully developed channel (pipe) flow is of fundamental importance, as it can be used as a basis for performance limitations for various controllers designed to reduce skin-friction drag in channel (pipe) flow. Bewley (2001, see also Bewley & Aamo 2004) proposed the following conjecture ('Bewley's conjecture' hereinafter):

> "The lowest sustainable drag of an incompressible constant mass-flux channel flow, when controlled via a distribution of zero-net mass-flux blowing/suction over the no-slip channel walls, is exactly that of the laminar flow."

This conjecture can be elucidated by a useful expression for skin-friction drag in fully developed channel flows (Fukagata, Iwamoto & Kasagi 2002 and Bewley & Aamo 2004):

$$D = \frac{1}{2} \left(\frac{\mathrm{d}U}{\mathrm{d}y}\bigg|_{-1} - \frac{\mathrm{d}U}{\mathrm{d}y}\bigg|_{1} \right) = 2 + \frac{3}{2} Re \int_{-1}^{1} \overline{u'v'} y \, \mathrm{d}y. \tag{1.1}$$

Here, all quantities are normalized by the centreline velocity of the laminar Poiseuille flow ($U_c = \frac{3}{2} U_b$, U_b is the bulk velocity) and the channel half-height (δ), U denotes the mean velocity, Re the Reynolds number based on the laminar centreline velocity, and $\overline{u'v'}$ is the Reynolds shear stress. In this paper, u, v, and w denote, respectively, the velocity component in the streamwise (x), wall-normal (y), and spanwise (z) directions, and the prime denotes a fluctuating quantity. Note that (1.1) is valid for all channel flows with the same mass flux as the base laminar flow (4/3 with the

present normalization). The first term on the right-hand side of (1.1) represents the mean wall-shear rate of laminar flow ($U = 1 - y^2$), and therefore (1.1) shows that skin-friction drag in a channel flow consists of the laminar drag plus the y-weighted integral of $\overline{u'v'}$. From the viewpoint of (1.1), Bewley's conjecture is equivalent to saying that the y-weighted integral of $\overline{u'v'}$, with and without control input, is always positive in channel flows. For regular channel flows without control, this is the case, since the Reynolds shear stress in the lower half of the channel ($-1 < y < 0$) is negative, while the opposite is true in the upper half of the channel ($0 < y < 1$). As such, the skin-friction drag in transitional and turbulent channel flows is higher than that of the corresponding laminar flow with the same mass flux. With a form of periodic control, Bewley & Aamo (2004) report that they could not sustain the Reynolds shear stress necessary to yield drag below the laminar value. They provide phenomenological justification by a Reynolds analogy between convective momentum transport and convective heat transport, but they left the proof of the conjecture as an open problem.

The objective of this paper is to explore a control input, in the form of zero-net-mass-flux blowing and suction on the wall, that can sustain the Reynolds shear stress in such a way that the y-weighted integral of $\overline{u'v'}$ remains negative. In the following sections, we shall show that a control input in the form of an upstream travelling wave indeed produces the Reynolds shear stress that makes a negative contribution to the total drag, resulting in sustained sub-laminar drag in a fully developed channel flow. It is worth pointing out that although control input in the form of surface blowing and suction used in the present work is easy to implement numerically, it may not be straightforward to implement in real flows. An alternative possibility is discussed in § 5.

2. Linear analysis

Recent studies have shown that certain linear mechanisms play important roles in turbulent boundary layers (for example, see Jiménez & Pinelli 1999; Kim & Lim 2000). Recognizing the role of linear mechanisms, particularly that of self-sustaining near-wall turbulence in turbulent boundary layers, several investigators have successfully applied modern control theories to develop optimal controllers based on the linearized Navier–Stokes equations (see, for example, Bewley 2001 and Kim 2003 and references therein). The success of these controllers when applied to fully nonlinear flows further demonstrates the usefulness of linear analysis in designing controllers for fully non-linear flows. Here, we first study the effect of travelling control waves on the Reynolds shear stress by examining the solution to the linearized Navier–Stokes equations.

The linearized Navier–Stokes equation for a two-dimensional channel flow can be written as

$$\frac{\partial \hat{v}}{\partial t} = (\nabla^2)^{-1} \left(-i\alpha U \nabla^2 + i\alpha \frac{d^2 U}{dy^2} + \frac{1}{Re} \nabla^4 \right) \hat{v}, \tag{2.1}$$

where $\hat{v}$ denotes the Fourier-transformed wall-normal velocity perturbation (v'), $\nabla^2 = \partial^2/\partial y^2 - \alpha^2$, and α is a wavenumber in the streamwise direction. Equation (2.1) can be written in the following state-space representation (for further details, see Kim 2003):
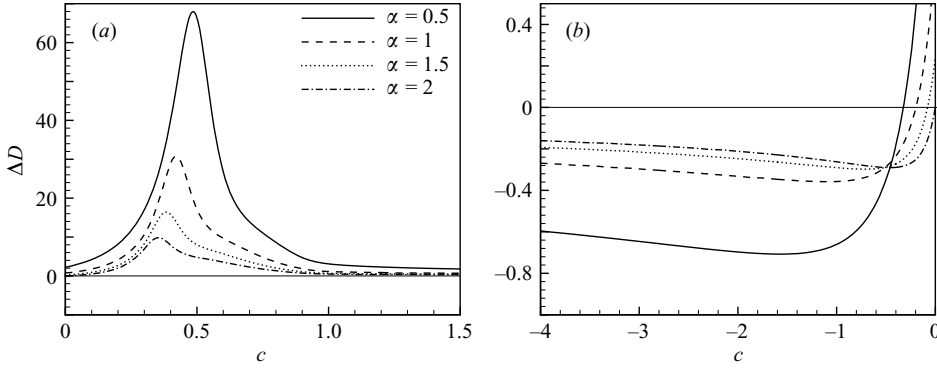
$$\frac{dx}{dt} = Ax + Bu, \tag{2.2}$$

FIGURE 1. ΔD in steady state at $Re = 2000$ and $a = 0.1$: (*a*) downstream travelling waves
($c > 0$); (*b*) upstream travelling waves ($c < 0$).

where the vector x represents the 'state' of the system and consists of $\hat{v}$ in Galerkin-Chebyshev space. The system matrix A is related to the linear operator in (2.1), while the input matrix B and the control u determine how the control input affects the state. For any control u, the solution to equation (2.2) can be found by:

$$x(t) = e^{At}x(0) + \int_0^t e^{A(t-\tau)}Bu(\tau)\,\mathrm{d}\tau. \tag{2.3}$$

We consider the solution when control input is introduced as surface blowing and suction in the form of a travelling wave. The initial objective of this study was to develop a control strategy for viscous drag reduction through periodic control of a turbulent boundary layer. In the process of optimizing the control input defined at multiple wavenumbers, it was observed that certain upstream travelling waves reduced the drag, while certain downstream travelling waves increased the drag. In order to simplify our analysis, we consider travelling control waves consisting of a single wavenumber. Such a control can be expressed in physical space as boundary conditions for v:

$$v_{\mathrm{w}} = a\cos(\alpha(x - ct)), \tag{2.4}$$

where a and c denote the amplitude and wave speed of blowing/suction on the wall, respectively. In the present study, the blowing/suction (2.4) is implemented on both walls in varicose mode, i.e. the upper and lower walls have the blowing/suction in phase at the same streamwise locations. Note that, with stable systems, $\exp(At) \to 0$ as $t \to \infty$. Given control input (2.4), equation (2.3) can be analytically solved for $\hat{v}$ as $t \to \infty$, and the Reynolds shear stress $\overline{(u'v')}$ is obtained using the continuity equation ($i\alpha\hat{u} + \partial\hat{v}/\partial y = 0$).

Figure 1 shows the y-weighted integral of $\overline{u'v'}$ as a function of the wave speed for $Re = 2000$ and $a = 0.1$. Here, ΔD is defined as

$$\Delta D = \frac{3}{2}Re \int_{-1}^{1} \overline{u'v'}\, y \,\mathrm{d}y. \tag{2.5}$$

Note that ΔD is positive (increased drag) with downstream travelling waves ($c > 0$), whereas it is negative (reduced drag) with upstream travelling waves ($c < 0$) except near small negative c (slow upstream travelling wave). Note also that there exists an optimal wave speed, where ΔD reaches its minimum (with negative c) and maximum (with positive c). We mention in passing that the large peak with a positive c is

related to the most observable and controllable system mode. Also, although this large production of ΔD at a certain c is of no interest to the present study, it can be useful in certain applications and warrants further study.

It is apparent from the linear analysis that certain surface blowing and suction in the form of an upstream travelling wave can induce the Reynolds shear stress in such a way that the total drag could be less than that of the laminar flow. This is contrary to Bewley's conjecture. Strictly speaking, however, the linear analysis assumes that the mean velocity profile, and hence the drag, is not affected by perturbations (i.e. the system matrix $\boldsymbol{A}$ is independent of $\boldsymbol{x}$). The real effect of travelling waves on the drag must be investigated by a direct numerical simulation, where the nonlinear effects are included. In the following section, we begin investigating whether such Reynolds shear stress can be sustained in nonlinear flows with the same control input.

Bewley & Aamo (2004) provided a phenomenological justification by an analogy between convective momentum transport and convective heat transport. Clearly, this analogy does not hold. This failure of the analogy, however, is not due to nonlinearity of momentum transport since the present analysis is linear. Rather, it is due to differences in the linear equations. Among others, convective heat transport is governed by a single scalar equation, whereas convective momentum transport is governed by two equations coupled through the continuity equation. The present linear analysis indicates that a certain flow-field unsteadiness induced by wall-normal motion can decelerate the momentum transport in the direction of viscous diffusion, whereas the heat transport is always accelerated by flow-field unsteadiness as pointed out by Bewley & Aamo (2004).

3. Two-dimensional channel flow

We will first study the effect of travelling waves in two-dimensional channel flows. Disturbances are finite but they are two-dimensional, similar to those considered by Bewley & Aamo (2004). A pseudo-spectral code similar to that used by Kim, Moin & Moser (1987) is employed. Simulations are conducted at $Re = 2000$, and the computational domain of $4\pi\delta \times 2\delta$ is used in the streamwise and wall-normal directions, respectively, with a 32×65 grid. The mean pressure gradient is varied to maintain a constant mass flux, and the total drag is measured by averaging the mean velocity gradient on both walls.

Figure 2 shows the results for a travelling wave of $\alpha = 0.5$ at $c = -2$. All simulations start from the laminar flow with no initial disturbances, and a steady state is reached when $t > 500$ as shown in figure 2(a). It is apparent that the sub-laminar drag is sustained for all amplitudes shown. Figure 2(b) shows that the results from the linear analysis agree with those from direct numerical simulations for small amplitudes. As expected, the nonlinear results deviate from the linear solutions as the amplitude is increased (figure 2b).

In order to examine the physical mechanism responsible for drag reduction by the upstream travelling waves, we performed numerical simulations of 'channel flow' without the imposed mean flow, i.e. $U = 0$ everywhere initially and the imposed mean pressure gradient was set to zero. Blowing and suction as prescribed in (2.4) was applied, and the simulations were carried out until a statistically steady state was reached. The momentum balance for this flow is

$$\frac{\mathrm{d}}{\mathrm{d}y}\left(-\overline{u'v'} + \frac{1}{Re}\frac{\mathrm{d}U}{\mathrm{d}y}\right) = 0 \quad \text{or} \quad -\overline{u'v'} + \frac{1}{Re}\frac{\mathrm{d}U}{\mathrm{d}y} = C. \tag{3.1}$$
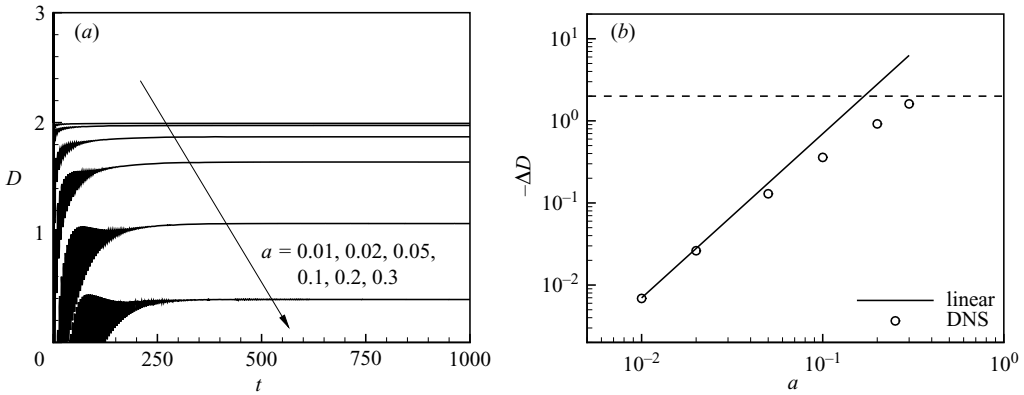
FIGURE 2. Viscous drag in a two-dimensional channel flow with $\alpha = 0.5$ and $c = -2$: (*a*) time histories of D for various control amplitudes; (*b*) ΔD in a steady state as a function of control amplitudes.
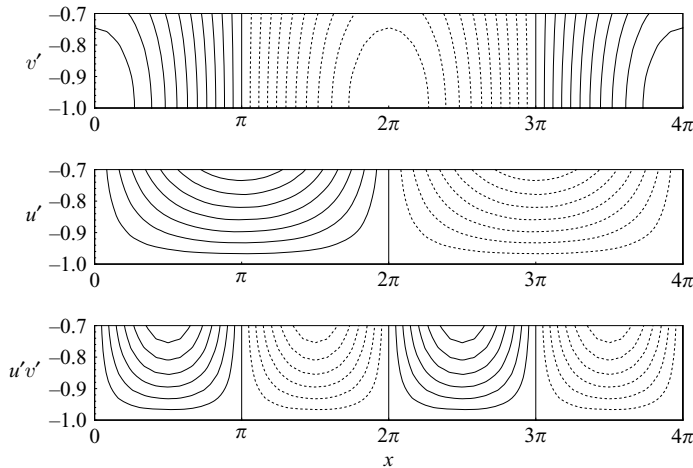

FIGURE 3. Contours of v' (top), u' (middle) and $u'v'$ (bottom) near the lower wall with a standing wave. Contour levels for v', u' and $u'v'$ are -0.01–0.01, -0.02–0.02 and -0.0001–0.0001, respectively (20 levels).

The integration constant C must be zero to satisfy the boundary conditions. A standing wave ($c = 0$ in (2.4)) created no net $-\overline{u'v'}$ as expected from the symmetry of the problem. Upstream travelling waves created positive $\overline{u'v'}$ near the lower wall, which was balanced by a positive dU/dy, implying that U is positive. In other words, upstream travelling waves induced a net mass flux in the opposite direction. Downstream travelling waves would create the opposite effect due to the apparent symmetry. The amount of induced mass flux was proportional to the amplitude of the travelling wave. Contours of v', u', and $u'v'$ near the lower wall with a standing wave and an upstream-travelling wave are shown in figures 3 and 4, respectively. It is apparent that the travelling wave had a different impact on the phase of u' and v'. Figure 5 illustrates the effect of standing and travelling waves on u' and v' at a location near the lower wall ($y = -0.95$) at $\omega t = 2\pi$. With a standing wave, the phase of u', which is related to that of dv'/dy through the continuity equation, is 90° out
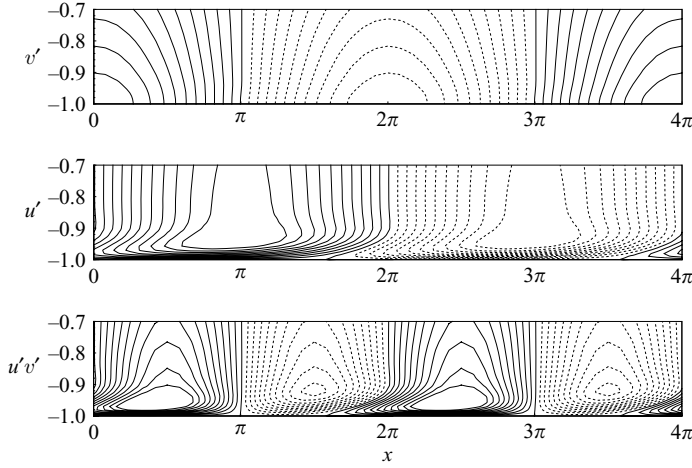
FIGURE 4. Contours of v' (top), u' (middle) and $u'v'$ (bottom) near the lower wall with an upstream travelling wave. Contour levels are the same as those used in figure 3.
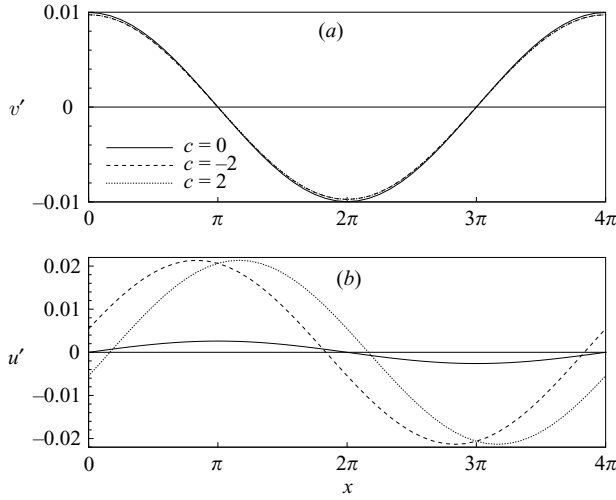

FIGURE 5. Effect of standing and travelling waves on u' and v' at $y = -0.95$ for $Re = 2000$, $\alpha = 0.5$ and $a = 0.01$: (a) v'; (b) u'.

of phase as shown in the figure. With an upstream travelling wave, the phase of v' remains approximately the same as that of the travelling wave, while that of u' is leading (upstream direction) that of v'. This phase lead in u' results in a net positive Reynolds stress as can be seen from

$$v' = c_1 \cos(\alpha x), \tag{3.2}$$

$$u' = c_2 \sin(\alpha x + \phi), \tag{3.3}$$

$$\overline{u'v'} = c_1 c_2 \overline{\sin(\alpha x + \phi) \cos(\alpha x)}$$

$$= \tfrac{1}{2} c_1 c_2 \sin \phi. \tag{3.4}$$

With a positive ϕ as shown in figure 5, $\overline{u'v'}$ is positive. With a downstream travelling wave, ϕ is negative, resulting in a negative $\overline{u'v'}$. This phase shift in u' resulted in net
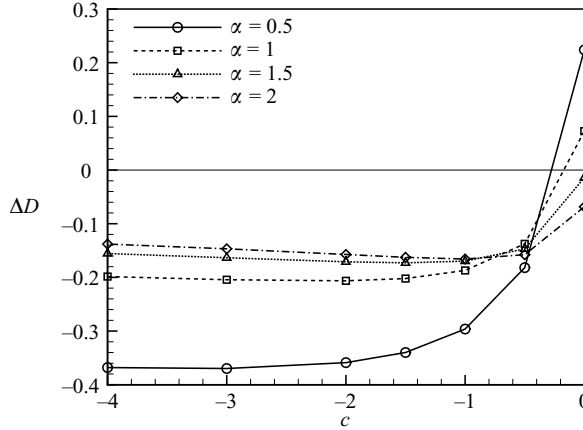
FIGURE 6. ΔD as a function of the wave speed and wavenumber for $a = 0.1$.

positive (negative) Reynolds shear stress with an upstream (downstream) travelling wave, which in turn induced net mass flux in the direction opposite to the travelling wave. The effect of travelling waves in a channel flow would be similar, although it would have been modified by the presence of mean U driven by the mean pressure gradient. Since an upstream travelling wave induces a net mass flux in the streamwise direction, the amount of mass flux to be driven by the pressure gradient in the channel flow with a fixed mass flux is reduced, resulting in reduced drag. If we had fixed the mean pressure gradient instead, the net mass flux in the channel would have increased due to the positive mass flux induced by an upstream travelling wave.

The flow remains stable for large a as the drag continues to decrease. However, when the amplitude exceeds a certain value, the induced mass flux exceeds the fixed mass flux. In fact, the drag (and hence the pressure force required to maintain the same mass flux) becomes negative as the entire flow is driven by the power required to provide the blowing and suction, and comparison with a channel flow is no longer meaningful. With downstream travelling waves ($c > 0$), on the other hand, the flow becomes unstable and the drag increases drastically as a is increased.

Figure 6 shows drag variations as a function of the wave speed for different streamwise wavenumbers with a fixed amplitude $a = 0.1$. Note that ΔD in nonlinear simulations represents the change in the total drag (see equation (1.1)). The nonlinear results show the same trend observed in the linear solutions: that is, ΔD becomes larger for smaller α, and there is an optimal wave speed that induces the minimum ΔD. The optimal wave speed for nonlinear simulations appears to be slightly more negative (faster upstream) than that of the linear solutions.

4. Turbulent channel flow

In this section, we investigate the effect of travelling waves in a turbulent channel flow. The same code is used to perform direct numerical simulations of a turbulent channel flow at $Re = 2000$. The computational domain is $4\pi\delta \times 2\delta \times 4\pi\delta/3$ in the streamwise, wall-normal and spanwise directions, respectively, and $64 \times 97 \times 64$ grid points are used in each direction. All simulations were started from a turbulent channel flow that had reached a steady state without control input. Figure 7 shows time histories of D in a turbulent channel flow. An upstream travelling wave at $\alpha = 0.5$ with $c = -2$ is applied on both walls in varicose mode, as was the case for the
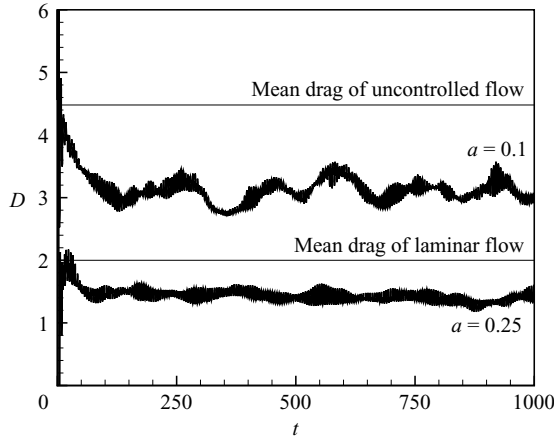
FIGURE 7. Time histories of D in a turbulent channel flow for $\alpha = 0.5$ and $c = -2$.
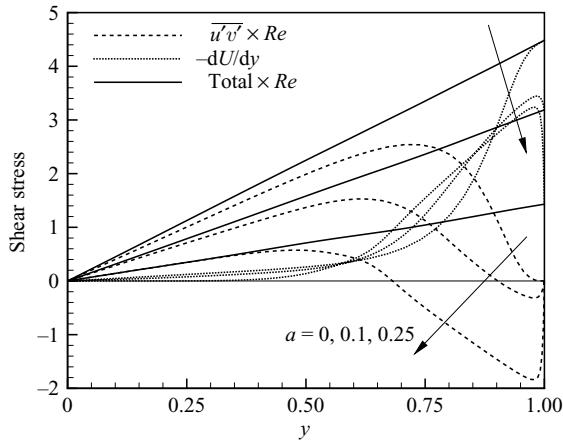

FIGURE 8. Distribution of total, viscous, and Reynolds shear stresses in the upper half of the channel for different control amplitudes. This is for the case of $\alpha = 0.5$ and $c = -2$.

two-dimensional channel discussed in §3. The same parameters as in two-dimensional channel flow were used, and they are by no means optimal ones for turbulent channel flows. Similar to the two-dimensional flows, a significant drag reduction is obtained, and the reduction is greater for larger amplitudes (about 30% and 70% drag reduction, respectively, with amplitudes 0.1 and 0.25). Note that, with $a = 0.25$, the sustained drag is sub-laminar even for this three-dimensional flow. It is worth noting, however, that this amplitude is much larger than that used in the opposition control of Choi, Moin & Kim (1994) and in the LQG control of Lee *et al.* (2001).

Figure 8 shows the total shear stress for the case of $\alpha = 0.5$ and $c = -2$ with $a = 0, 0.1$ and 0.25. The total shear stress for each case is a straight line, indicating that the flow has indeed reached a statistically steady state. Also shown in the figure are viscous stress $(\mathrm{d}U/\mathrm{d}y)$ and Reynolds shear stress $(\overline{u'v'})$. The positive $\overline{u'v'}$ in uncontrolled turbulent flow (note that only the upper half of the channel is shown in the figure, where the Reynolds shear stress is normally positive) is decreased by the effect of the upstream travelling wave. For the case of $a = 0.25$, $\overline{u'v'}$ near the wall becomes negative, which in turn results in sub-laminar drag.

The efficiency of the present control input in the form of a travelling wave is of great interest. In the present study, the efficiency η is defined as

$$\eta = \frac{P_{\text{drag}} + P_{\text{input}}}{P_0}. \tag{4.1}$$

Here, P_0, P_{drag} and P_{input} denote the power required for uncontrolled flow, the power required for drag-reduced flow, and power input for blowing and suction, respectively, and they can be expressed as

$$P_0 = \frac{4}{3}\frac{1}{Re}D_0, \quad P_{\text{drag}} = \frac{4}{3}\frac{1}{Re}D, \quad P_{\text{input}} = \overline{(p_{\text{w}} + \tfrac{1}{2}v_{\text{w}}^2)v_{\text{w}}}, \tag{4.2}$$

where D_0 denotes the mean wall-shear rate of uncontrolled flow, and p_{w} and v_{w} are the pressure and wall-normal velocity at the wall, respectively. Recall that the bulk velocity used in defining the power is 2/3 with the present normalization and the total drag is the sum of the drag on each wall. Also note that additional power required to account for the friction loss associated with blowing and suction through the wall is not included in (4.1). For $a = 0.1$ and $a = 0.25$, the efficiency η was found to be 0.76 and 0.81, respectively. In other words, the total power required to have the same mass flux was only 76% and 81% of the power required in a channel without control. Recall that there was about 30% and 70% drag reduction for $a = 0.1$ and $a = 0.25$, respectively. In comparison, the opposition control of Choi *et al.* (1994) reduced drag in a channel by about 30% and η was found to be about 0.7. For that closed-loop control, P_{input} was negligible compared to P_0, and therefore the power saved is directly related to the reduced drag. For the present open-loop control, however, P_{input} was significant, and the power saved was less (especially for high a) than the saving due to reduced drag. This was in part due to the large amplitudes of the travelling waves. Its low power saving notwithstanding, it is remarkable that substantial drag reduction can be achieved in a turbulent channel flow with such a simple open-loop control.

5. Concluding remarks

Motivated by Bewley's conjecture (Bewley 2001), we investigated the possibility of achieving sub-laminar drag in a fully developed channel flow. Sustainable sub-laminar drag was obtained when the flow was subjected to blowing and suction at the wall in the form of an upstream travelling wave. It was found, both from linear analysis and nonlinear simulations, that certain upstream travelling waves induce the Reynolds shear stress in such a way that it makes a negative contribution to the total viscous drag. This was the case not only for the two-dimensional channel flow considered by Bewley & Aamo (2004), but also for a three-dimensional turbulent channel flow. Note that the Reynolds shear stress induced by upstream travelling waves reduces the production of kinetic energy, and therefore the flow remains stable for large-amplitude upstream travelling waves.

Downstream travelling waves, on the other hand, increase the drag. The linear analysis shows that at certain wave speeds the drag increase is dramatic. There are certain applications where the increase in Reynolds shear stress could be desirable. For example, an optimized downstream travelling wave could be used to prevent or delay separation in turbulent boundary layers subject to a strong pressure gradient (e.g. in a diffuser or flow over an airfoil). The optimal use of downstream travelling waves is something that warrants further study.

The open-loop control presented was discovered serendipitously while exploring periodic control of turbulent boundary layers. Unlike the cyclic application of a

pressure feedback control (turning on and off their 'win-win' mechanism) by Bewley & Aamo (2004), our periodic optimization specifically tasked the wall-normal surface blowing/suction control to return the flow state back to its initial condition. Both the time period of control and initial state were part of the optimization (see Speyer 1996). Numerically calculated gradients were used to find a control history, an initial state, and a time period that minimized viscous drag. The two-dimensional travelling wave was discovered as we simplified the optimization to make the problem more tenable. The control presented in this paper is not an optimal solution; our purpose was to investigate whether a sub-laminar drag can be sustained in a fully developed channel flow. In the light of this new finding, optimization is underway. In particular, we plan to explore control input in the form of spanwise and obliquely travelling waves as well as constructing periodic regulators to form closed-loop solutions.

Finally, the current control scheme, consisting of surface blowing and suction in the form of travelling waves, is mathematically simple (and hence easy to implement in numerical experiments), yet it may not be straightforward to implement in real flows. For example, additional space is required to retain the flow through the walls, and the additional hardware required to control blowing and suction may be complicated. However, a moving surface with wavy motion would produce a similar effect, since wavy walls with small amplitudes can be approximated by surface blowing and suction. We plan to perform simulations over moving wavy walls.

REFERENCES

BEWLEY, T. R. 2001 Flow control: new challenges for a new renaissance. *Prog. Aerospace Sci.* **37**, 21–58.

BEWLEY, T. R. & AAMO, O. M. 2004 A 'win-win' mechanism for low-drag transients in controlled two-dimensional channel flow and its implications for sustained drag reduction. *J. Fluid Mech.* **499**, 183–196.

CHOI, H., MOIN, P. & KIM, J. 1994 Active turbulence control for drag reduction in wall-bounded flows. *J. Fluid Mech.* **262**, 75–110.

FUKAGATA, K., IWAMOTO, K. & KASAGI, N. 2002 Contribution of Reynolds stress distribution to the skin friction in wall-bounded flows. *Phys. Fluids* **14**, L73–L76.

JIMÉNEZ, J. & PINELLI, A. 1999 The autonomous cycle of near-wall turbulence. *J. Fluid Mech.* **389**, 335–359.

KIM, J. 2003 Control of turbulent boundary layers. *Phys. Fluids* **15**, 1093–1105.

KIM, J. & LIM, J. 2000 A linear process in wall-bounded turbulent shear flows. *Phys. Fluids* **12**, 1885–1888.

KIM, J., MOIN, P. & MOSER, R. D. 1987 Turbulence statistics in fully developed channel flow at low Reynolds number. *J. Fluid Mech.* **177**, 133–166.

LEE, K. H., CORTELEZZI, L., KIM, J. & SPEYER, J. 2001 Application of reduced-order controller to turbulence flows for drag reduction. *Phys. Fluids* **13**, 1321–1330.

SPEYER, J. L. 1996 Periodic optimal flight. *AIAA J. Guidance, Control, Dyn.* **19**, 745–755.